UNIVERSITY OF CALIFORNIA SAN DIEGO

From large-scale internal tides to small-scale turbulence: observations on the continental slope off Tasmania

A dissertation submitted in partial satisfaction of the
requirements for the degree
Doctor of Philosophy

in

Oceanography

by

Olavo Badaró Marques

Committee in charge:

Matthew H. Alford, Chair
Jennifer A. MacKinnon
Robert Pinkel
Sutanu Sarkar
Janet Sprintall

2021

The dissertation of Olavo Badaró Marques is approved, and it is acceptable in quality and form for publication on microfilm and electronically.

University of California San Diego

2021

EPIGRAPH

When the ebbing tide retreats
along the rocky shoreline
it leaves a trail of tidal pools
in a short-lived galaxy.
Each microcosmic planet
a complete society.
A simple kind of mirror
to reflect upon our own.
All those busy little creatures
chasing out their destinies.
Living in their pools
they soon forget about the sea.
—Neil E. Peart (1979)

TABLE OF CONTENTS

LIST OF FIGURES

LIST OF TABLES

ACKNOWLEDGEMENTS

I owe many thank-yous to my advisor Matthew Alford. For instigating my curiosity, helping me to navigate through the world of science, pushing me to do more and take different viewpoints, and carrying for my professional and personal development. With the benefit of time, I can now look back and see how far you have helped me to go. I'm also indebted to the other members of my committee, Rob Pinkel, Jennifer MacKinnon, Janet Sprintall, and Sutanu Sarkar. I have greatly benefited from their suggestions, insights, and encouragement.

My dissertation is based on observations from a large field experiment (T-TIDE) that was only possible through the incredible work of incredible people. It is hard to grasp, and even harder to put into words the breadth of the work, knowledge, and skills that led to the the execution of the experiment. In addition to my committee members who led T-TIDE, I would like to thank Dmitry Braznikov, Jonathan Nash, Shaun Johnston, Nicole Jones, Sam Kelly, Jody Klymak, Drew Lucas, Giulio Meille, Ruth Musgrave, Luc Rainville, Tamara Schlosser, Harper Simmons, Gunnar Voet, Amy Waterhouse, and Zhongxiang Zhao. Thank you for the collaborations, science discussions, and the encouragement along the way.

After many years at Multiscale Ocean Dyanmics (MOD) group, it is easy to lose perspective and take for granted the privilege of having been a part of it. As a testament to its positive environment, the group has expanded over the years and this page is not long enough to acknowledge everyone. However, I could not miss the opportunity to thank: Mike Goldin, for always being a source of inspiration; Arnaud Le Boyer, for all the fun and work in our office; and San Nguyen, for (literally) everything.

Whenever I needed, the SIO staff was always there to help me and my problems were soon gone. Thank you to Tomomi Ushii, Gilbert Bretado, and Eva Friedlander for making my journey a lot smoother.

If you go to a cruise in the Arctic, you don't want to forget your jacket. If instead you go to the tropics, you'd better bring sunscreen. If you decide to do a Ph. D., have friends by your

side. I can't thank all of you enough for all the wonderful time we've had together. I've had all the support from the incomparable 2014 PO cohort: Bia, Derek, Effie, Isa, Paul, and Stephen. Of course, I could not leave out Alan, Dillon, Gui, Jess, Jesse, Kate, Mika, and Reuben. Huge thanks to André and Tiago, whose support goes way before SIO. Special thanks also to Adonis, Bernardo, Camila, Victor, and Marília.

Thank you to all my family, in particular to Claudia, Guilherme, Danilo, Ana Mendes, Luiz (in memoriam) and Sara,

All of this journey wouldn't have been possible with all the love from sister, Diana, and my parents, Carmen and Noel. Thank you from the bottom of my heart.

Chapter 2, in full, is a reprint of the material as it appears in Journal of Physical Oceanography, 2021, DOI: 10.1175/JPO-D-20-0044.1. Marques, Olavo B.; Alford, Matthew H; Pinkel, Robert; MacKinnon, Jennifer A.; Klymak, Jody M.; Nash, Jonathan D.; Waterhouse, Amy F.; Kelly, Samuel M.; Simmons, Harper L.; Braznikov, Dmitry. The dissertation author was the primary investigator and author of this paper.

Chapter 3, in part is currently being prepared for submission for publication of the material. Marques, Olavo B.; Alford, Matthew H.; Pinkel, Robert; MacKinnon, Jennifer A.; Klymak, Jody M.; Nash, Jonathan D. The dissertation author was the primary investigator and author of this paper.

Chapter 4, in part is currently being prepared for submission for publication of the material. Marques, Olavo B.; Alford, Matthew H.; Pinkel, Robert; MacKinnon, Jennifer A.; Voet, Gunnar; Klymak, Jody M.; Nash, Jonathan D. The dissertation author was the primary investigator and author of this paper.

VITA

2013	B. S. in Oceanography, University of São Paulo, Brazil
2021	Ph. D. in Oceanography, University of California San Diego

PUBLICATIONS

Marques, O. B., Alford, M. H., Pinkel, R., MacKinnon, J. A., Voet, G., Klymak, J. M. & Nash, J. D "Near-bottom upwelling along corrugations in the continental slope of Tasmania", in prep. for *Journal of Physical Oceanography*.

Marques, O. B., Alford, M. H., Pinkel, R., MacKinnon, J. A., Klymak, J. M. & Nash, J. D., "Observations of tidally driven turbulence over steep, small-scale topography on the Tasman slope.", in prep. for *Journal of Physical Oceanography*.

Marques, O. B., Alford, M. H., Pinkel, R., MacKinnon, J. A., Klymak, J. M., Nash, J. D., Waterhouse, A. F., Kelly, S. M., Simmons, H. L., & Braznikov, D. (2021) "Internal Tide Structure and Temporal Variability on the Reflective Continental Slope of Southeastern Tasmania", *Journal of Physical Oceanography*, 51 (2), 611-631.

Alford, M. H., Simmons, H. L., **Marques, O. B.**, & Girton, J. B. (2019) "Internal tide attenuation in the North Pacific", *Geophysical Research Letters*, 46 (14), 8205-8213.

ABSTRACT OF THE DISSERTATION

From large-scale internal tides to small-scale turbulence: observations on the continental slope off Tasmania

by

Olavo Badaró Marques

Doctor of Philosophy in Oceanography

University of California San Diego, 2021

Matthew H. Alford, Chair

The dissipation of surface tides is thought to be one of the major contributors to small-scale turbulence and mixing in the abyssal ocean (below > 2000 m), which is an essential component of the large-scale deep circulation. However, the energy of surface tides is first converted into internal tides and these waves can be transformed through several processes until they break and generated mixing.

Over the course of two months in 2015, we made intensive in-situ observations to determine the energy fate of the incident internal tide on the continental slope off Tasmania, Australia. Over the steep slope in the southeast region, the incoming tide mostly reflects back to the deep

ocean. We observed a complex interference pattern that is associated with both wave reflection and the alongshore propagation of a slope wave. During our experiment, the incoming internal tide exhibits a predictable spring-neap cycle. However, the mismatch between the observed and predicted phases of the fortnightly variability indicates that local waves are also important in the internal-tide wave field.

The irregular northeastern continental slope off Tasmania leads to large scattering of the incoming internal tide. Tidal flow over a steep bump sets nonlinear lee-wave like phenomena on the offshore and onshore sides of the topography. Through these processes, the semidiurnal tide drives most of the observed energy dissipation rate. However, the temporal variability is complex on weekly timescales and may be associated with the interference between remote and local tides. Nevertheless, idealized theoretical predictions roughly agree with the observations and supports that wave scattering is responsible for the near-bottom turbulence.

Despite the high reflectivity off southeastern Tasmania, small-scale bathymetric corrugations modify the near-bottom tidal flow, which is in turn coupled with the background current. Large cross-shore tidal and subtidal velocities are observed within the trough of the corrugation. The low-frequency horizontal current is $O(10^{-2})$ m s^{-1}, which may be associated with large vertical velocities of up to $O(10^{-3})$ m s^{-1}. The temporal variability of the near-bottom subtidal current is correlated with turbulence estimates, which do not have a clear fortnight modulation. However, spatially and temporally resolving measurements show that the sloshing of the internal tide is crucial for setting the near-bottom turbulence. The vertical divergence of the semidiurnal Reynolds stress explains the temporal variability of turbulence within the corrugation trough and suggests an internal-tide driven onshore subtidal flow. The onshore acceleration is likely balanced by an offshore pressure gradient, and the associated density field is responsible for the decrease in magnitude of the overlying alongshore flow as it approaches the top of the corrugations.

Chapter 1

1.1 Introduction

Several of the broad features of the ocean circulation were sparsely measured from the late 19th century to the middle of the 20th century. Observations from extensive ship surveys were able to describe strong upper-ocean currents in the western boundary of ocean basins [Stommel, 1950], along the equator [Gellert, 1938], and around Antarctica [Deacon, 1937]. These currents were inferred from measurements of temperature and salinity, which can be combined with the equations of fluid dynamics to estimate the velocity of large-scale currents [Gill, 1982].

However, while surface currents are in direct contact with the scientists on a research vessel, observations also captured the similarity between surface waters at high latitudes with those in the deep ocean [Sverdrup et al., 1942]. In regions in the North Atlantic and around Antarctica, surface cooling (among other processes) create dense waters near the surface of the ocean that subsequently sink towards the bottom and spread throughout the global ocean. This was the beginning of our understanding of what is now known as the Meridional Overturning Circulation (MOC).

The increasing number of measurements in the late 20th century allowed a rich and quantitative description of the MOC. In terms of the zonally averaged circulation, the deep ocean circulation between the northern and southern hemispheres is composed of two overturning cells

[Lumpkin and Speer, 2007]. Both are fed from water that sinks at high latitudes and flow away from their origin. In the Southern Ocean, the densest water masses are created, and thus fill the bottom of the ocean as part of the lower overturning cell. The North Atlantic also exports water to the abyss, but at lower density relative to in the Southern Ocean, thus feeding an upper cell of the circulation. To close the overturning cells, water in the abyssal ocean must flow upwards (i.e. undergo upwelling), and eventually be transported to higher latitudes again.

However, the dynamics of the large-scale, steady circulation in the ocean interior constrain the currents to be parallel to density surfaces. Since these surfaces are nearly horizontal over much of the abyss, where and how does water get back to the upper ocean? This question has been progressively answered in the past century. This dissertation is my small contribution to this subject.

1.2 Abyssal upwelling

[Stommel, 1958] first recognized abyssal upwelling as a key ingredient of the deep ocean circulation, but without considering which processes were responsible for the upward transports. [Munk, 1966] then attempted to estimate how much upwelling could be accounted for by different mechanisms. In the author's own words: "I have not succeeded in interpreting the inferred diffusion in terms of known processes" [Munk, 1966]. Nevertheless, these landmark papers recognized that small-scale turbulent processes could be responsible for abyssal upwelling and thus contribute to large-scale features of the ocean. In other words, transient phenomena can lead to mixing across density surfaces, and lead to the net upward mass transport that is part of the time-mean circulation.

Several complementary approaches have been pursued to address diapycnal mixing in the ocean. Sensors that can resolve temperature and velocity fluctuations over horizontal scales of centimeters have been developed to directly measure small-scale turbulence [Gregg, 1991].

Tracers can be purposefully released and diffusion can be measured by tracking the tracer cloud over time [Ledwell et al., 1993]. Large-scale observations coupled with conservation equations can be used to infer basin-wide upwelling averages [Ganachaud and Wunsch, 2000].

In the last few decades, some general patterns of abyssal mixing have emerged. Direct measurements are now sufficient to produce basin-wide averaged diffusivities that are consistent with estimates inferred from large-scale constraints on the ocean circulation. However, temporally averaged deep-ocean turbulence is highly variable in space and largely associated with rough topography. Where turbulence is strong, diapycnal diffusivities are larger than over smooth topography by a few orders of magnitude. The turbulence is often bottom-enhanced over $O(100) - O(1000)$ m, although it can extend throughout the water column [Polzin et al., 1997, Waterhouse et al., 2014, Kunze, 2017]

Although the magnitude of the observed abyssal diffusivity can account for the lower overturning cell, the bottom-enhanced profiles leads to an apparent paradox. If water parcels mix more vigorously with denser water from below than with lighter water from above, then a bottom-enhanced mixing profile induces downwelling instead of the expected upwelling. To resolve this conundrum, mixing near the bottom must be taken into account [Ferrari et al., 2016]. For example, the argument that leads to downwelling is not valid if the water parcel is bounded from below by the seafloor. Nevertheless, while there has been substantial progress in the last few years, it is still unclear how to properly account for net abyssal upwelling.

In addition to the much richer description of the patterns of mixing that have evolved since [Munk, 1966], the questions about which processes fuel turbulence are also being answered. On one hand, the adiabatic upwelling in the upper overturning cell does not require small-scale turbulent processes in the interior. On the other hand, several processes can interact in a variety of ways with bottom topography and ultimately contribute to abyssal mixing. Winds at the surface power near-inertial waves that can propagate downwards and break over rough topography [Clément et al., 2017]. Near-bottom flows of the large-scale circulation can also generate internal

waves that can account for mixing [Cusack et al., 2017]

While there are large uncertainties on which processes account for deep ocean turbulence, the dissipation of surface tides is relatively well constrained (3.5 TW, [Wunsch and Ferrari, 2004]). Most of the tidal dissipation takes place on shallow seas. However, around 1 TW is converted into internal tides and their breaking is thought to be an important energy source for abyssal mixing [Whalen et al., 2020].

1.3 Internal tides

As surface tides slosh back and forth over sloping topography, the density field is perturbed and internal waves are generated. Depending on several factors, such as the steepness of the seafloor [Sarkar and Scotti, 2017] or the velocity of the subtidal current [Shakespeare, 2020], the generated internal waves can have quite distinct features. In particular, the wave response that propagates away from its generation site at the tidal frequency is known as internal tide.

At any specific frequency, internal waves are not restricted to a single corresponding wavelength. However, longer waves (i.e. low modes) propagate faster than shorter ones (i.e. high modes). Moreover, the faster internal tides also tend to be more stable to perturbations and are likely to propagate further away.

These differences have been crucial to address the energy fate of tidal dissipation. For internal tides generated over short topographic features, a relatively large fraction of the energy flux goes to high modes, which break closer to their generation sites. In contrast, surface tidal flow over tall ridges induce a relatively larger flux into low-mode waves, which can propagate for up to thousands of kilometers [Zhao et al., 2016, Alford et al., 2019]. While the high modes can break locally and induce large turbulence relative to the ocean interior [Klymak et al., 2006], the fate of low-mode waves is unclear.

Interestingly, internal tides in the first couple of modes can be globally mapped from

satellite altimetry [Zhao et al., 2016, Zhao, 2018]. Nevertheless, these data are not able to track the instantaneous temporal evolution, such that the energy budget for low-mode internal tides is hard to constrain. Considering their long-range propagation, these waves can reach continental margins and undergo several transformations determined by the shape of the seafloor [Klymak et al., 2011]. Therefore, understanding how low-mode internal tides are modified by the continental slope may be important to determine the fate of their energy flux, where they break, and how the induced turbulence might contribute to mixing in the ocean.

To study internal tides upon reaching a continental slope, a fieldwork experiment was designed to make observations on the continental slope off eastern Tasmania [Pinkel et al., 2012]. This region was chosen because it has a fairly well-defined remote semidiurnal internal tide source, which is located south of New Zealand. Energetic internal tides are generated at the tall Macquarie Ridge and a mode-1 tidal beam propagates over 1400 km until reaching Tasmania. The overarching goal of the Tasman Tidal Dissipation Experiment (T-TIDE) is to determine the energy fate of the incident internal tide on the continental slope and study the relevant near-bottom dissipation processes. In the following chapters, I will present some of the main results from T-TIDE.

1.4 Dissertation outline

This dissertation contains three somewhat independent manuscripts focusing on different aspects of the internal tide on the continental slope off Tasmania.

Chapter 2 investigates the semidiurnal energetics on the southeastern continental slope. Previous T-TIDE work has shown that most of the incident flux is directed towards this region, where it primarily reflects back from the steep topography, in addition to exciting a slope wave. The in-situ observations support previous results and highlight new features of the internal tide. The large reflectivity is inferred from the characteristic standing wave interference pattern. A

significant departure from this pattern is an offshore energy flux, that is associated with the slope wave. While interference patterns have been described in other regions, we provide a more detailed description of the standing wave on a sloping bottom using results from models and observations. The observations also capture that the internal tide energy vary over spatial scales of $O(1)$ m due to small-scale bathymetric corrugations. The temporal variability of the internal tide is largely associated with the spring-neap cycle, which indicates the propagation of the remote internal tide was did not substantially vary over the period of the experiment. Nevertheless, the observed phase of the spring-neap cycle does not agree with the theoretical expectation, and we attribute the mismatch to interference with the local tide.

In chapter 3, we turn to the observations around a small-scale bump in the northeastern region of the slope. On a larger scale, the continental slope is irregular and previous work has identified the incident mode-1 internal is almost entirely scattered to higher modes. The in-situ observations address the nonlinear tidal response and near-bottom turbulence across the bump. These observations are unique in that we resolved both the temporal and spatial variability of transient, small-scale tidal processes. Their structure is sensitive to the different bottom slopes on each side of the bump and may also depend on the background current. The semidiurnal tide drives most of the near-bottom turbulence. However, tides and and dissipation are not modulated by a spring-neap cycle, which may be associated with the interference between local and remote waves. We also show that idealized theory for internal tide scattering over steep topography roughly agrees with the observed nonlinear tidal response and near-bottom dissipation.

Chapter 4 revisits the observations in chapter 2, but with special attention on the processes induced by the small-scale corrugation. A persistent subtidal onshore flow is observed within the corrugation trough. Over the sloping bottom, the inferred vertical velocity is large and up to $O(100)$ m day^{-1}. The noise in direct vertical velocity measurements is too big to confirm the estimate, but are not entirely inconsistent with it. Turbulence is also enhanced within the corrugation trough and correlated with the subtidal velocity. Although the temporal variability

of the near-bottom flow and turbulence do not exhibit a spring-neap cycle, the sloshing of the internal tide within the corrugation trough is an essential mechanism for near-bottom turbulence. These different pieces of the data are reconciled through the onshore acceleration of the subtidal flow by the internal tide. Although we couldn't close the momentum budget, an opposing pressure gradient likely balances the internal tide forcing. The resulting slope of density surfaces acts to create a slippery boundary layer on the overlying alongshore flow. Finally, our turbulence estimates suggest that mixing can only sustain a vertical velocity of up to $O(1)$ m day^{-1}, which is negligible relative to our previous estimate, but large compared to basin-wide averages of diapycnal upwelling.

Chapter 2

Internal tide structure and temporal variability on the reflective continental slope of southeastern Tasmania.

2.1 Introduction

Surface tides, through the generation and subsequent breaking of internal tides, are thought to provide a significant contribution of the ~2 TW of power required to maintain deep-ocean diapycnal mixing and the observed abyssal stratification [Munk and Wunsch, 1998]. In turn, diapycnal mixing plays a key role in both the vertical and horizontal circulations at depth [Lumpkin and Speer, 2007, Melet et al., 2016]. Thus, a better understanding of the energy pathways that ultimately drive diapycnal mixing is necessary to improve our models of the global circulation, in particular, of the lower Meridional Overturning Circulation [MacKinnon et al., 2017].

In contrast to the high-wavenumber internal tides [Vic et al., 2019], mode-1 waves propagate away from their generation sites for hundreds to thousands of kilometers and redistribute the energy available for deep-ocean mixing across the ocean basins [Ray and Mitchum, 1996,

Alford, 2003, Zhao et al., 2016, Alford et al., 2019]. After long-range propagation, low-mode internal tides may reach continental slopes where several processes associated with tide-topography interactions can play a role in the wave energy budget. [de Lavergne et al., 2019] parameterized some of these processes and found that internal-wave breaking on continental slopes can account for 10-15% of global tidal dissipation.

Understanding the processes that determine the fate of the remote internal tide energy upon impinging on the continental slope is the goal of the Tasman Tidal Dissipation Experiment, T-TIDE [Pinkel et al., 2015]. Observations and numerical models have been used to study different aspects of the internal tide generated at Macquarie Ridge, which then propagates ~1400 km towards Tasmania.

Macquarie Ridge has been shown to be strong a generation site in satellite observations [Egbert and Ray, 2000], theoretical [Morozov, 1995] and numerical models [Niwa and Hibiya, 2001, Simmons et al., 2004]. From a regional analysis of altimeter data, [Zhao et al., 2018] characterized the spatial variability of internal-tide generation along the ridge and calculated that a M_2, mode-1 energy flux of ≈1 GW propagates towards Tasmania (Fig. 2.1a). In addition to good agreement with the altimetry-based estimate, energy flux from in-situ observations in the center of the basin also show a spring-neap cycle, which is consistent with radiation of M_2 and S_2 internal tides from Macquarie Ridge [Waterhouse et al., 2018]. From numerical simulations, [Klymak et al., 2016] found that the incident wave is diffracted before it arrives on the continental slope, leading to larger (smaller) flux towards southeastern (northeastern) Tasmania (reproduced in Fig. 2.1b). Coincidentally, the region with the largest incoming energy flux also has highest modeled reflectivity, where ≈80% of the incoming mode-1 internal tide energy flux reflects as mode-1.

Previous observations have been used to characterize the internal tide on the eastern Tasman slope and corroborate the large reflectivity of its southeastern sector. Glider observations by [Boettger et al., 2015] indicate the source of the internal tide is primarily remote as opposed to local

generation on the continental slope. More extensive glider observations by [Johnston et al., 2015] show standing wave features in the cross-slope structure of internal-tide energy, characteristic of high reflectivity. Their reflectivity estimate (90%) is higher than those based on satellite altimetry (60%, [Zhao et al., 2018]) and numerical simulations (80%, [Klymak et al., 2016]). Furthermore, [Johnston et al., 2015] identified a northward propagating (approximately alongslope) internal tide, which [Klymak et al., 2016] identified as an edge wave generated by the remote forcing on the slope.

Despite recent observations on eastern Tasmania, the sampling of available glider and satellite observations has precluded a description of the internal tide temporal variability. In particular, altimetry-based energy flux estimates are only calculated from the sea-surface height tidal signal that has constant amplitude and phase at any given location (i.e. the stationary signal[1]). On one hand, if lunar (M_2) and solar (S_2) internal tides have amplitudes and phases that are constant, then the only temporal variability that would be observed is due to their beating (i.e. the spring-neap cycle). On the other hand, processes such as wave-mean flow interactions (e.g. [Duda et al., 2018]) or variable internal-wave generation (e.g. [Zilberman et al., 2011]), can create nonstationary variability of the internal tide, which requires more comprehensive ocean models for accurate prediction. Therefore, it is not known whether the stationarity assumption of current internal-tide energy budgets [de Lavergne et al., 2019] is a good approximation for the Tasman slope.

In-situ observations [Johnston et al., 2015] have focused on the horizontal variability of the internal tide over O(10-100) km instead of its vertical structure on the continental slope. Regions where the internal tide energy is bottom-enhanced may trigger more tidally driven turbulence near the bottom. These regions may be determined by several processes associated with tide-topography interactions. For example, small-scale topography can lead to wave breaking [Nash et al., 2007] and interactions of the remote internal tide with the local surface tide can

[1]Note that standing waves are also known as stationary waves. Instead, we reserve the term stationary for a tidal signal with constant amplitude and phase.

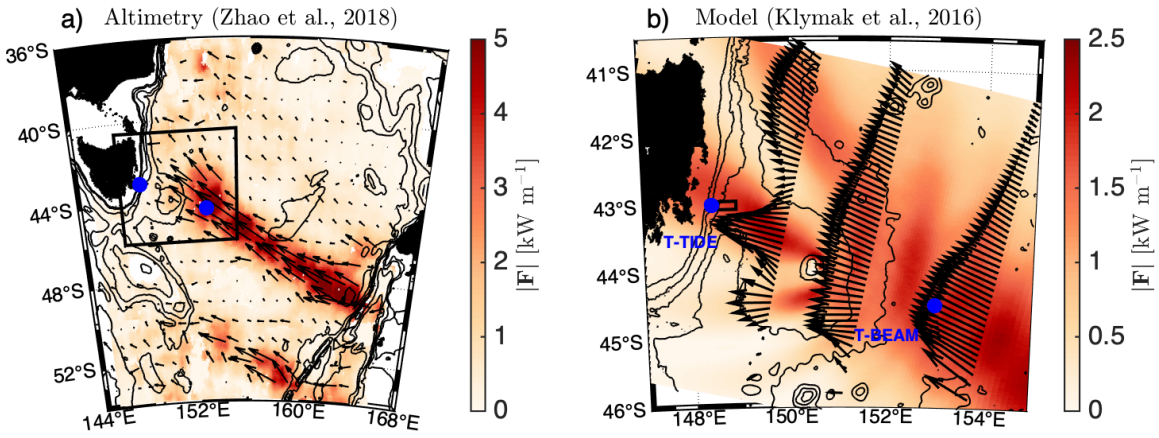

Figure 2.1: Incident internal tide on the Tasman slope. (a) Stationary, M_2, mode-1 depth-integrated energy flux from satellite altimetry [Zhao et al., 2018]; (b) Modeled [Klymak et al., 2016] incident depth-integrated energy flux inside the black rectangle in (a). The East Tasman Plateau (with water depths as shallow as 1000 m at 150.5°E and 44°S) diffracts the incoming internal tide beam and leads to variable energy flux along Tasmania. Note the upper colormap limit in (b) is smaller than in (a). Blue dots show the mooring locations from T-TIDE (that we present in this paper) and T-BEAM [Waterhouse et al., 2018]. The black rectangle in (b) is the region shown in Fig. 2.2a.

change the internal wave generation on the slope [Kelly and Nash, 2010]. Identifying which processes are relevant is an important step towards improving energy budgets of the internal tide on the continental slope.

In this paper, we present new in-situ observations from T-TIDE and, along with a hierarchy of models, further describe the reflection process on the southeastern Tasman slope. In particular, our two-month long mooring observations capture the bottom-enhanced tidal energy in the reflective portion of the continental slope and provide an estimate of the temporal variability. In addition to being broadly consistent with a standing wave, our observations show that (i) both the standing wave and small-scale topography lead to bottom-enhanced energy, (ii) the tidal energy is primarily stationary and (iii) the spring-neap cycle is a function of the complex interference between between remote and local tides.

We proceed by describing our measurements, the numerical models we use to compare with observations, and the analysis methods (Section 2.2). We then present model predictions of the standing wave pattern (2.3a), the observations (Section 2.3b) and the overall agreement

between them (Section 2.3c). In addition to the large-scale structure of the standing wave, bathymetric corrugations lead to significant spatial variability of near-bottom energy density at small spatial scales (Section 2.3d). From the temporal variability of internal-tide energetics (Section 2.3e), we show that the internal tide is primarily stationary, but the observed timing of the spring-neap cycle does not match with the prediction from the group-velocity across the Tasman Sea. We use simple trigonometric calculations to argue this mismatch is a result of interference between the remote internal tide with the local tide on the slope (Section 2.3f). We conclude with a brief discussion of the incident energy flux (Section 2.4) and the summary of our results (Section 2.5).

2.2 Methods

The T-TIDE field experiment took place between January and March of 2015. We carried out extensive observations along eastern Tasmania, focusing on two regions on the slope where we deployed 10 moorings and occupied several CTD-lowered acoustic Doppler current profiler (CTD-LADCP) stations and transects.

We will present observations from three moorings and one station in southeastern Tasmania (Fig 2.2). In an alongslope averaged sense, the bathymetry has a concave shape, with supercritical topography ($\gamma > 1$, see Fig. 2.2) in the upper part of the continental slope and subcritical ($\gamma < 1$) further offshore. Three subsurface moorings were deployed on the upper half of the continental slope, where the mean water depth is 1170 meters (Table 2.1) and the slope is locally supercritical. While the moorings were deployed at roughly the same cross-slope location (relative to the width of the continental slope), two moorings (T5 and T6) were deployed in a corrugation trough and the other (M5) on the adjacent crest of the bathymetry.

Moorings T5 and T6 were each instrumented with two downward-looking acoustic Doppler current profilers (ADCPs): a 300-kHz RDI Workhorse measuring the bottom 100 meters of the

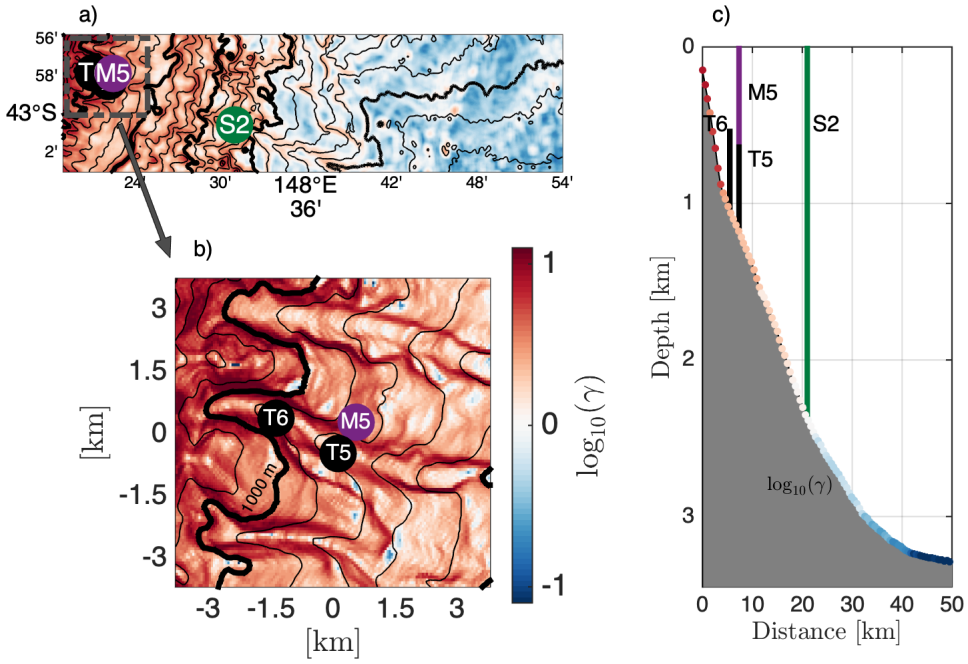

Figure 2.2: Observation sites. (a) Bottom criticality (γ) map to the semidiurnal internal tide with mooring (purple and black dots) and CTD/LADCP station (green dot) sites. (b) Same as (a), but zoomed in around mooring sites. (c) Continental slope of southeastern Tasmania (bathymetry averaged in the along-slope direction over 10 km). $\gamma \equiv |\beta|/s$, where $|\beta|$ is the absolute value of the bottom slope and $s \equiv \sqrt{(\omega_{M_2}^2 - f^2)/(N_b^2 - \omega_{M_2}^2)}$ is the slope of internal-wave characteristics (where ω_{M_2} is the semidiurnal lunar frequency, f is the Coriolis frequency, and N_b is the buoyancy frequency at the bottom). We have calculated N_b from the *World Ocean Atlas* [Boyer et al., 2013]. In (a) and (b), bathymetry is contoured every 100 meters (with thick contours every 500 meters). In (c), the solid black vertical lines extend over the depth range of available observations at T5 and T6.

Table 2.1: Mooring (M5, T5 and T6) and CTD/LADCP station (S2) obervations on the southeastern Tasman slope.

	lon (°E)	lat (°S)	bottom depth (m)	observed depth range (m)
M5	148.3749	42.9641	1140	10-1130
T5	148.3696	42.9708	1238	610-1228
T6	148.3511	42.9633	1136	495-1126
S2	148.5168	43.0088	2505	20-2480

water column and a 75-kHz RDI Longranger for the adjacent 500 meters above (Fig 2.3a,b). Throughout the combined depth range of the ADCPs, each mooring was instrumented with around 40 Seabird (SBE)-56 thermistors and two SBE-37 MicroCAT CTDs. The vertical spacing of thermistors is highest over the bottom 150 meters (10-meter resolution), while they were deployed farther apart higher up on the mooring. The CTDs were deployed near the top and bottom of the mooring line, providing pressure records to estimate the depths of the thermistors. Moreover, moored and shipboard CTD data were used to calculate a 3rd-order polynomial fit to estimate salinity and potential density from the temperature data measured by the thermistors.

Mooring M5 was instrumented with an upward-looking 300-kHz RDI Workhorse ADCP, measuring the upper 100 meters of the water column, as well as two McLane Moored Profilers (MMPs) profiling below (Fig 2.3c). A few SBE-56 and RBR-Solo thermistors, a SBE-37 CTD and an Aanderaa model 8 recording current meter (AA-RCM8) were deployed above and below the profiling depth limits of each MMP for assessing mooring knockdown and cross-calibration. The nominal profiling depth ranges of the MMPs were 100-800 meters and 820-1130 meters, and with a profiling speed of 0.25 m s^{-1}, the temporal resolutions at mid-profile are about 45 and 20 minutes, respectively. Each MMP carried a standard Falmouth Scientific Inc. (FSI) CTD and velocity in the upper and lower MMPs was measured by a FSI acoustic current meter (ACM) and a Nortek Aquadopp profiler, respectively.

Large currents (> 0.4 m s^{-1}) around yeardays 19 and 52 coincide with times when the MMPs at M5 could not profile along the mooring (Fig 2.3c). At these times, a moored CTD near the surface indicates mooring knockdown of up to 300 meters. Moreover, due to issues with the clock in a current meter, velocity measurements between 600 and 800 meters in mooring M5 are only available when the MMP is profiling downwards (Fig 2.3c).

We also conducted a tidally resolving CTD/LADCP station (S2) at a water depth of 2505 meters, about 15 km offshore from the moorings. The station was occupied for 23.5 hours (on yearday 25) and a total of 32 nearly full water column profiles were taken. Along with the

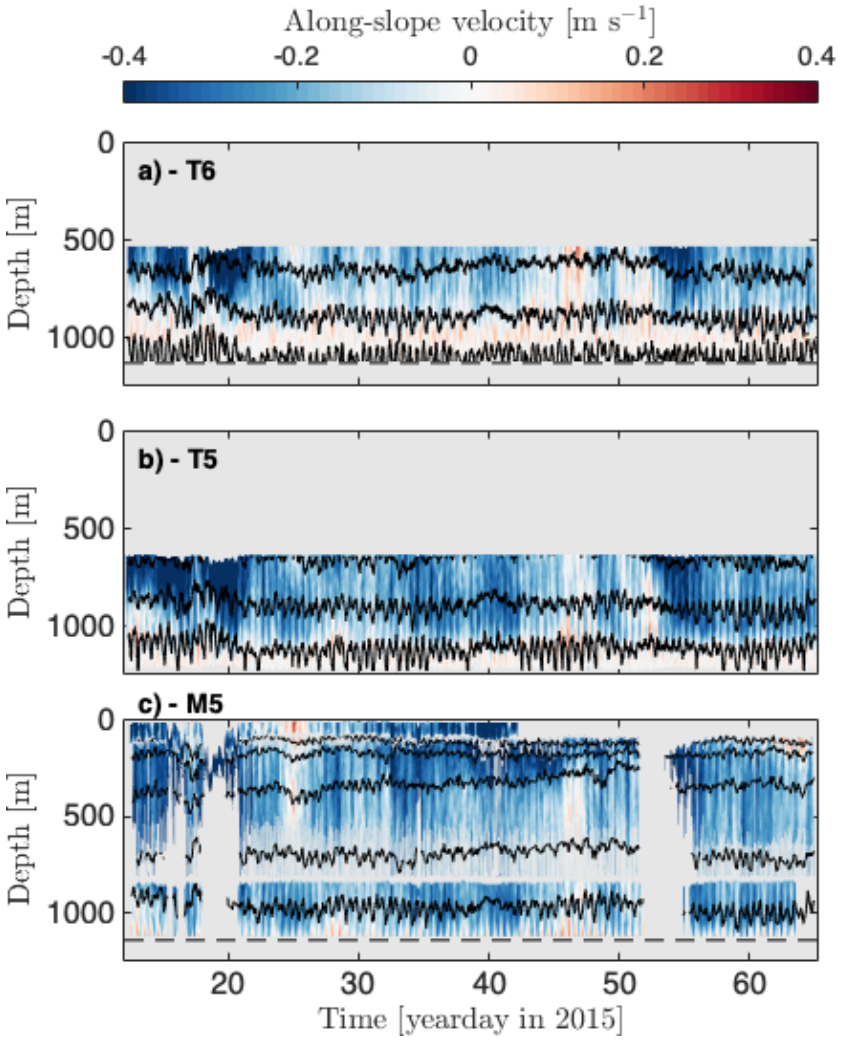

Figure 2.3: Moored data from southeastern Tasmania (see Fig. 2.2 and Table 2.1 for deployment sites). Evenly spaced isopycnals are shown by the black contours. The along-slope direction is 12° clockwise from the north. The common depth axes extend to the bottom depth at T5 and horizontal dashed lines indicate the water depth at the other two moorings. Mooring M5 was deployed on the crest of a bathymetric corrugation while T5 and T6 in a trough, where along-slope flow is blocked in the bottom ~100 meters. Due to instrument issues, velocity between 600 and 800 meters from mooring M5 is only available when the MMP is profiling downwards.

moorings, these data provide information on the cross-slope internal tide energetics.

2.2.1 Linear scattering model

We will present internal tide energetics from the Coupling Equations for Linear Tides (CELT) model [Kelly et al., 2013] to address how the simple standing wave solution due to reflection from a vertical wall is modified by the slope of southeastern Tasmania. Briefly, CELT is a linear scattering model for one-dimensional topography, which is based on matching normal modes across topographic steps under the appropriate boundary conditions. The reader is referred to [Kelly et al., 2013] for further details.

CELT was run with realistic bathymetry from southeastern Tasman slope (averaged in the along-slope direction over 10 km around the site of the observations) discretized with 500-meter horizontal resolution and with adjacent flat bottoms in the deep ocean and the continental shelf. The buoyancy frequency is horizontally uniform and calculated from the *World Ocean Atlas* [Boyer et al., 2013]. The imposed forcing is a mode-1, M_2 internal tide propagating from the deep ocean and we have solved the scattering problem for 100 (surface and internal) modes (from a posteriori analysis, 100 modes is enough to calculate smooth velocity fields). The depth-integrated energy flux of the incoming wave was set to 1.7 kW m^{-1}, which is the same incident flux in the model by [Klymak et al., 2016].

2.2.2 Regional numerical model

In addition to CELT, we will also compare our observations with the model from [Klymak et al., 2016] that has realistic two-dimensional bathymetry of the Tasman slope (hereafter referred to K16). The model is the MITgcm [Marshall et al., 1997], with lateral resolution of 1 km on the slope and a stretched vertical coordinate with 200 grid cells. The forcing is an idealized internal-tide beam, tuned to have a width broadly consistent with that observed from

satellite altimetry, ≈300 km [Zhao et al., 2018], but with a relatively small incident energy flux to investigate the linear response of the continental slope. The incident energy flux at the moorings site is 1.7 kW m^{-1} (Fig. 2.1b), which is a factor of two smaller than in-situ [Waterhouse et al., 2018] and satellite altimetry [Zhao et al., 2018] observations. We refer the reader to [Klymak et al., 2016] for further details.

To compare model with observations we regridded the model output onto a height above the bottom grid and averaged over 10 km along the slope. We then calculated internal tide energy density and flux (as described below in Section 2.2d). Along-slope averaging removes relatively high wavenumber waves, which are hard to compare with observations for several reasons. For example, with a 1-km horizontal resolution the model does not fully resolve the small-scale topographic corrugations. Therefore, along-slope averaged energetics provides a more robust comparison with the data than the model output extracted from a single location.

2.2.3 Data processing

Throughout this paper, buoyancy frequency ($\overline{N}$) refers to that calculated from the background temperature and salinity fields (using the Gibbs-SeaWater Oceanographic Toolbox, [McDougall and Barker, 2011]). We define “background" as the temporal average over 3-day windows (denoted by the overbar in $\overline{N}$). Vertical isopycnal displacement (η) is calculated from the difference between observed and background depths of potential density surfaces.

Semidiurnal velocity and isopycnal displacement were calculated from harmonic fits with a sliding 3-day window to depth-gridded data. For each segment, the harmonic fit solves for amplitudes of a linear trend as well as variability at semidiurnal, diurnal and inertial frequencies (with equivalent periods of 12, 24 and 17.5 hours, respectively). The bandwidth associated with this window length is narrow enough to separate semidiurnal and inertial frequencies (at the latitude of our observations), but wide enough to encompass all semidiurnal variability. Thus, though we do not filter in the frequency domain, we will refer to these semidiurnal timeseries

as “bandpassed" (which will be denoted with the subscript D_2). Following [Martini et al., 2011], this bandpass approach avoids time-gridding MMP data, which have uneven and depth-variable temporal resolution.

Under the flat-bottom approximation, the internal tide (baroclinic) horizontal velocity ($\mathbf{u}_{\mathrm{BC}}$) can be calculated by subtracting the depth-averaged velocity (barotropic, $\mathbf{u}_{\mathrm{BT}}$) from the total velocity. With observations throughout most of the water column, both the barotropic and baroclinic components can be directly calculated (e.g. [Pickering et al., 2015]). When data gaps in the vertical are significant, fits to standard vertical modes can be used to calculate low-mode internal tide velocities (e.g. [Waterhouse et al., 2018]). In both cases, observations throughout the water column, specially in the upper few hundred meters [Nash et al., 2005], are necessary for reliable estimates of $\mathbf{u}_{\mathrm{BT}}$ and $\mathbf{u}_{\mathrm{BC}}$.

Only one of our moorings (M5) meets this requirement. Even in that case, there are significant data gaps until yearday 21 and around 52, and no data from the ADCP near the surface is available in the last 3 weeks of deployment. Moreover, though $\mathbf{u}_{\mathrm{BC}}$ is a justifiable definition for internal-tide velocities over a flat bottom, either freely propagating and coastally trapped internal waves on a sloping bottom may have a non-zero depth-integrated velocity [Musgrave, 2019].

Hereinafter we will refer to the total semidiurnal signal (i.e. $\mathbf{u}$) as the internal-tide velocity. Though this is not ideal, we do not have a reliable estimate of $\mathbf{u}_{\mathrm{BT}}$ for most of our dataset and, even worse, $\mathbf{u}_{\mathrm{BC}}$ may not be a valid definition for internal-tide velocity on the slope. Moreover, our results do not change qualitatively by subtracting the surface-tide velocities from the TOPEX/Poseidon Global Inverse Solution (TPXO) 7.2 [Egbert and Erofeeva, 2002] from the observed semidiurnal velocities.

The horizontal kinetic energy (HKE) and (linear) available potential energy (APE) are defined by

$$HKE(z,t) = \frac{\rho_0}{2}\langle \mathbf{u}\cdot\mathbf{u}\rangle \tag{2.1}$$

and

$$APE(z,t) = \frac{\rho_0}{2}\overline{N}^2\langle\eta^2\rangle, \tag{2.2}$$

respectively. ρ_0 is a constant reference density (1025 kg m^{-3}) and the angle brackets denote temporal averaging over a semidiurnal period. This averaging procedure implies that energy only varies on timescales longer than a semidiurnal period.

The nearly full water column extent of observations at M5 also allows us to calculate the internal-tide horizontal energy flux, i.e.

$$\mathbf{F}(z,t) = \langle p\mathbf{u}\rangle, \tag{2.3}$$

where p is the pressure perturbation calculated from vertical integration of η [Kunze et al., 2002].

Caveats analogous to those presented for the calculation of internal-tide velocity on a sloping bottom apply for the pressure perturbation estimates. Nevertheless, we will show our energy flux estimates are qualitatively consistent with the expected standing-wave pattern, which gives confidence on the validity of the calculations.

2.2.4 Stationarity metric

In addition to the bandpassed semidiurnal signals described earlier, we also solve for the amplitude and phase at M_2 and S_2 frequencies from harmonic fits to our entire timeseries, which are sufficiently long (≈50 days) to resolve these tidal frequencies. We define the stationary tidal signal as the results from these harmonic fits and we refer to their sum as the stationary spring-neap cycle (which will be denoted with the subscript M_2S_2).

Stationary HKE and APE are calculated from stationary velocity and displacement. For constant displacement variance, temporal variability of $\overline{N}$ leads to changes in stationary APE (and total energy). In our observations, this temporal variability is significantly smaller than the spring-neap cycle between semidiurnal constituents.

Similar to [Nash et al., 2012], we quantify stationarity with the skill score [Murphy, 1988], i.e.,

$$\mathrm{SS}_{x_{\mathrm{M_2S_2}}} = \left[1 - \frac{\mathrm{var}\left(x_{\mathrm{D_2}} - x_{\mathrm{M_2S_2}}\right)}{\mathrm{var}\left(x_{\mathrm{D_2}}\right)}\right], \tag{2.4}$$

where x is the variable for which the stationary metric is computed (e.g. HKE), the subscript $\mathrm{D_2}$ denotes the semidiurnal band and $\mathrm{M_2S_2}$ the stationary signal. If the stationary signal is equal to the semidiurnal energy, the former captures all of the variance of the latter and $\mathrm{SS}_{E_{\mathrm{M_2S_2}}} = 1$. If $x_{\mathrm{D_2}}$ and $x_{\mathrm{M_2S_2}}$ are anticorrelated, the skill score is negative.

2.3 Results

2.3.1 Modeled interference patterns

Before presenting the observed internal tide, it is instructive to look at idealized expectations for energy density and flux from models with varying degrees of realism. Our goal in this section is to provide background for interpreting the observations by relating the modeled spatial structures of the internal tide to the setup and limitations of each model.

The well-known analytic solution of wave reflection from a vertical wall (dotted lines in Fig. 2.4a-d) shows that energy density and flux in a standing wave are oscillatory as a function of distance from the wall [LeBlond and Mysak, 1981, Nash et al., 2004, Johnston et al., 2015]. The cross-slope flux component does not have an oscillatory structure because it is identically zero. This result contrasts with the spatially constant energetics for a single wave, such that the ratio between HKE and APE is a useful diagnostic of wave interference [Nash et al., 2004, Martini et al., 2007, Alford and Zhao, 2007b, Klymak et al., 2011]. For a complete derivation of this simple model's solution, the reader is referred to Appendix A in [Johnston et al., 2015][2].

[2]Note the derivation in [Johnston et al., 2015] has two minor mistakes: in their notation, assuming k is the magnitude of the zonal wavenumber component, the complex amplitude of $v_{w,e}$ in equation (A1) should be $\omega l \pm i f k$; in equations (A3) and (A5), instead of a common amplitude factor C, velocity components u_t and v_t should have amplitude factors $C_u = \sqrt{(\omega k)^2 + (fl)^2}$ and $C_v = \sqrt{(\omega l)^2 + (fk)^2}$, respectively.

Despite the sloping bottom, potentially different responses to one and two-dimensional topographies, and the partial mode-1 reflectivity of 83%, oscillatory patterns of energy density and along-slope energy flux in CELT and K16 are broadly similar to the wall model (Fig. 2.4a-d). Around the sites of our observations (vertical bars in Fig. 2.4 a-d), all solutions have primarily southward energy flux and the ratio between HKE and APE increases towards deeper water. In contrast to the wall model, reflection is distributed across the slope and little energy gets to the shelfbreak (as indicated by APE approaching 0 instead of a finite value at $x = 0$, Fig. 2.4b).

From CELT (Figs. 2.4e-h), the internal tide response to one-dimensional bathymetry leads to bottom-enhanced energy density and flux around the moorings site (7 km from the shelfbreak). At this location, larger near-bottom tidal energy is a result of both (i) offshore-propagating scattered waves and (ii) the seafloor crossing the depth level of the deep-ocean mode-1 APE maximum (i.e. the profile of the incoming mode-1 wave at 3300 meters has maximum APE at $\approx$1000 meters). The geometric effect (ii) can be thought of as reminiscent of the interference pattern from a vertical wall, where both incident and reflected waves are mode-1. As a result from two distinct mechanisms, the interference pattern is such that HKE is enhanced near the bottom at the mooring sites over a shorter vertical scale than APE.

Energy density and the along-slope energy flux in K16 is similar to CELT (Fig 2.4e-g, i-k) and can thus be explained by the internal tide response in the cross-slope direction only. However, the cross-slope energy flux in the two models have opposing directions (Fig. 2.4c, g, k). CELT has a (small) net onshore energy flux because the reflectivity is not 100%. K16 has a net offshore energy flux around the location of the observations, but the sign of this component varies in the along-slope direction (Fig. 2.5). The $\approx$100km along-slope wavelength in the cross-slope energy flux is consistent with a slope wave on the Tasman slope, which can be excited by the incident internal tide [Klymak et al., 2016]. Since the model is stationary, dissipation is relatively small, and reflectivity is large, an energy budget implies the cross-slope energy flux at some distance from the shelfbreak is balanced by the along-slope gradient of the along-slope flux (Fig. 2.5c).

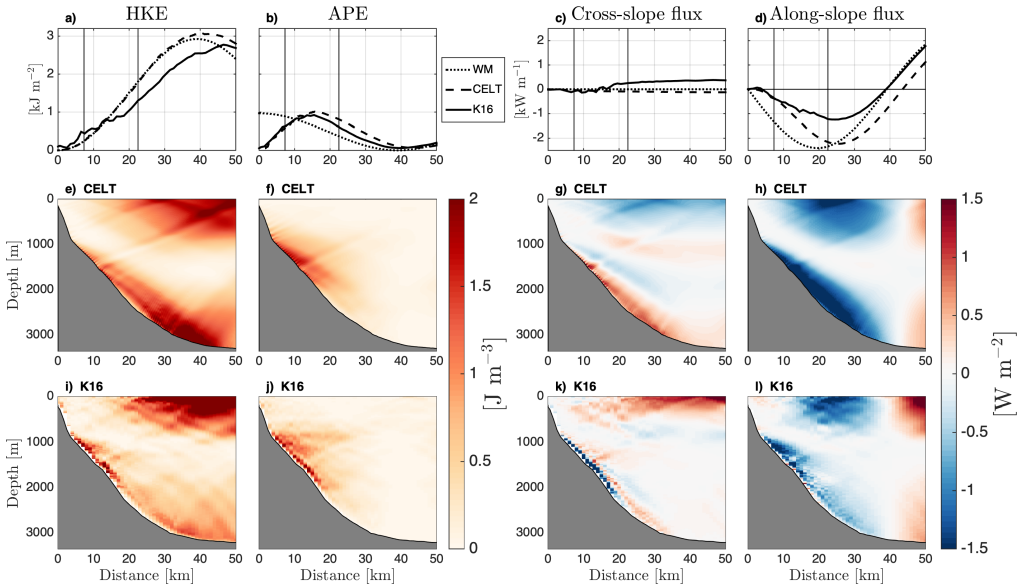

Figure 2.4: Modeled cross-slope structures of M_2 energy density and flux for the southeastern Tasman slope from a simple model with a vertical wall (WM), a linear scattering model (CELT) and a three-dimensional numerical simulation (K16). Depth-integrated (a) horizontal kinetic energy, (b) available potential energy, (c) cross-slope energy flux and (d) along-slope energy flux. (e)-(h) The correspondent depth-distance distributions of energy density and flux from CELT and (i)-(l) from K16. The vertical bars in (a)-(d) indicate the sites of observations (see Fig. 2.2). Positive energy flux in (c) and (d) are directed offshore and into the page (primarily northward for the Tasman slope), respectively. The location of the wall for the wall model is set to x = 2.5 km.

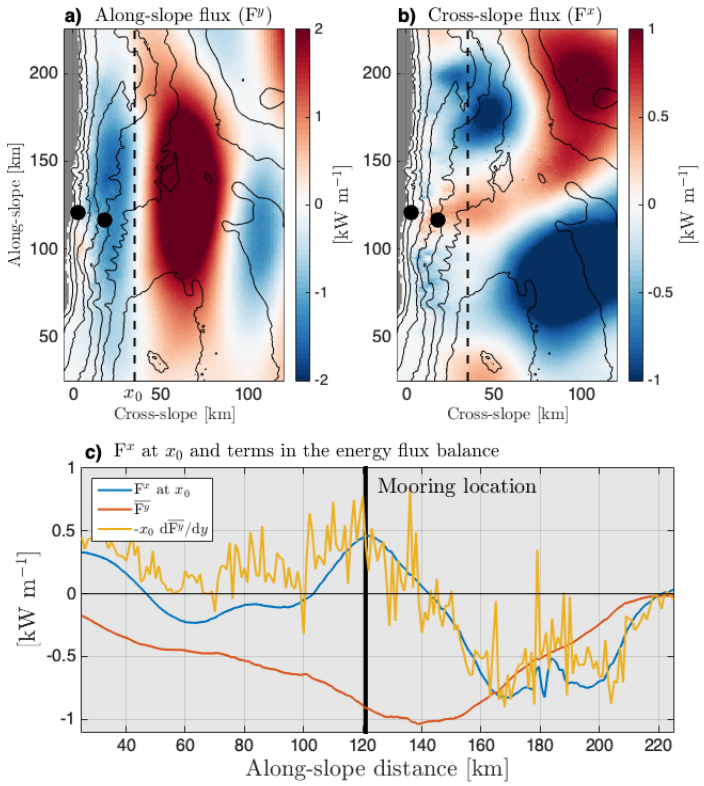

Figure 2.5: Spatial variability of the modeled (K16) depth-integrated energy flux in southeastern Tasmania. (a) Along-slope component of the energy flux, (b) cross-slope component, (c) cross-slope flux at x_0 and terms in the energy balance. Maps (a) and (b) are shaded for water depths less than 200 meters and the dots show the sites of the observations. While a standing wave (Fig. 2.4d) explains the cross-slope structure of the along-slope flux, the cross-slope component has more complex spatial variability. Assuming small dissipation, the divergence of the depth-integrated energy flux in K16 is approximately 0. Due to large reflection, the cross-slope (F^x) at x_0 is proportional to the along-slope gradient of the mean along-slope flux between the shelbreak and x_0 ($d\overline{F^y}/dy$, where the overbar denotes the averaging operation).

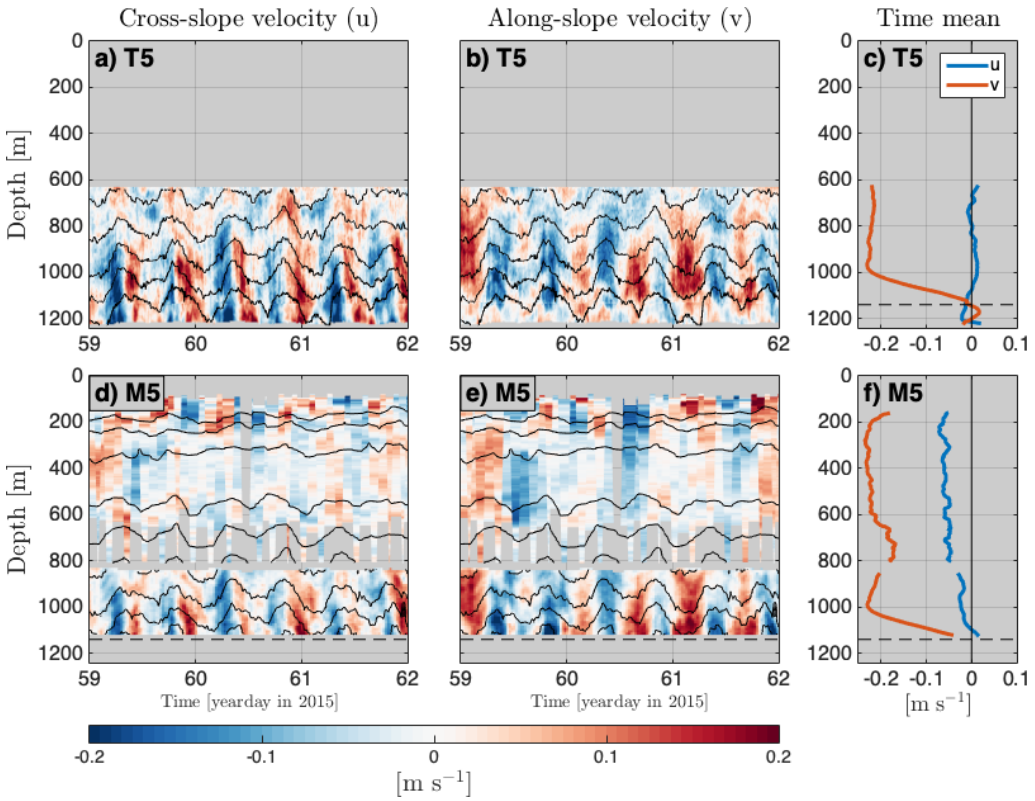

Figure 2.6: Velocity (colors) and isopycnal surfaces (black curves) over a 3-day subset of the timeseries. (a) Zonal and (b) meridional velocity component anomalies relative to (c) the 3-day temporal mean from mooring T5. (d), (e) and (f) show the same for mooring M5. The horizontal dashed lines indicate the bottom depth at mooring M5, which is on the crest of a bathymetric corrugation. Note velocity (both varying and temporally averaged) are topographically constrained within the corrugation trough (i.e. below the dashed line at mooring T5). For the time-mean velocity, that effect extends upwards for another ≈150 meters.

2.3.2 Overview of the observations

General features of the semidiurnal internal tide, such as bottom-enhanced energy, are highlighted by a 3-day subset of the 50-day mooring records (Fig. 2.6). Velocity and isopycnal displacements are enhanced over the bottom ~300 meters and have amplitude maxima of > 0.1 m s^{-1} and ~ 75 m, respectively. These amplitudes are characteristic of the observed spring tides, four of which have been captured in the full 50-day mooring records (Fig. 2.8a-c). At neap tides, both semidiurnal velocity and displacements drop to about 0.05 m s^{-1} and 30 m, respectively.

From the full mooring records, near-bottom velocity spectra have statistically significant

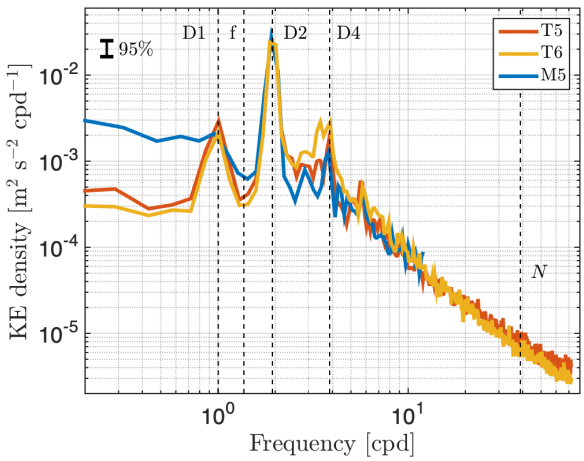

Figure 2.7: Average kinetic energy spectral estimates within 100 meters from the bottom at each mooring on the slope (M5, T5 and T6). Power densities correspond to the sum of negative and positive frequencies from rotary spectra. The 95% confidence interval is indicated in the upper left. Vertical dashed lines are plotted at the diurnal (D_1), inertial (f), semidiurnal (D_2), second semidiurnal harmonic (D_4) and buoyancy (N) frequencies.

peaks at the diurnal, semidiurnal and two times the semidiurnal frequencies (Fig. 2.7). The beating between the diurnal and semidiurnal tides can be seen as diurnal inequalities of isopycnal displacements (e.g. around yearday 48 in Fig. 2.8a,b). Mooring M5, which was deployed on a crest of the corrugated bathymetry, shows larger near-bottom subtidal variability than currents inside the trough of the corrugation.

The diurnal internal tide, which is subinertial and thus coastally trapped at the latitude of our observations, has vertical isopycnal displacements of up to 50 metes (Fig. 2.8d), which are comparable to the semidiurnal variability (Fig. 2.8c). The background cross-slope velocity within the trough of the corrugated bathymetry (below ≈1100 meters at the site of the T5 mooring) is consistently upslope (Fig. 2.8e).

2.3.3 Observed interference pattern

We now describe the observed semidiurnal energy density and flux and how it compares with the patterns in the modeled interference pattern. While our sparse measurements preclude a quantitative decomposition of each wave in the interference pattern, some of the features in the

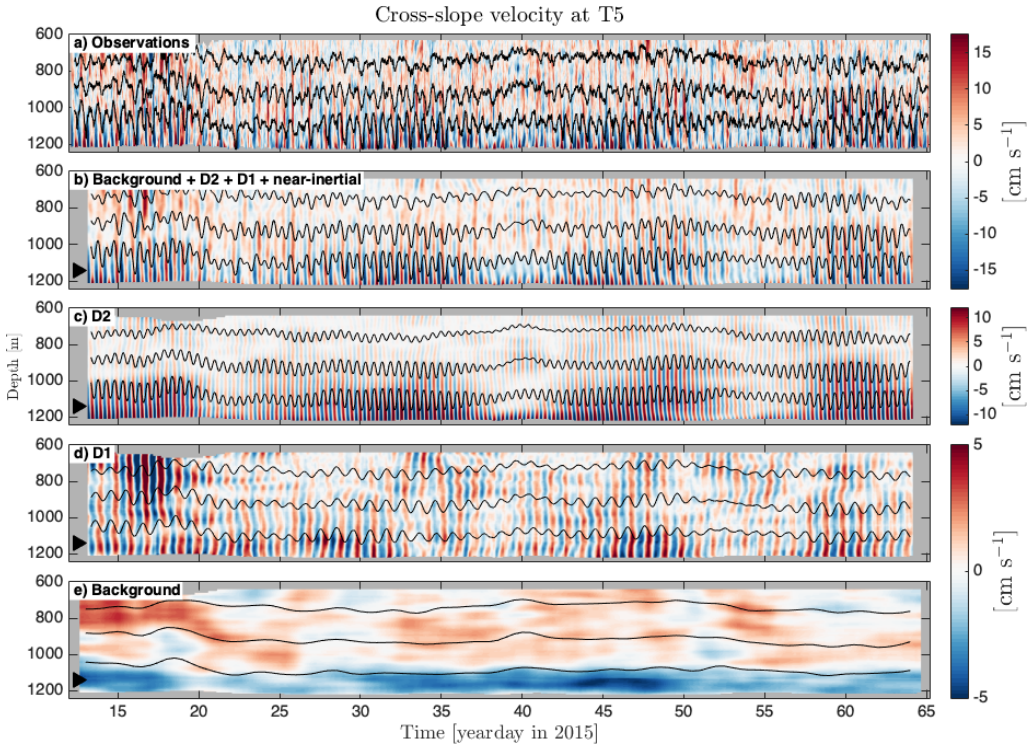

Figure 2.8: Zonal velocity (colors) and isopycnal surfaces (black curves) observed from mooring T5. (a) Observed, (b) sum of filtered signals, (c) semidiurnal (d) diurnal and (e) subinertial (background). Near-inertial is calculated, but not shown because it is small relative to diurnal. The triangle on the bottom-left corner of (b)-(e) indicates the depth of the corrugation crest. Background velocities within the corrugation trough indicate persistent onslope flow and thus upwelling near the sloping bottom. Semidiurnal observations highlight the spring-neap cycle as well the larger velocity and isopycnal displacement in the bottom few hundred meters.

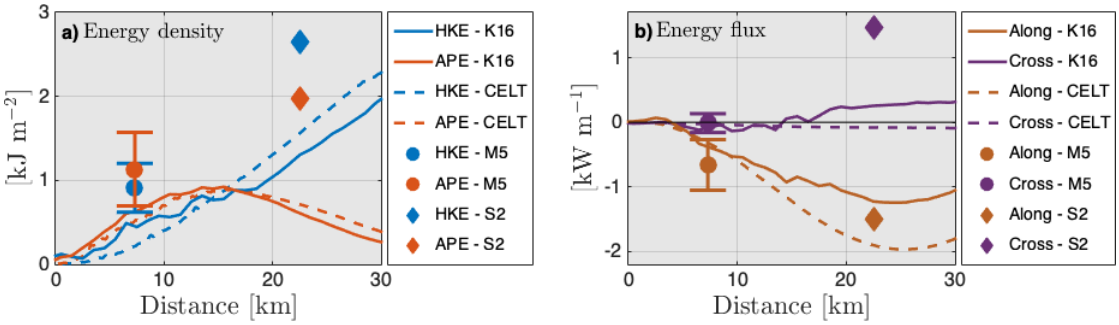

Figure 2.9: Modeled (lines) and observed (symbols) cross-slope structure of depth-integrated semidiurnal energy density (a) and flux (b). For the mooring (M5), averages of the semidiurnally bandpassed energetics are calculated over the full record and are shown along with plus and minus one standard deviation. Diamonds denote estimates from CTD/LADCP station (S2). Qualitative agreement between the cross-slope structure in the models and observations indicate the high reflectivity of the southeastern Tasman slope.

observations are qualitative consistent with the models and thus suggest the large reflectivity of the continental slope. Models and observations also have their limitations and we will highlight differences between their results.

The cross-slope variability in depth-integrated energy density and flux is roughly consistent with the modeled predictions (Fig 2.9). Both the model and mooring show that $HKE/APE \leq 1$ at the same location while HKE is larger than APE near the CTD/LADCP station. Moreover, the along-slope energy flux is poleward and its magnitude increases from the shelfbreak to the deep ocean. Since these features in energy density and flux are consistent with a standing wave pattern, the energetics observed at the two sites across the slope are suggestive of the large reflectivity of the continental slope. While the offshore cross-slope flux at the station is not a feature of the standing wave, it has the same direction as in K16, which indicates the variability of the internal tide in the along-slope direction.

Furthermore, models and mooring observations show bottom-enhanced energetics (Fig. 2.10). Observed energy density (Fig. 2.10a-b) and along-slope flux (Fig. 2.10e) are larger in the bottom few hundred meters, which is the depth range that mostly contributes to the temporal variability in the correspondent depth-integrated quantities (Fig. 2.10c, f). While large values

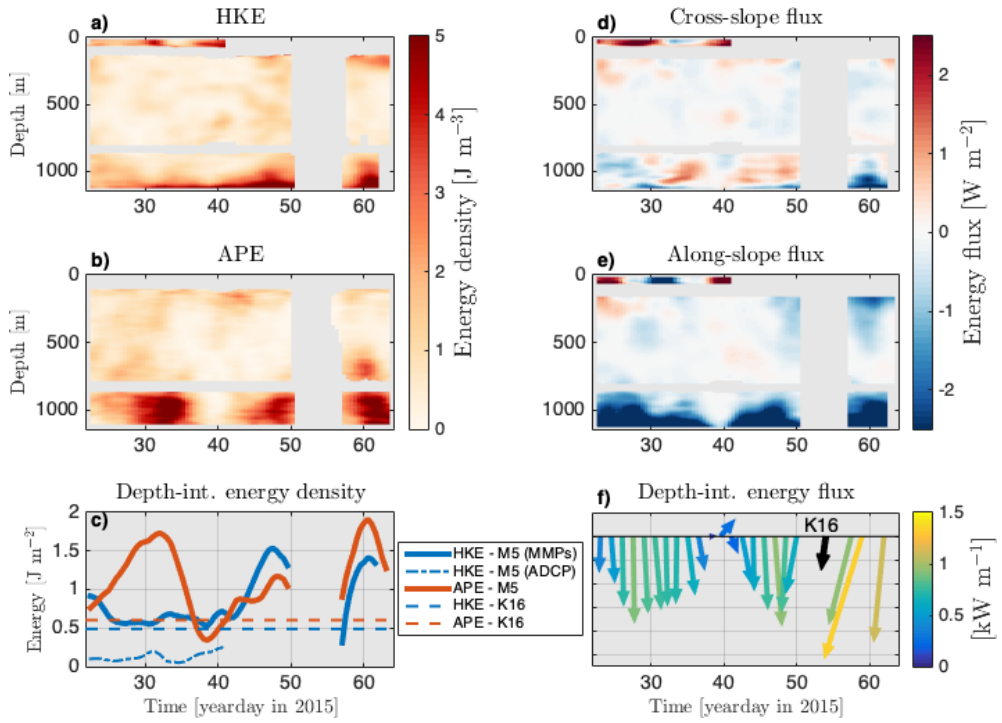

Figure 2.10: Semidiurnal internal tide energy (a, b, c) and flux (d, e, f) from the nearly full water column mooring (M5). Depth-integrated HKE (c) is shown for different instruments because the near-surface ADCP stopped working after yearday 42. Despite large near-surface semidiurnal velocities, HKE from the ADCP is smaller because it covers a relatively small depth range. Energy (dashed lines in (c)) and flux (black arrow in (f)) from the model are shown for comparison. Strong currents between yeardays 49 and 57 prevent the vertical motion of the McLane profilers. Bottom-enhanced energetics, $APE > HKE$ and primarily southward flux on yeardays 32 and 60 are qualitatively consistent with the standing wave interference pattern (Fig. 2.4).

are also found near the surface, which is poorly covered by our observations, they have shorter vertical extent than the near-bottom energetics. These quantitative statements are only true for the three bottom-enhanced periods observed at M5, which are associated with the spring tides previously noted from mooring T5 (Fig. 2.8).

The predominantly along-slope direction in the moored energy flux (Fig. 2.10e, f) further corroborates the standing wave pattern predicted from the models. Since the pressure perturbation is estimated by vertically integrating isopycnal displacement, the along-slope energy flux can also be identified in the phase difference between the near-bottom velocity components and isopycnal displacements (Fig. 2.11). If the internal tide shoaled on the continental slope, near-bottom

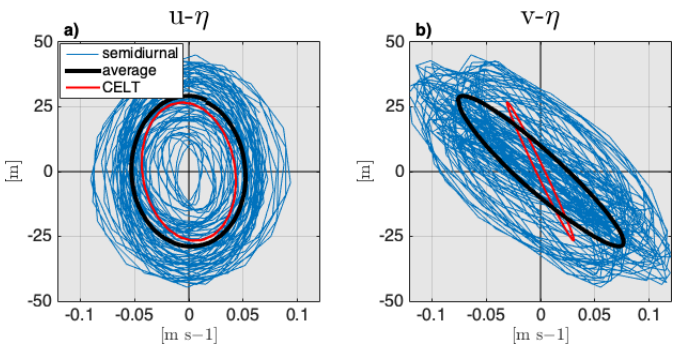

Figure 2.11: Hodographs from observed and modeled semidiurnal cross-slope velocity (u), along-slope velocity v, and vertical isopycnal displacement (η). Velocity and displacement are averaged in the bottom 100 meters. Observations are taken from mooring M5 (blue ellipses) and modeled results from CELT (red ellipses). Mean hodographs for the observations are calculated from the phase-averaged semidiurnal velocity and displacement (black ellipses). Because the pressure perturbation is estimated from vertical integration of η, these two quantities are proportional to one another. Therefore, the non-polarized u-η ellipses (a) indicate small cross-slope energy flux and the predominant along-slope energy flux is shown by largely polarized v-η ellipses (b).

cross-slope velocity and isopycnal displacement would be anti-correlated, such that the energy flux would be onslope. However, model and observations show it is the along-slope velocity component that is anti-correlated with displacement (i.e. ellipses in Fig. 2.11b are polarized with negative slope) and the energy flux at the mooring site has a predominantly along-slope component. Therefore, the observed energy flux supports the high reflectivity of the continental slope because the net cross-slope energy flux is much smaller than the along-slope component, in agreement with the model results that we described earlier (Figs. 2.4 and 2.5).

Several features are also different between models and observations. The magnitudes of energy density and flux are not consistent with the model because the modeled energy density is similar to the observed minimum (Figs. 2.9a and 2.10c) while the average observed flux is close to the model prediction (Figs. 2.9b and 2.10f). Moreover, the partition between HKE and APE varies in time and only the third spring tide (around yearday 60, Fig. 2.10c) appears to be consistent with the model (see also Fig. 2.14d). Furthermore, our description of the cross-slope structure is also crude because the station data at S2 only provides a snapshot in time and we

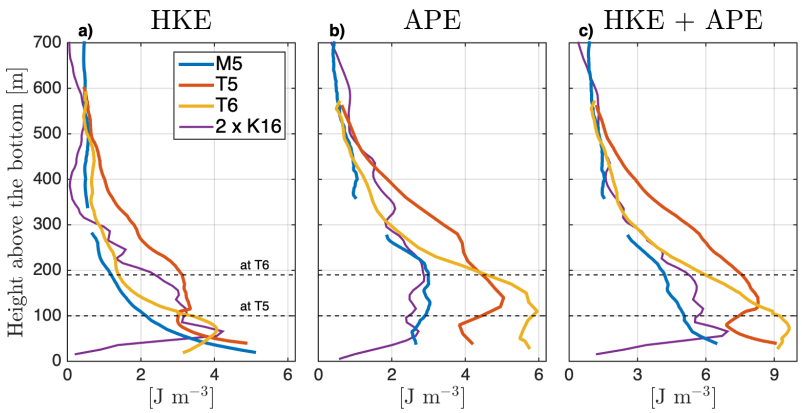

Figure 2.12: Vertical structure of energy density in the bottom-half of the water column: (a) Horizontal kinetic energy (HKE); (b) available potential energy (APE); (c) and their sum. Each profile is a temporal average over the whole record of the semidiurnally bandpassed HKE and APE. Since the model has relatively weak forcing, the modeled profile (K16) is shown with twice its amplitude for quantitative comparison with the observations. For the locations of moorings T5 and T6, the horizontal dashed lines indicate the heights of the corrugation crests above the bottom depth at the adjacent trough. While the broad standing wave structure (K16) explains bottom-enhanced energy over the bottom 300-400 meters, larger energy density is observed along the corrugation trough (T5 and T6) relative to the crest (M5).

only have observations at two locations across the continental slope (the other moorings are close to M5 and differences among them are not due to the large-scale structure of the interference pattern).

2.3.4 Bathymetric corrugations: spatial variability over small scales

Similar to the vertical structure from the M5 mooring, all (full-record) temporally averaged semidiurnal energy profiles are enhanced in the bottom few hundred meters (Fig. 2.12). From all moorings, the vertical scale of enhanced APE is longer than for HKE. These different length scales are qualitatively consistent with CELT (Fig. 2.4e, f), suggesting this feature is simply due to the broad standing wave structure at this location of the slope. Vertical profiles of modeled energy density (K16 in Fig. 2.12) are broadly consistent with observations. Consistent with the relatively weak forcing in the model, modeled energy density is about half of the observed.

Despite the proximity of the three moorings, energy density is larger along the trough of

the corrugation (moorings T5 and T6) as opposed to the crest (mooring M5, Fig. 2.12). Enhanced total energy along the trough is primarily associated with the increase in APE (Fig. 2.12b). The different quantitative responses of HKE and APE to the corrugations may be associated with wave interference leading to different spatial structures for each quantity.

Although we have not investigated how corrugations modulate the energetics, one hypothesis is that high wavenumber waves are generated by topographic scattering [Legg, 2004, Thorpe, 2001] and contribute to the interference pattern at small spatial scales. Larger HKE on the trough (T5) than on the crest (M5) for heights above the rim of the corrugation might be evidence for internal tide scattering (Fig. 2.12a).

For this paper, the modulation of tidal energy by the corrugations is relevant because it creates substantial spatial variability at small horizontal scales. As a result, this leads to uncertainties on how to compare energy magnitudes between moorings as well as between observations and model. For consistency, in the remainder of this paper we restrict the vertical range of depth integration between 40 and 550 meters above the bottom (for mooring M5, energy density is linearly interpolated between MMPs). Within this range, depth-integrated energy is higher from moorings deployed in the corrugation trough (T5 and T6) as opposed to the crest (M5).

2.3.5 Internal tide energy: time mean and variability

The stationary tidal signal contributes most to the mean (≥80%) and variance ($\mathrm{SS}_{E_{\mathrm{M_2S_2}}} \geq 0.6$) of the observed energy (Table 2.2). As expected, the amplitude of the M_2 tide is much larger than that of the S_2 (85% of the stationary mean, not shown). The large stationary fraction of the temporally averaged energy density is in qualitative agreement with concurrent offshore observations [Waterhouse et al., 2018] and model estimates [Savage et al., 2020].

The vertical profile of bandpassed and stationary velocity components (Fig. 2.13) illustrates the validity and caveats of our stationarity metrics (Table 2.2). Towards the bottom, where HKE

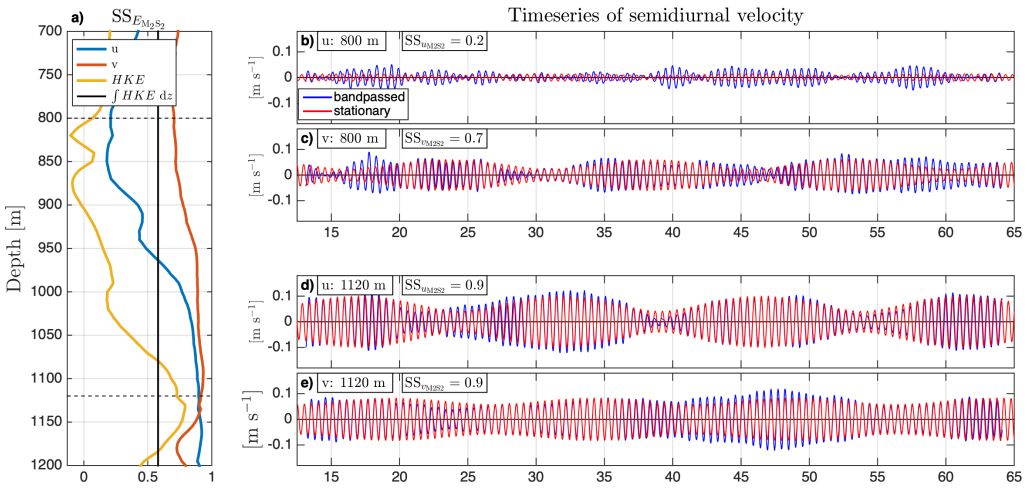

Figure 2.13: Variance of semidiurnally bandpassed velocity and HKE explained by the correspondent stationary signals from mooring T5. (a) Vertical profiles of the skill score, defined by (2.4), for the cross-slope (u) velocity component, the along-slope (v) component, and HKE. The vertical black line is the skill score computed from the depth-integrated HKE. (b), (c) Timeseries of each velocity component farther away from the bottom. (d), (e) same as (b) and (c) but closer to the bottom. The depth of the timeseries and the skill score in (b)-(e) is shown on the top left of the corresponding panels. The larger variability towards the bottom is generally more stationary than higher above.

is elevated, semidiurnally bandpassed u and v amplitude and phase are well-predicted by the harmonic fits to the M_2 and S_2 frequencies, such that there is large skill score between the corresponding signals ($SS_{u_{M_2S_2}} \approx 0.9$ and $SS_{v_{M_2S_2}} > 0.7$). Higher up in the water column, tidal velocities have smaller magnitude and the stationarity also decreases. In terms of the kinetic energy, the stationary metric is generally smaller than for each velocity component separately. However, because HKE is enhanced towards the bottom, the variance explained calculated from the depth-integrated kinetic energy is similar to the high values closer to the bottom.

The vertical profile shows additional features that are not addressed by the stationary depth-integrated energy. For example, the stationary component may be significant for only one velocity component at a single depth (Fig. 2.13b, c) or the spring-neap cycle may differ for each velocity component (Fig. 2.13d, f). Moreover, the relatively high amplitude and stationarity of the along-slope tidal velocity further away from the bottom is likely associated with the surface tide.

For depth-integrated energy density, the large stationary signal (M_2 and S_2) is apparent

Table 2.2: Depth-integrated internal tide energy statistics. Time mean values and standard deviations (inside parenthesis) are in kJ m^{-2}. Depth integrals for the three moorings are taken between 40 and 550 meters above the bottom. The skill score (SS) is defined by (2.4). The numerical model (K16) only has M_2 forcing and no temporal variability in tidal energy.

	Stationary (M_2 + S_2)			Bandpassed (D_2)			SS		
	HKE	APE	E	HKE	APE	E	HKE	APE	E
M5	0.4 (0.1)	0.8 (0.3)	1.2 (0.3)	0.5 (0.2)	0.9 (0.5)	1.5 (0.6)	0.14	0.56	0.58
T5	0.9 (0.2)	1.4 (0.6)	2.3 (0.7)	1.0 (0.3)	1.6 (0.7)	2.6 (0.9)	0.53	0.80	0.81
T6	0.6 (0.1)	1.3 (0.5)	1.9 (0.7)	0.7 (0.2)	1.5 (0.7)	2.2 (0.9)	0.58	0.75	0.78
K16	0.4	0.5	0.9	–	–	–	–	–	–

as the spring-neap cycle in the temporal variability (Fig. 2.14). HKE has a lower stationarity and spring-neap cycle amplitude than APE. However, due to the spatial variability of the partition between kinetic and potential energy in an interference pattern, variability in total energy is likely a more adequate measure of stationarity. Though the nonstationary variability does have a non-negligible contribution, our observations are not sufficient to explain the underlying mechanisms at any specific time (e.g. a relatively more energetic neap tide around yearday 25, Fig. 2.14a).

Though we previously showed the consistency between the observed and modeled average HKE to APE ratio (Fig. 2.9), the temporal variability of this ratio is not consistent with a standing wave at all times (Fig. 2.14d). In particular, HKE has a smaller spring-neap cycle amplitude than APE, and their ratio tends to be lower at spring tides (Figs. 2.14). This pattern suggests that when the incident (and reflected) internal tides have larger amplitude, the standing wave predicted from the models (Fig 2.4) is a better approximation to the total interference pattern. In contrast, the surface tide or locally generated internal tides may a have a significant amplitude when the remote forcing is weak at neap tides.

However, this interpretation is not strictly valid because energy density and flux are nonlinear quantities. That is, because the observed energy depends on the relative phasing between all waves in the interference pattern, including locally generated waves, the time of

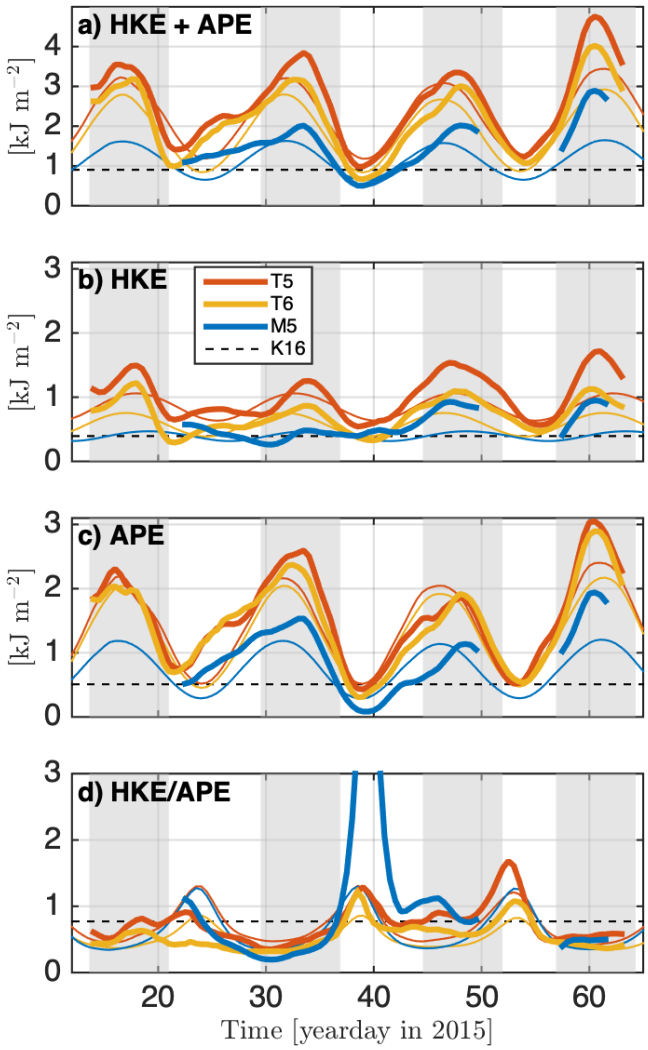

Figure 2.14: Temporal variability of the depth-integrated semidiurnal energy on the southern Tasman slope. Depth integrals are taken over the common height-above-the-bottom range of the observations (40 to 550 meters from the bottom). (a) Total energy, (b) Horizontal kinetic energy (HKE), (c) Available potential energy (APE) and (d) ratio between the curves in (b) and (c). Thin colored lines are depth-integrated stationary energy timeseries. Black dashed lines are the correspondent values from K16. The gray shading indicates the spring tides, centered around the peaks in total energy. The apparent spring-neap cycle (a) indicates large stationarity (i.e. from the beating beating M_2 and S_2 tides). In contrast to K16 (as well as the simple standing wave models in Fig. 2.4), large HKE/APE from the moorings is predominantly observed at neap tides (as well as at the third spring tide). Presumably, the standing wave prediction when the incident wave has a smaller energy flux (neap tides) and the local tides have a relatively larger contribution to the full interference pattern.

maximum incoming flux does not necessarily coincide with maximum observed energy density on the slope.

This nonlinear effect is highlighted by the mismatch between observed and predicted spring-neap cycles (Fig. 2.15). Based on the group velocity, calculated from climatological stratification, the remote internal tide reaches the southern Tasman slope in 9.23±0.06 days (mean and standard deviation based on different ray path choices, Appendix A). This is smaller than the average 12 day-estimate from observed energy, which also differs from the fortnightly cycle of the surface tide by 2 days. Therefore, the phase of the observed spring-neap cycle can not be explained by individually considering the remote internal tide nor the surface tide.

In contrast to these data, offshore observations by [Waterhouse et al., 2018] are in agreement with the predicted travel time from Macquarie Ridge (Fig. 2.15). This difference between datasets suggests that there should be an effect local to the Tasman slope that changes the phasing of the spring-neap cycle there, but not offshore.

2.3.6 Interference of remote and local waves

We attribute the unexpected phase of the observed fortnightly cycle to the complex of interference of remote and local tides. Consider the four-wave interference

$$y(x,t) = \cos\left(k_{M_2}x - \omega_{M_2}t\right) + \cos\left(k_{S_2}x - \omega_{S_2}t\right) + \cos(-\omega_{M_2}t) + \cos(-\omega_{S_2}t), \qquad (2.5)$$

where ω_{M_2} (ω_{S_2}) is the frequency of the lunar (solar) semidiurnal tide, k_{M_2} (k_{S_2}) is the correspondent horizontal wavenumber and x is the distance the remote waves propagate (from $x = 0$). The first (last) two terms on the right-hand side represent the remote (local) M_2 and S_2 internal tides. This four-wave model is a valid representation of tides at a reflective boundary because the reflected wave is phase-locked to the incident internal tide, such that they can both be represented by the remote wave terms in (2.5). Moreover, additional constant phase factors could be included for

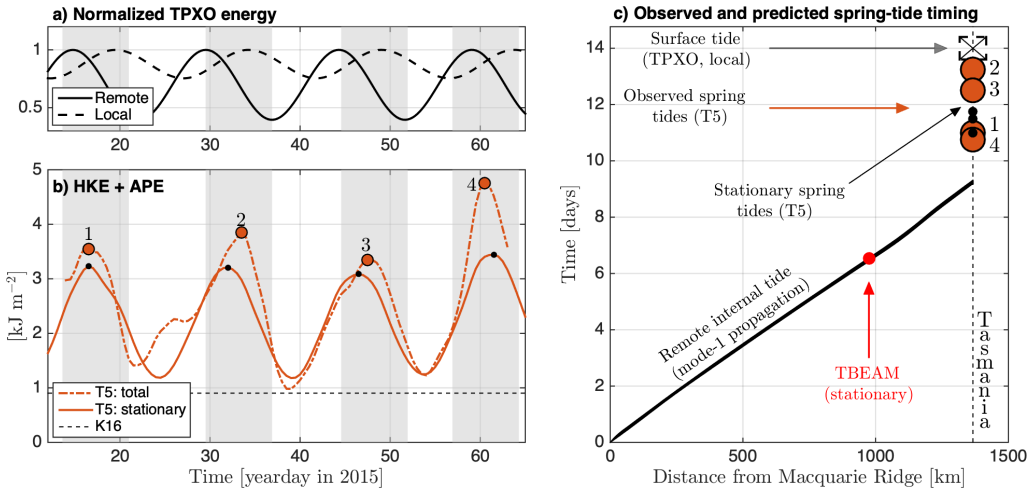

Figure 2.15: Predicted and observed semidiurnal spring-neap cycle. (a) Semidiurnal normalized barotropic tidal energy from TPXO. Local (dashed) refers to the Tasman slope and remote (solid) is the prediction at Macquarie Ridge lagged by the travel time based on the mode-1 group speed in the Tasman Sea (i.e. 9.24 days the value of black line in (c) at the distance corresponding to Tasmania); (b) Total (dot-dashed) and stationary (solid) depth-integrated internal-tide energy from mooring T5 (other moorings are not shown for clarity); (c) distance-time diagram with predicted and observed timing of semidiurnal spring tides taken from (a) and (b), as well as TBEAM data [Waterhouse et al., 2018]. The stationary energy in (b) is not exactly periodic due to temporal variability in the buoyancy frequency. Horizontal dashed lines in (b) is the depth-integrated from the regional numerical model (K16). Gray shading is the same as in Fig 2.14. Time on the y axis is equivalent to fortnight phase, where 0 day is the time of the surface tide spring tide at Macquarie Ridge (i.e., the generation site of the remote internal tide) and the period is ≈14.77 days. Solid black curves (indistinguishable from one another) are theoretical predictions from mode-1 propagation along a set of rays paths (see Appendix B). The mode-1 propagation correctly predicts the phase of the stationary spring-neap cycle in the deep ocean (TBEAM), but it does not explain the timing on the southeastern Tasman slope (T5) and neither does the surface tide (TPXO).

a more realistic analogy with tides in the Tasman sea, but they do not qualitatively change the results and are set to zero for simplicity.

By adding lunar and solar tides together[3], we can rewrite (2.5) as

$$y(x,t) = 2\left[\cos\left(kx-\omega t\right)\cos\left(\delta kx-\delta\omega t\right)+\cos\left(\omega t\right)\cos\left(\delta\omega t\right)\right], \tag{2.6}$$

where $\omega = (\omega_{S2}+\omega_{M2})/2$ and $\delta\omega = (\omega_{S2}-\omega_{M2})/2$ (with analogous definitions for k and δk). While each term on the right-hand side of (2.6) is separable in terms of a carrier wave (with arguments ω and k) and an envelope (with arguments $\delta\omega$ and δk), this is not the case for the full four-wave interference.

The form of the envelope can be calculated from the energy-like quantity $\langle y^2\rangle(x,t)$, where the angle brackets denote time-averaging over a tidal period[4]. Squaring and averaging (2.6) (see Appendix B) gives

$$\tfrac{1}{2}\langle y^2\rangle(x,t) = 1+\cos(\delta kx)\cos(kx)+\cos(\delta kx-2\delta\omega t)\left[\cos(\delta kx)+\cos(kx)\right]. \tag{2.7}$$

It is relevant to see the behavior of (2.7) for $x = \pi/(2\delta k)\pm 2\pi/k$. This location corresponds to half the wavelength of the remote wave envelope. Since $\delta k/k \ll 1$, we can make the approximation $\cos(\delta kx)\approx\cos(\pi/2) = 0$. Under this approximation, (2.7) becomes

$$\tfrac{1}{2}\langle y^2\rangle(x,t)\approx 1+\sin(2\delta\omega t)\cos(kx). \tag{2.8}$$

From (2.8), the spring-neap cycle at distances where $\cos(kx) > 0$ is out of phase relative to what is observed at locations with $\cos(kx) < 0$. Qualitatively, this phase inversion happens because the total spring-neap cycle has an intermediate phase between the individual spring-neap

[3] with the trigonometric identity $\cos(a)+\cos(b) = 2\cos\left(\frac{a+b}{2}\right)\cos\left(\frac{a-b}{2}\right)$

[4] Much of the complexity in the spring-neap cycle with remote and local tides stems from averaging in time only. While an averaging operation in both time and space could be defined, it is not the relevant calculation to interpret point-wise observations.

cycles from local and remote tides, which are themselves out of phase around $x = \pi/(2\delta k)$. Since the solutions are periodic, there are two intermediate phases for the total spring-neap cycle. For a given distance x, the sign of $\cos(kx)$ determines which intermediate phase is the correct one.

While (2.8) provides some insight on the complex interference, we calculate the phase of the envelope numerically to address the superposition of waves with different amplitudes. As opposed to (2.5), the amplitude of the M_2 tide in the ocean is usually much larger than the S_2. As for the relative contribution of remote and local tides on the Tasman slope, the agreement of standing-wave predictions with our mooring observations, as well as with previous glider surveys [Boettger et al., 2015, Johnston et al., 2015], indicates the remote wave is more energetic.

Numerical calculations of the fortnightly phase with fixed ratio between M_2 and S_2 amplitudes and varying local wave magnitude (see Appendix C for details), show that, even with modest local waves, the spring-neap phase is sensitive to the travel time, especially for widths that are consistent the Tasman sea (Fig. 2.16). The larger sensitivity for these widths is reminiscent of the behavior of (2.7) at $x = \pi/(2\delta k)$, which for the Tasman sea is approximately 1125 km. However, the different amplitudes between remote and local waves allow for phases of the envelope in between the two values predicted by (2.8).

The sensitivity of the spring-neap cycle implies that small errors in estimating the distance (or travel time) of propagation by the remote wave may result in large errors in determining the phase of the spring-neap cycle. For example, if the remote wave amplitude is two times the local one (corresponding to a factor of 4 in energy), an error of 5% leads to estimates of the spring-neap phase that range by an equivalent time of 4 days. In terms of the travel time, a 5% error of $\approx$9 days corresponds to $\approx$12 hours.

While the error bound based on different choices of ray paths is only about $\pm$1.5 hours (Appendix A), there are a several other potential sources of error (both uncertainties and biases). For example, the group velocity can change in relatively small temporal and spatial scales due to the background currents and stratification (e.g. [Duda et al., 2018]) or basin-wide over longer

time scales as a result of climate variability [Zhao, 2016].

The four-wave interference provides a mechanism that qualitatively explains the observations of the spring-neap cycle (Fig. 2.15c). On the continental slope, the interference of both local and remote tides is significant such that the timing of observed spring tides is in between the predictions. Moreover, changes in the travel time of a few hours between different spring tides can account for the variability of a few days in their timing. We also highlight this result does not change whether or not TPXO surface tide velocities are subtracted from the data, suggesting the observations are the result from the interference between locally generated internal tides and the remote internal tide. In contrast to the continental slope, the four-wave interference does not apply at the TBEAM site because the magnitude of the northwestward propagating internal tide is much larger than other waves (as shown from satellite altimetry, [Zhao et al., 2018]), and a simple travel time prediction agrees with the in-situ observations [Waterhouse et al., 2018].

2.4 Incident energy flux on the Tasman slope

Because of the complex interference pattern, we can not calculate the incident energy flux from the observed total energy (i.e. through the internal-wave polarization relations). Nevertheless, we can make a rough estimate of the incoming energy flux by scaling the energy density in the model relative to the observations.

The observed average energy density is 2.1 kJ m^{-2}, which is a factor of 2.3 larger than the modeled energy at the mooring sites (Table 2.2). Since the model has a prescribed forcing, with a corresponding energy flux of 1.7 kW m^{-1}, we infer the average incident energy flux on southeastern Tasmania is 3.9 kW m^{-1}. Based on a standard deviation of 40% in total energy density, primarily associated with the spring-neap cycle, we infer an incident energy flux range between 2.3 and 5.5 kW m^{-1}.

The inferred mean incident energy flux is consistent with a concurrent 3.4 kW m^{-1} mode-1

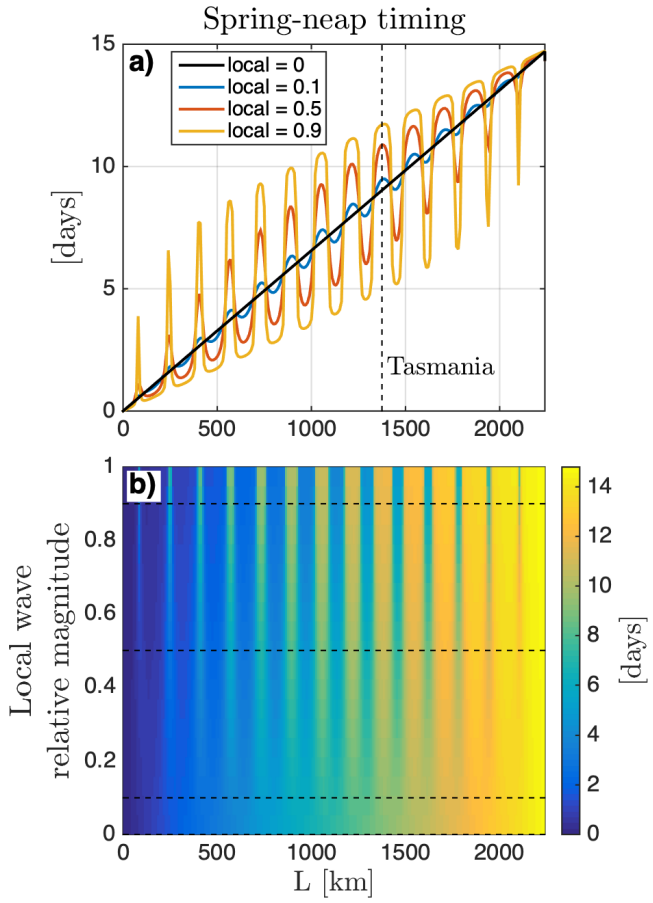

Figure 2.16: Sensitivity of the spring-neap envelope to the local wave amplitude and the propagation distance of the remote wave (L). (a) Spring-neap phase as a function of L for a few local wave amplitudes and (b) the solutions for all local wave amplitudes between 0 and 1. The curves in (a) are the solutions along the horizontal dashed lines in (b). The phase is defined as the time when the envelope peaks (i.e. spring tide). The parameters in the calculation are consistent with the internal tide across the Tasman sea and the Tasman slope corresponds to $L \approx$1400 km.

energy flux based on offshore observations [Waterhouse et al., 2018] and larger than the 2.3 kW m^{-1} from a glider survey [Johnston et al., 2015] undertaken two years before our mooring deployments. Both of these estimates are based on spatially distributed data and have large uncertainties. Since the temporal variability of energy density on the slope is primarily due to the spring-neap cycle, our rough estimate of the incident energy flux range (2.3 to 5.5 kW m^{-1}) primarily corresponds to the stationary (i.e., M_2 and S_2) component.

Nevertheless, the largest energy density observed on the slope seems to be associated with nonstationary variability observed offshore (Fig. 2.17). These energetic events at both locations suggest the remote internal tide experiences nonstationary variability, which leads to a larger incident energy flux on the Tasman slope. Though the anomalously high value on the slope is not as large as would be predicted from [Waterhouse et al., 2018], the time lag between these observations is consistent with the mode-1 travel time. Presumably, the incident energy flux at this time is large enough to overwhelm the temporal lag induced by the interference between remote and local tides. For the rest of the record (i.e., before yearday 55 in Fig. 2.17), this interference can not be neglected and the remote wave travel time alone does not account for the delay between observations on the slope and offshore.

While this analysis shows some consistency between the internal tide observations, there are several caveats that preclude a quantitative comparison. Because of the spatial structure of the offshore internal tide beam, both the mean and variability of the energy flux based on a single mooring are different than their across-beam averaged counterparts (which may explain larger nonstationary variability at TBEAM relative to T5 in Fig 2.17). Moreover, the inferred energy flux by scaling the model to match the observations does not take into account the enhancement of tidal energy along the troughs of the corrugations, which the model does not fully resolve with its 1 km resolution. Finally, the difference between the incident energy flux estimate from [Johnston et al., 2015] and our rough calculation could be due to large uncertainties as opposed to temporal variability of the incident internal tide beam.

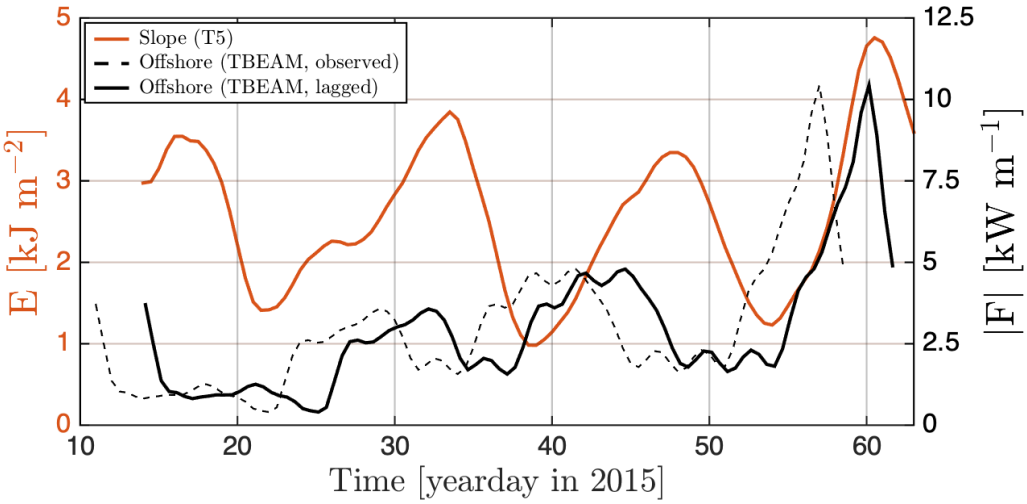

Figure 2.17: Timing of the internal tide energetics observed on the slope (T5) and ≈500 km offshore (TBEAM, [Waterhouse et al., 2018]). Timeseries of depth-integrated energy on the slope (orange line) and magnitude of the mode-1 semidiurnal energy flux (black lines). The solid black line is temporally lagged by the travel time of energy between the TBEAM and T5 sites. As expected from the interference between locally and remotely generated internal tides, the group-velocity-based travel time does not explain the overall timing of energy maxima and minima on the slope. The last peak is an exception, potentially due to a substantially larger incoming energy flux, thus reducing the role of wave interference in setting the timing of spring tides on the slope.

2.5 Summary

Mode-1 internal tides can propagate for hundreds or thousands of kilometers with little dissipation [Ray and Mitchum, 1996, Egbert and Ray, 2000, Zhao et al., 2016, Alford et al., 2019]. Previous work has studied the internal tide beam that is generated south of New Zealand and propagates northwestward for ≈1400 km until impinging on the continental slope of Tasmania. In this paper, we have presented in-situ observations from a region of the slope where previous studies have identified high reflectivity [Johnston et al., 2015, Klymak et al., 2016, Zhao et al., 2018].

As expected, in-situ observations are roughly consistent with modeled standing wave patterns and thus suggest most of the remote internal tide reflects from the continental slope (Figs. 2.4, 2.9, 2.10, and 2.11). While previous work has focused on the standing wave extending hundreds of kilometers away from the boundary [Johnston et al., 2015], we highlight that the bottom-enhanced energetics, over a portion of the continental slope, is part of the standing wave on a sloping bottom. Model analysis indicates that this feature is observed where the rising seafloor on the continental is within the depth range of the deep-ocean mode-1 APE maximum. Even though most of the energy flux from the incident wave is reflected, this region of the continental slope with bottom-enhanced tidal energy may fuel near-bottom turbulence and account for the relatively small fraction of the incident wave that is dissipated on the slope.

In addition to the large-scale standing wave pattern, small-scale bathymetric corrugations lead to spatial variability of tidal energy over horizontal scales of $O(1)$ km. Our observations show larger tidal energy along a trough of the corrugation relative to the adjacent crest (Figs. 2.12 and 2.14). Although we have not investigated which processes are responsible for this pattern, we hypothesize that the more energetic tide along the troughs can lead to larger near-bottom turbulence there as opposed to the crests.

The temporal variability of tidal energy on the continental slope is primarily associated with the stationary spring-neap cycle over the ≈50-day records (Table 2.2 and Fig. 2.14). Although

the TBEAM moored observations do not show a large spring-neap cycle (presumably due to temporal variability of the internal tide over point-wise observations), a large fraction (93%) of the time averaged energy flux is explained by the M_2 internal tide [Waterhouse et al., 2018]. Therefore, our observations indicate that a substantial fraction of the internal tide energy on the slope can be predicted.

The relatively large stationarity ($SS_{E_{M_2S_2}} \geq 0.6$) on the southeastern continental slope of Tasmania is consistent with model estimates [Savage et al., 2017, Savage et al., 2020]. Globally, altimetry-based estimates indicate that stationarity of more than 50% is a common feature of remote internals even far away from their generation sites, as long as they do not propagate near the equator [Zaron, 2017]. In-situ estimates are scarce, but stationarity larger than 0.6 has been observed in the north Pacific, where energetic mode-1 internal tides propagate over $O(1000)$ km from both from Hawaii and Alaska [Zhao et al., 2010].

Despite the large stationarity on the Tasman Sea, anomalously large energetics both on the slope and 500 km offshore suggests that nonstationary variability of the remote internal tide can be non-negligible (Fig. 2.17). The actual processes that create this variability are beyond the scope of this paper, but two potential candidates are wave-mean flow interactions and enhanced internal tide generation due to larger stratification at the generation site.

The observed spring-neap cycle on the slope has an intermediate phase relative to the spring-neap cycles of the remote internal tide and the local surface tide (Fig. 2.15). We show from simple trigonometric calculations that the timing of the spring tide that arises from wave interference is a function of both the relative magnitudes of local and remote tides as well as the travel time of the remote wave (Fig. 2.16). These effects can lead to changes in the timing of the spring tide by a few days, as observed in our mooring records. Although we only present the variability in the timing of the spring tides, our observations reinforce results from [Kelly and Nash, 2010] on the interference between local and remote waves. For example, modeling internal-wave generation on the continental slope of Tasmania, perhaps associated with

the small-scale corrugations, would need to incorporate tidal forcing as the interference between the surface and the remote internal tide.

An important question that we are not able to address from our sparse measurements is the energy flux carried by each separate wave in the full interference pattern. Though scaling the model results based on the observations suggests the mean incident energy flux is about 3.9 kW m^{-1}, more observations would be required to obtain a direct estimate. Nevertheless, analysis of the in-situ observations, along with models of varying degree of realism, allows us to explain certain features of the complex internal tide field on the southeastern Tasman slope: the standing wave captures broad features of the internal tide energetics, but interaction with small-scale topography and interference with locally generated waves also play a significant role.

2.6 Appendix A: Range of travel time estimates

We argued in section 2.32.3.6 that the temporal mismatch of ≈2 days between the observed spring-neap cycle and the predicted from the remote internal tide only is due to interference with the locally generated tide. An alternate hypothesis is that the theoretical estimate of the remote wave travel time that we used (9.25 days) as a temporal lag is physically inadequate. Here we present a range of travel time estimates and show that they can only account for a time mismatch of less than a day and are thus not able to explain the timing of the spring-neap cycle on the slope.

The theoretical group velocity we refer to is that derived from the dispersion relationship for linear internal mode waves. This formulation does not include nonlinear effects nor wave-current interactions. Moreover, one of the parameters is stratification, which can vary in a wide range of spatial and temporal scales. Finally, the travel time is calculated based on a choice of ray path and is thus dependent on the spatial variability of the relevant parameters used to calculate the group velocity.

From altimetry observations and the same theoretical group velocity we use in this paper,

[Zhao et al., 2018] found the observed phase speed from satellite altimetry is at most 5% higher than the theoretical prediction (see their Fig. 8). This implies a shorter travel time by 5%, or 11 hours for energy. As argued by [Zhao et al., 2018], this difference may be attributed to effects not included in linear theory or the different temporal coverages of the data in the altimetry record and climatology. Regardless of the dominant effect, the difference in travel time alone does not explain the ≈2-day lag in Fig. 2.15.

The altimetry-based energy flux of the westward propagating internal tide highlights the geographical locations where ray paths may be taken for appropriate travel time estimates (Fig. 2.18a). We chose several ray paths that end at southeastern Tasmania, but start at different locations along Macquarie Ridge (Fig. 2.18b). An additional ray path was taken following the middle of the internal tide beam and bending westward around the East Tasman Plateau, consistent with refraction by the topography. From the group velocity taken on the ray paths (Fig. 2.18c), we calculated a range of travel time estimates (Fig. 2.18d).

Due to relatively large-scale gradients of the climatological group velocity, the range of travel time estimates is less than 5 hours and different choices of ray paths do not explain the observed timing of the spring-neap cycle on the slope. Even when scaling the climatological group velocity throughout the Tasman sea, such that it matches with the value obtained from moored observations at the TBEAM site, the difference in travel time is only 8 hours.

Given all these travel time estimates, the value of 9.25 days used in Fig. 2.15 may be biased by about half a day at most. Therefore, this range of theoretical estimates is relatively short and can not explain the 2-day lag between theoretical and observed timings of the spring-neap cycle.

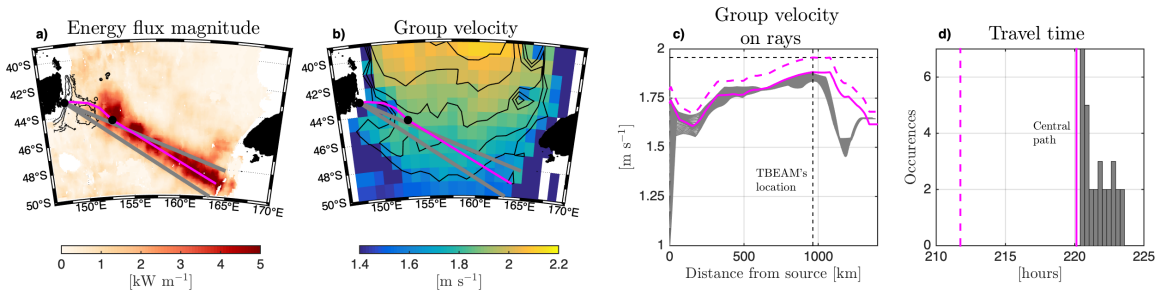

Figure 2.18: Range of travel time estimates for the internal tide energy across the Tasman Sea. (a) Energy flux magnitude of westward propagating waves (based on satellite altimetry, [Zhao et al., 2018]). (b) Theoretical group velocity (c_g) of the mode-1 M_2 internal tide based on climatological stratification. (c) c_g along rays that start at Macquarie Ridge and end in southeastern Tasmania. (d) Histogram of travel time estimates for 30 rays bounded by the gray-shaded rays in (a) and (b). These are the rays used to calculate the travel time of the remote internal tide in Fig. 2.15. The black dots in (a) and (b) indicate mooring locations from TTIDE and TBEAM. The gray rays are arcs along great circles. The solid pink ray was chosen such that it lies along the center of the internal tide beam and bends around the East Tasman Plateau (consistent with refraction). The travel time indicated by the dashed pink line is calculated by first scaling c_g along the solid pink line such that the theoretical group velocity based on a climatology matches with the value (1.97 m s^{-1}) calculated from TBEAM's mooring observations concurrent with TTIDE.

2.7 Appendix B: Four-wave interference with equal amplitudes: analytical calculation

The form of the envelope of the four-wave interference (2.5) is given by the energy-like quantity $\langle y^2 \rangle (x,t)$. Angle brackets denote averaging over a wave period, i.e.

$$\langle y^2 \rangle (x,t) = \frac{\omega}{2\pi} \int_{t-T/2}^{t+T/2} y^2(x,t')\, \mathrm{d}t', \tag{2.9}$$

where ω is the semidiurnal frequency and $T = 2\pi/\omega$ is the equivalent period.

The square of (2.6) is

$$\begin{aligned}\tfrac{1}{4}y^2 = &\underbrace{\cos^2(kx-\omega t)\cos^2(\delta kx-\delta\omega t)}_{I} + \underbrace{\cos^2(\delta\omega t)\cos^2(\omega t)}_{II} + \\ &+ \underbrace{2\cos(kx-\omega t)\cos(\delta kx-\delta\omega t)\cos(\delta\omega t)\cos(\omega t)}_{III}.\end{aligned} \tag{2.10}$$

We now phase-average each term of (2.10). Since $\delta\omega/\omega \ll 1$, terms with frequency $\delta\omega$ are approximately constant over a semidiurnal period. With this approximation, the average of I is

$$\begin{aligned}\langle I\rangle &= \langle\cos^2(kx-\omega t)\cos^2(\delta kx-\delta\omega t)\rangle \\ &\approx \cos^2(\delta kx-\delta\omega t)\underbrace{\langle\cos^2(kx-\omega t)\rangle}_{=1/2} \\ &= \tfrac{1}{2}\cos^2(\delta kx-\delta\omega t).\end{aligned} \tag{2.11}$$

Similarly, the average of II is

$$\langle II\rangle = \tfrac{1}{2}\cos^2(\delta\omega t). \tag{2.12}$$

The average of the third term is

$$\begin{aligned}\langle III\rangle &= 2\cos(\delta\omega t)\cos(\delta kx-\delta\omega t)\langle\cos(kx-\omega t)\cos(\omega t)\rangle \\ &= 2\cos(\delta\omega t)\cos(\delta kx-\delta\omega t)\langle[\cos(kx)\cos(\omega t)+\sin(kx)\sin(\omega t)]\cos(\omega t)\rangle \\ &= 2\cos(\delta\omega t)\cos(\delta kx-\delta\omega t)\left[\cos(kx)\langle\cos^2(\omega t)\rangle + \sin(kx)\underbrace{\langle\sin(\omega t)\cos(\omega t)\rangle}_{=0}\right] \\ &= \cos(kx)\cos(\delta\omega t)\cos(\delta kx-\delta\omega t).\end{aligned} \tag{2.13}$$

Therefore, $\langle y^2\rangle$ is given by

$$\tfrac{1}{4}\langle y^2\rangle(x,t) = \tfrac{1}{2}\cos^2(\delta kx-\delta\omega t) + \tfrac{1}{2}\cos^2(\delta\omega t) + \cos(kx)\cos(\delta\omega t)\cos(\delta kx-\delta\omega t). \tag{2.14}$$

With trigonometric identities, the first two terms on the right-hand side of (2.14) can be rewritten as

$$\begin{aligned}\tfrac{1}{2}\cos^2(\delta kx-\delta\omega t)+\tfrac{1}{2}\cos^2(\delta\omega t) &= \tfrac{1}{2}\left[\tfrac{1}{2}\cos(2\delta kx-2\delta\omega t)+\tfrac{1}{2}\cos(2\delta\omega t)+1\right]\\ &= \tfrac{1}{2}\left[\cos\left(\tfrac{1}{2}(2\delta kx)\right)\cos\left(\tfrac{1}{2}(2\delta kx-4\delta\omega t)\right)+1\right]\\ &= \tfrac{1}{2}\left[\cos(\delta kx)\cos(\delta kx-2\delta\omega t)+1\right]\end{aligned} \tag{2.15}$$

and the last term as

$$\begin{aligned}\cos(kx)\cos(\delta\omega t)\cos(\delta kx-\delta\omega t) &= \tfrac{1}{2}\cos(kx)\left[\cos(\delta\omega t-\delta kx+\delta\omega t)+\cos(\delta\omega t+\delta kx-\delta\omega t)\right]\\ &= \tfrac{1}{2}\cos(kx)\left[\cos(2\delta\omega t-\delta kx)+\cos(\delta kx)\right]\\ &= \tfrac{1}{2}\cos(kx)\left[\cos(\delta kx-2\delta\omega t)+\cos(\delta kx)\right].\end{aligned} \tag{2.16}$$

Substituting (2.15) and (2.16) into (2.14) gives

$$\tfrac{1}{2}\langle y^2\rangle(x,t) = 1+\cos(\delta kx)\cos(kx)+\cos(\delta kx-2\delta\omega t)\left[\cos(\delta kx)+\cos(kx)\right]. \tag{2.17}$$

2.8 Appendix C: Four-wave interference with arbitrary amplitudes: numerical calculations

The spring-neap phase in Fig. 2.16 is calculated from

$$y(t) = A\cos\left(k_{M_2}L-\omega_{M_2}t\right)+B\cos\left(-\omega_{M_2}t\right)+C\cos\left(k_{S_2}L-\omega_{S_2}t\right)+D\cos\left(-\omega_{S_2}t\right), \tag{2.18}$$

which is similar to (2.5), but with arbitrary amplitudes. In the idealized calculation, the remote wave has fixed amplitude and, since the M_2 tide is often much more energetic than the S_2,

we set $A = 0.9$ and $C = 0.1$. For simplicity, we set $B = A$ and $D = C$. The spring neap cycle is calculated for $0 \leq (B + D) < 1$ (i.e. the x axis in Figure 2.16b). Results are also presented for $0 \leq L \leq 2250$ km, where the upper bound is the periodicity of the results (see Fig.2.16a) and $L \approx 1400$ km is analogous to the distance between Macquarie Ridge and Tasmania.

The mode-1 horizontal wavenumbers (k_{M_2} and k_{S_2}) for the respective semidiurnal tidal frequencies are calculated from the dispersion relationship

$$\omega^2 = \left(\frac{NH}{\pi}\right)^2 k^2 + f^2, \tag{2.19}$$

where H is the bottom depth, f the Coriolis parameter and N the buoyancy frequency. Equation (2.19) assumes constant stratification and a rigid lid approximation (e.g. [Wunsch, 1975]). We use parameters appropriate for the Tasman Sea: $N = 2 \times 10^{-3}$ s^{-1} (i.e. the depth-average from climatology [Boyer et al., 2013]), H = 4000 m and $f \approx 1.03 \times 10^{-4}$ s^{-1} (correspondent to a latitude of 45 °N, where the sign is irrelevant). The implied group velocity (i.e., $c_g = \partial\omega/\partial k$) is 1.7 m s^{-1}, which corresponds to the average value across the Tasman Sea along the path of the internal tide.

For a range of values of $(B + D)$ and L, we then calculate $\langle y^2 \rangle(t)$, where the angle brackets denote semidiurnal phase-averaging, and find the time of maximum variance. We define this time as the spring-neap phase.

Note that when local and remote waves have the same magnitude ($A = B$ and $B + D = 1$), there are values of L for which there is perfect cancellation at each frequency and the spring-neap phase is not defined. These are the same distances for which the derivative of spring-neap phase with respect to L is maximum in the case where $B + D < 1$ (Fig. 2.16a).

2.9 Acknowledgements

This study was supported by the National Science Foundation (through Grants OCE-1129246 and OCE- 1129763). AFW and SMK acknowledge funding from NSF- OCE1434722 and NSF-OCE1434352 and ship time aboard the R/V Falkor supported by the Schmidt Ocean Institute. HS and DB were supported by NSF-OCE 1130048. We thank the captain and crew of the R/V Roger Revelle and the engineers of the Scripps MOD group for their hard work and expertise at sea that made this work possible. We are grateful to Gunnar Voet for his generous work in preparing and conducting mooring and shipboard operations.

Chapter 2, in full, is a reprint of the material as it appears in Journal of Physical Oceanography, 2021, DOI: 10.1175/JPO-D-20-0044.1. Olavo B. Marques, Matthew H. Alford, Robert Pinkel, Jennifer A. MacKinnon, Jody M. Klymak, Jonathan D. Nash, Amy F. Waterhouse, Samuel M. Kelly, Harper L. Simmons, and Dmitry Braznikov. The dissertation author was the primary investigator and author of this paper.

Chapter 3

Observations of tidally driven turbulence over steep, small-scale topography on the Tasman slope.

3.1 Introduction

Tides are one of the primary energy sources for diapycnal mixing in the abyssal ocean [Munk and Wunsch, 1998, De Lavergne et al., 2016]. This mixing sustains net upwelling and is an essential component of the lower meridional overturning circulation [Lumpkin and Speer, 2007]. In contrast, the upper meridional overturning circulation can exist largely independent of diapycnal mixing at mid-depths away from high latitudes [Talley, 2013, Cessi, 2019]. Given these differences on how turbulence may or may not play a role in the general circulation, accurate representations of the vertical structure of tidal dissipation are required for realistic general circulation models and have been shown to significantly affect ocean climate simulations [Melet et al., 2013].

Tidal mixing is often separated into local and remote mixing [Whalen et al., 2020]. Surface tide over sloping topography generates internal tides that propagate away as well as a

trapped response that can lead to large turbulence locally [Klymak et al., 2011]. Propagating internal tides with large wavenumber (characteristic of modes higher than 4) are thought to dissipate relatively close ($\leq$ 100 km) to their generation sites such that they also contribute to local mixing in coarse resolution models [de Lavergne et al., 2019, Vic et al., 2019]. Low-mode internal tides can propagate over much longer distances ($\geq$ 1000 km) and induce mixing remotely [Alford, 2003, Zhao et al., 2016, Zhao, 2018]. Each of these processes contribute to different spatial distributions of diapycnal mixing in the ocean and ultimately determine the potential roles of tidal mixing in the ocean [de Lavergne et al., 2020, Whalen et al., 2020].

While direct and indirect estimates of small-scale turbulence are now beginning to characterize the global geography of turbulence [Whalen et al., 2012, Waterhouse et al., 2014, Kunze, 2017], process studies that can identify the responsible processes are more sparse. In particular, observations of tidally driven turbulence have focused on the steep flanks of tall ridges with strong surface tides (e.g. [Levine and Boyd, 2006, Klymak et al., 2006, Pinkel et al., 2012, Alford et al., 2014, Musgrave et al., 2016]). Near-bottom turbulence in these regions is consistent with tidal lee wave theory [Legg and Klymak, 2008, Klymak et al., 2010a]. Observations over smaller-scale or isolated topographic features also highlight the importance of nonlinear tides over steep topography in setting near-bottom tidal dissipation [Dale and Inall, 2015, van Haren, 2017]. Although steep continental slopes reflect the energy of incident low-mode internal tides back to the deep ocean [Nash et al., 2004, Johnston et al., 2015], steep isolated topography embedded on the continental margin can also sustain hotspots of large dissipation [Nash et al., 2007, Klymak et al., 2011]. Nevertheless, since these sparse observations may not be representative of tidally driven turbulence in the deep ocean, it is unclear whether lee-wave like phenomena are responsible for turbulence above abyssal hills, which in turn contributes to most of the tidal energy dissipation in the abyssal ocean (below 2000 m) [de Lavergne et al., 2020].

Furthermore, direct measurements that can identify the processes driving near-bottom, deep-ocean turbulence are challenging and scarce. Where tides are important, spatially re-

solving observations must be taken over time scales sufficiently shorter than a tidal period [Voet et al., 2020]. For example, observations from a towed platform at the Hawaiian Ridge [Alford et al., 2014] resolved breaking tidal lee waves, which had been inferred from the agreement between timeseries [Levine and Boyd, 2006, Klymak et al., 2008] theoretical predictions [Legg and Klymak, 2008, Klymak et al., 2010a]. In contrast, the temporal variability at the steep flanks of a seamount [van Haren, 2017] do not agree with the same theory such that the source of the observed nonlinear tidal flows is unclear. Observations that can constrain the primary processes driving turbulence in the deep ocean, as well as their temporal variability, may indicate avenues for improving parameterizations of small-scale turbulence in large-scale climate models [Whalen et al., 2020].

In this study, we present observations of turbulent processes over small-scale topography near Tasmania (Fig. 3.1). These observations were taken as part of the Tasman Tidal Dissipation Experiment (TTIDE) to study the fate of a remote internal tide impinging the continental slope of Tasmania [Pinkel et al., 2015]. In contrast to other regions [Nash et al., 2004, Martini et al., 2011], Tasmania has a fairly well-defined remote internal tide forcing (Fig. 3.2a). In the steep southeastern slope, the incident wave primarily reflects back to the deep ocean [Johnston et al., 2015, Klymak et al., 2016, Marques et al., 2021]. However, model results show a much lower reflectivity in the northeastern region [Johnston et al., 2015, Klymak et al., 2016]. Numerical modeling [Klymak et al., 2016] showed enhanced dissipation associated with a small-scale bump embedded on the large-scale continental slope (Fig. 3.1a). Motivated by this turbulence hotspot in the model, we used a combination of moored and shipboard measurements to resolve the spatial and temporal variability of wave breaking mechanisms that lead to tidally driven turbulence.

We begin with a description of the region of study and our measurements (section 3.2). We then describe how response of tidal flow over the bump, its spatial variability, and associated turbulence in a numerical simulation (section 3.33.3.1) and in the observations (section 3.33.3.2).

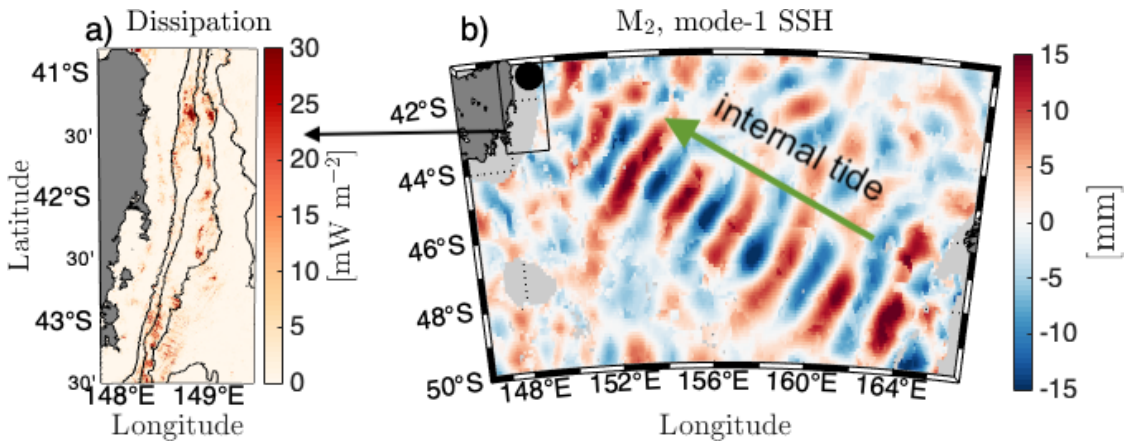

Figure 3.1: Incident internal tide on the Tasman slope and induced dissipation from a numerical model. (a) Depth-integrated dissipation from a numerical model [Klymak et al., 2016] forced by a mode-1 remote internal tide. (b) In-phase M_2, mode-1 sea surface height (SSH) from satellite altimetry [Zhao et al., 2018]. The numerical model predicts hotspots of enhanced dissipation in northeastern Tasmania. The offshore hotspot is associated with a bump on the continental slope. The radiation of an internal-tide beam from the bump leads to the enhanced dissipation further onshore. In this paper, we present observations taken in the vicinity of the bump (see Fig. 3.2).

From our 45-day long timeseries, we show that near-bottom dissipation rate is primarily driven by the tides and both have complex temporal variability (section 3.4). While our measurements can not constrain the large-scale tidal forcing, we present observations that support that the incident remote internal tide plays a significant role (section 3.5). Despite the complexity in the observations, some general features are in good agreement with idealized theory of tidal flow over supercritical topography (section 3.6). We conclude with a summary (section 3.7). For completeness, the supplemental material includes additional figures with the observations not discussed in detail in the paper.

3.2 Methods

3.2.1 Observations

We have made mooring and shipboard observations around a topographic bump on the northeastern continental slope of Tasmania at a depth of about 1900 meters (Fig. 3.2). The bump

is somewhat elongated in the along-slope direction and the bottom slope is primarily aligned in the cross-slope direction. Immediately adjacent to the crest (within 1km), the onshore side has a steeper slope than the offshore side (Fig. 3.2b).

The relevant bottom slope for internal tide dynamics is quantified in terms of the criticality parameter

$$\gamma \equiv \frac{\beta}{s}, \tag{3.1}$$

where β is the bottom slope,

$$s \equiv \sqrt{\frac{\omega^2 - f^2}{N^2 - \omega^2}} \tag{3.2}$$

is the slope of internal-wave characteristics, ω is the frequency of the waves, f is the Coriolis parameter, and N is the buoyancy frequency at the bottom.

As the remote internal tide enters the continental margin, the wave shoals where the bottom slope is subcritical ($\gamma < 1$) (Fig. 3.2b). Near the 3200 m isobath, where the bottom slope first becomes supercritical ($\gamma > 1$) for a significant distance, the shoaling internal tide is expected to undergo significant scattering. In other words, for an incoming mode-1 internal tide, the wave primarily remains as mode-1 over the subcritical region but significant conversion to higher modes takes place where the bottom becomes supercritical. Under this hypothesis of tidal forcing, the tidal flow is blocked over most of the supercritical bottom and a nonlinear lee wave develops near the crest of the topography [Klymak et al., 2010a].

One mooring (T1) was deployed for most of the experiment (≈45 days) on the onshore side of the bump. Velocity was measured from two downward-looking acoustic Doppler current profilers (ADCPs). A higher frequency (300-kHz RDI Workhorse) ADCP covered the bottom 100 meters of the water column, whereas a 75-kHz RDI Longranger measured the overlying 500 meters. Over this vertical range, temperature was measured by 36 thermistors, where the vertical spacing is smallest (10 meters) in the bottom 200 meters. Two SBE-37 MicroCAT CTDs were deployed near the top and bottom of the mooring. An additional mooring (T2) with similar

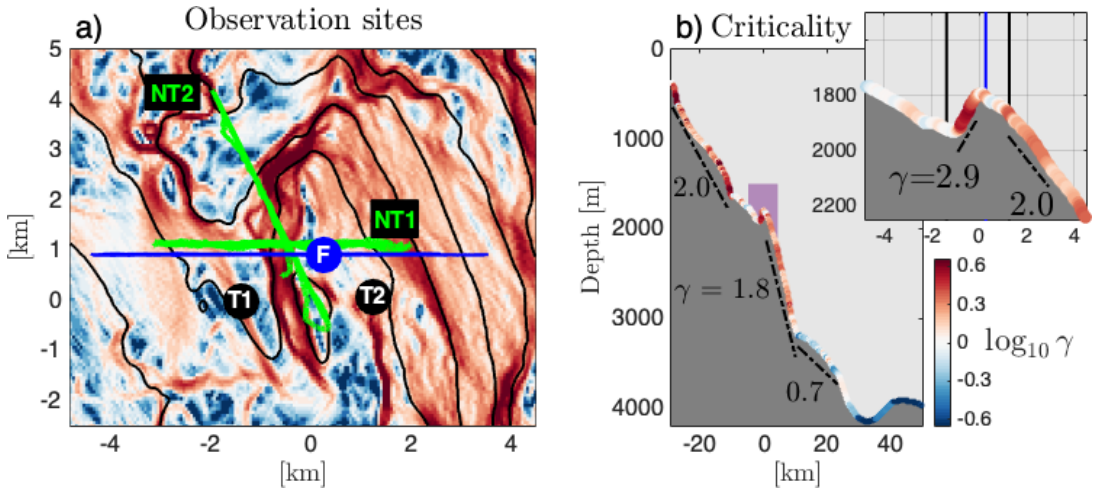

Figure 3.2: Observational dataset around small-scale bump in northeastern Tasmania. (a) Location of the observations around the bump. (b) Cross-slope section of the bathymetry and bottom criticality (γ). Contours in (a) show bathymetry at 100 m depth spacing and color shading is $\log_{10}\gamma$, with the same color limits as in (b). Note that $\log_{10} 0.3 \approx 2$. Average γ is shown for different subsets of the continental slope in (b). Our observations consist of two moorings (T1 and T2), two CTD/LADCP towyos (NT1 and NT2), and a Fast-CTD station (F) and towyo (blue line crossing F). The purple shaded area in (b) is the area of the Fast-CTD transect and the vertical lines in the insert show the locations of the moorings and the Fast-CTD station. Observations are generally restricted to depths below 1400 m.

instrumentation was also deployed for 3.5 days, but on the offshore side of the bump.

Over the common deployment period of T1 and T2, we conducted CTD/LADCP towyos across the bump. One towyo (NT1) was aligned in the cross-slope direction, which is the direction primarily aligned with the bottom slope around the bump. Nevertheless, given the specific shape of topography, we conducted a second towyo (NT2) that is at an angle to the other one. Velocity measurements were made from downward and upward looking 300-kHz RDI Workhorse ADCPs mounted on the CTD rosette.

Additional CTD measurements from a rapid profiling platform (Fast-CTD) were taken several weeks after the CTD/LADCP towyos. The profiling speed for the Fast-CTD was about 2.5 m s^{-1} and the vertical resolution of temperature and salinity is 2 m. We made observations along cross-slope transects across the bump for about two and half days, followed by a 2-day long timeseries taken at the crest of the bump.

Moored timeseries of potential density are obtained from thermistor data and a temperature-salinity (T-S) polynomial fit based on moored and shipboard CTD observations. Deviations from the T-S relation are large only in the upper range of the moorings observations (the top $\approx$150 meters), where temperature inversions can be salinity compensated.

3.2.2 Dissipation rate estimates

For CTD shipboard measurements, we used the Thorpe-scale method [Thorpe, 1977] to estimate the dissipation rate of kinetic energy (ϵ). Briefly, we sorted the vertical profiles of potential density into stable profiles and used the vertical displacement associated with the sorting to identify individual overturns. For each overturn, the Thorpe length scale is defined as the root-mean-square of the vertical displacements and it is assumed to be proportional to the Ozmidov scale, i.e.

$$L_O = \alpha L_T, \tag{3.3}$$

where $L_O \equiv \left(\epsilon/N^3\right)^{1/2}$. An estimate of the dissipation rate can then be obtained by

$$\epsilon = \alpha^2 L_T^2 N^3, \tag{3.4}$$

where we used $\alpha = 0.8$ [Dillon, 1982] (see below our discussion on the caveats of this assumption).

Although the Thorpe-scale method is most often applied to shipboard CTD observations, it has also been used with moored thermistor data [Aucan et al., 2006, Levine and Boyd, 2006, van Haren, 2017]. In our case, thermistors in the bottom 200 meters are spaced by 10 meters and up to 30 meters higher above the bottom. Therefore, the smallest overturns that can be identified in our moorings is a factor of 10 larger than from shipboard measurements and, from (3.4), this factors increases to two orders of magnitude in terms of ϵ. Moreover, the Thorpe scale and the derived ϵ are undefined for observed stable density profiles. To compute averages of Thorpe-scale-based ϵ, these undefined values must be substituted by an ad-hoc background value. Since the mooring observations have lower vertical resolution and higher ϵ noise floor than the shipboard data, the substitution of a background ϵ can impart a larger bias in the statistics of the mooring-based dissipation.

Similar to [Cimatoribus et al., 2014], we have estimated ϵ from the mooring data using the Ellison scale (L_E) instead of the Thorpe scale in (3.4). The Ellison scale is defined as

$$L_E \equiv \frac{\sqrt{\langle T'^2 \rangle}}{\partial \langle T \rangle / \partial z}, \tag{3.5}$$

where $\langle T'^2 \rangle$ is the turbulent temperature variance and $\partial \langle T \rangle / \partial z$ is the vertical gradient of the background temperature profile. In practice, we used an 1-minute window for the averaging operation (where the temperature sensors have a sampling frequency of 2 Hz and a response time of about 10 seconds). For the vertical gradient, we sorted the temperature profile into a stable one, such that L_E is always positive. Since the mooring has fast time sampling (relative to shipboard observations) and (3.4) is based on an ensemble-averaged length scale [Thorpe, 1977],

we further averaged L_E over 10-minute intervals before calculating ϵ. We also assumed $\alpha = 0.8$ for the calculation with the Ellison scale.

The dissipation rate estimates based on the Ellison scale are consistent with those based on the Thorpe scale and are less affected by environmental and sampling constraints that lead to biases in L_T (Figs. 3.3). Temperature inversions around 1500 meters, which shipboard measurements show are salinity-compensated, contaminate the Thorpe-based ϵ, but not the one based on the Ellison scale. Moreover, the Thorpe scale is more sensitive than the Ellison scale around the depth level where the thermistor spacing changes, such that ϵ from L_T decrease upwards more abruptly than ϵ from L_E. Even within the region near the bottom with the shortest thermistor spacing, overturns on the order of meters (not captured by our instruments) can significantly contribute to turbulent events (i.e. around yearday 39.75 in Fig 3.3).

Dissipation rates from the two vertical scales are quantitatively consistent with one another (Fig. 3.4). Semidiurnal, depth-averages of ϵ from the two methods are correlated with one another. Averages from the Thorpe-scale based ϵ were calculated by assuming a background dissipation of 10^{-9} m^2 s^3. The capability of observing smaller ϵ with the Ellison scale is consistent with both the relatively larger ϵ estimates from L_E and the slope of the regression with the estimate from L_T. Only the Ellison scale can account for overturns on the order of meters and their dissipation rate is larger than the ad-hoc background value, thus resulting in larger averages of ϵ. However, this difference between methods is more significant for turbulent events with smaller dissipation, which results in a regression slope smaller than the one-to-one relationship (Fig. 3.4).

We highlight that both estimates of ϵ are consistent with one another, but we can not diagnose whether they are significantly biased against the true dissipation. A potentially important source of bias is our assumption of $\alpha = L_T/L_O = 0.8$. Observations [Mater et al., 2015] and numerical simulations [Scotti, 2015, Jalali et al., 2017] have highlighted that convectivelly driven turbulence may have $\alpha \ll 1$, whereas $\alpha = 0.8$ would be more appropriate for shear-driven turbulence [Dillon, 1982]. Since turbulence near-bottom turbulence in our region of study is

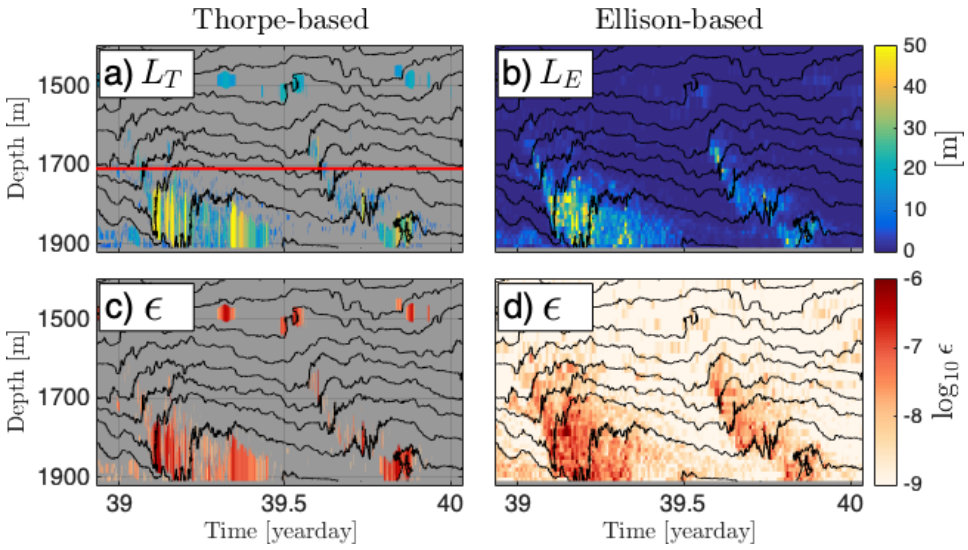

Figure 3.3: Comparison of dissipation rate (ϵ) estimates from Thorpe and Ellison scales from a 1-day subset of the T1 mooring record. (a) Thorpe scale (L_T), (b) Ellison scale (L_E), (c) ϵ from L_T, and (d) ϵ from L_E. Potential density (estimated from temperature measurements and a T-S polynomial fit) is contoured in all panels. Thermistors below the red line in (a) are spaced by 10 meters and the spacing increases further above. L_T is undefined where the observed potential density profile is stable. Shipboard observations (not shown) confirm that apparent overturns around 1500 meters are temperature inversions that are salinity-compensated. Dissipation rate from the Ellison scale is consistent with the one based on the Thorpe scale, it is not contaminated by salinity-compensated temperature inversions, it is not affected by changes in thermistor spacing, and it captures ϵ with overturns smaller than 10 meter (e.g. in the bottom 200 m for the event around yearday 39.75).

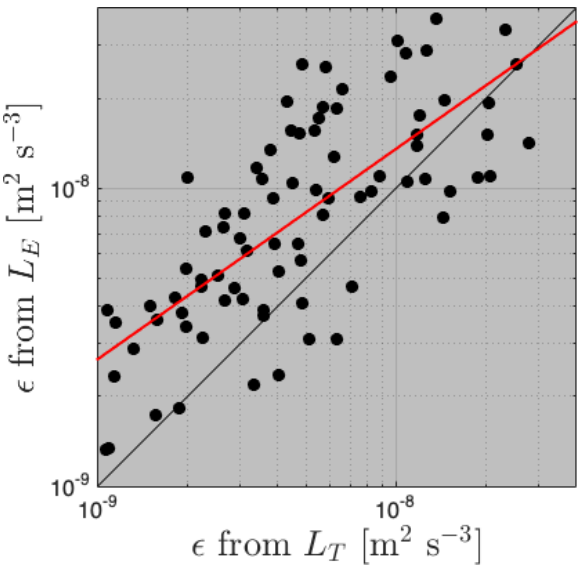

Figure 3.4: Semidiurnally and depth-averaged dissipation rate (ϵ) estimates based on the Thorpe scale (L_T) and the Ellison scale (L_E) from mooring (T1) observations. The black line is the one-to-one line and the red line is the least-squares fit. The correlation coefficient between the two estimates is 0.6.

associated with convective instabilities, our ϵ estimates may be biased high.

3.3 Tidal response over the bump

3.3.1 Numerical model

We begin by highlighting features of the tidal response over the bump in a numerical model (Fig. 3.5). The numerical model is the MITgcm and the set up is the same as in [Klymak et al., 2016], but with higher resolution to resolve the tidal response over small-scale topography. The model is only forced by a remote, M_2, mode-1 internal tide incident on the continental slope of Tasmania. The incoming wave was tuned to have a spatial structure consistent with satellite altimetry [Zhao et al., 2018], but the magnitude leads to higher energy than observed in our in-situ measurements. No forcing from the surface tide is included.

Since the slope around the bump is mostly supercritical, the tidal forcing on the bump leads

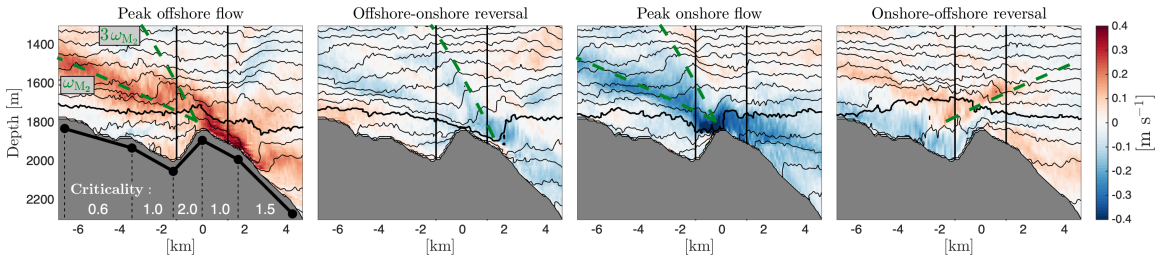

Figure 3.5: Timeseries of velocity and density around the bump over a semidiurnal tidal period from a 3D numerical model. The bottom criticality to the semidiurnal internal tide is shown in (a) and internal-wave characteristics for one and three times semidiurnal frequency are plotted for reference. Vertical black lines denote the locations of moorings T1 and T2 (see Fig. 3.2). Qualitatively, the modeled response around the bump has linear (i.e. internal tides radiating from the bump) and nonlinear (i.e. hydraulic jumps / tidal lee waves) components. In particular, we highlight that a tidal lee wave starts to develop at peak offshore flow around x = 2 km (a), it is advected onshore with the reversal of tidal flow (b), and it reaches the onshore side of the bump when the nonlinear response over the crest is developed at peak onshore tidal flow (c).

to radiation of internal tide beams both upward and downward along internal-wave characteristics. A more energetic upward, onshore propagating beam indicates that asymmetry in the bathymetry across the bump induces an asymmetric tidal response over the bump. Beams at higher harmonic are also generated and propagate along their corresponding characteristic further away from the horizontal direction. Moreover, the onshore propagating tidal beam highlights the non-local aspect of internal tides shoaling on a continental slope, where tidally driven dissipation further upslope is influenced by the generation of the beam at the bump (i.e. the two locations are the hotspots of dissipation in the northern region of the Tasman slope, see Fig. 3.1a).

In addition to the propagating rays, the near-field response is also asymmetric. At peak offshore internal-tide velocity (Fig. 3.5a), the flow is enhanced over the lee of the bump where the slope is near-critical. Further offshore, a hydraulic jump has developed where the slope is supercritical. At the reversal of tidal flow (Fig. 3.5b), a tidal lee wave has developed over the bottom ≈400 meters and propagates onshore. By the time of peak onshore internal-tide velocity, the lee-wave has propagated to the other side of the bump while an additional tidal lee wave response develops near the crest of the bump. At the onshore-offshore velocity reversal, the

offshore propagating response[1] is restricted closer to the bottom than its onslope propagating counterpart.

Steep isopycnals in the modeled response indicate locations and times of enhanced energy dissipation. At the crest of the bump, large dissipation rates are expected every half of a tidal period due to advection from either side of the bump. From the asymmetric response, larger dissipation rates at the crest are expected for onshore velocity relative to offshore flow. Moreover, the onshore propagating lee wave extends further up away from the bottom and can induce larger dissipation rates upon breaking. Finally, past the peak onshore tidal flow, low near-bottom stratification on the onshore side of the bump suggests active density overturns.

3.3.2 Observations

Observed cross-slope transects of velocity and dissipation rate support several features of the modeled tidal response (Figs. 3.5 and 3.6). In particular, the observations highlight the asymmetry between the onshore and offshore sides of the bump. For offshore flow, isopycnals plunge downwards past the crest of the bathymetry, ϵ is enhanced in the bottom 100 meters, and only a weak signal of vertical displacements can be observed hundreds of meters away from the bottom. For onshore flow, large ϵ is also observed near the bottom, but vertical displacements extend higher above the bottom.

Despite the asymmetry across the bump, average dissipation rates on either side of the bump are $O(10^{-8})$ m^2 s^{-3}. While a few overturns are up to 100 m, average height of overturns weighted by dissipation rate is about 30 m. Similarly, ϵ can be as high as $O(10^{-6})$ m^2 s^{-3} for individual overturns, but averaging in space and time (i.e. across repeated transects over a tidal period) gives dissipation of $O(10^{-8})$ m^2 s^{-3}.

Cross-slope transects taken 3 weeks apart show different responses for onshore tidal flow

[1]Hydraulic jumps and nonlinear lee waves lie in the same region of parameter space [Legg, 2021]. Moreover, there is no clear distinction between these phenomena in our observations. Hence, we also use the more generic term “tidal response".

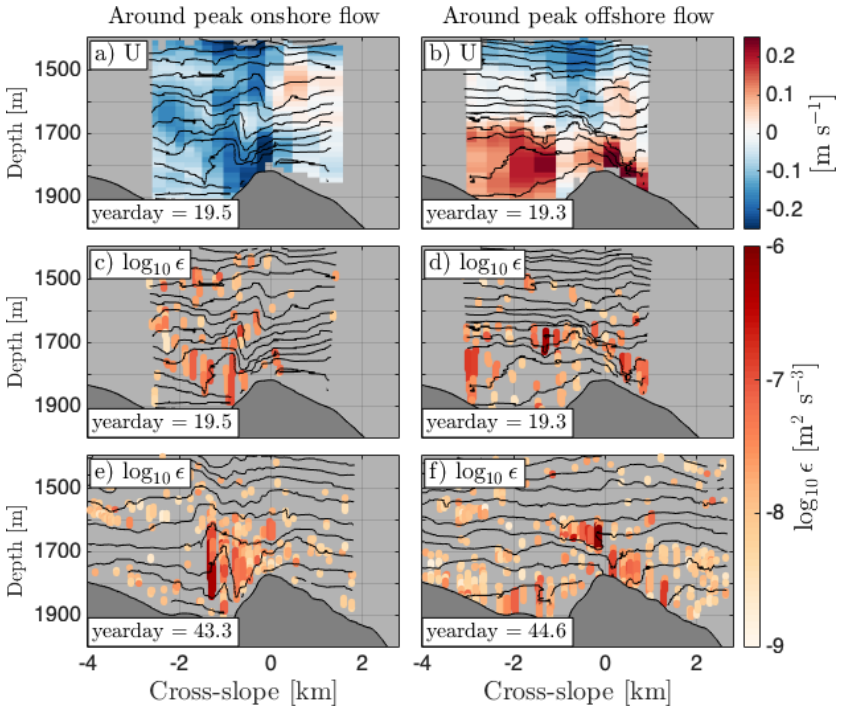

Figure 3.6: Cross-slope velocity and dissipation rate (ϵ) structure from observations taken around peak onshore (a, c, e) and offshore (b, d, f) tidal flow. CTD/LADCP observations of cross-slope velocity (a, b) and dissipation rate (c, d). Fast-CTD observations only provide ϵ (e, f). Mean flow (primarily along-slope the slope) was comparable to the tidal velocity when CTD/LADCP measurements were taken, whereas mean flow was small during Fast-CTD transects (see also Fig. 3.10). The asymmetric bottom slope leads to a tidal response that extends further away from the bottom on the onshore side of the bump.

(Fig. 3.6c, e). In the CTD/LADCP transect, the density structure within 1 km has vertical displacement leaning offshore with increasing height above the bottom. This structure is consistent with a nonlinear lee-wave response generated by the onshore tidal flow [Legg, 2021]. In contrast, the Fast-CTD observations capture displacements leaning in the opposite direction. The latter is more consistent with the model (Fig. 3.5c), where the density structure is associated with the onshore translation of the response generated by the offshore tidal flow. Observations around peak offshore tidal flow are similar between different transects (Fig. 3.6d, f).

Concurrent mooring and Fast-CTD observations resolved the onshore translation of the tidal response generated by offshore tidal flow (Fig. 3.7). At the transition from offshore to onshore tidal velocities, shipboard measurements near the crest of the bump capture a breaking lee wave in the bottom few hundred meters (Fig. 3.7a). Given the phase of tidal velocities (determined from the mooring data) and the observed overturns in the shipboard data, the breaking wave must be associated with the response set by the offshore tidal velocities. This response translates onslope and is later observed at the mooring. A rough speed estimate based on shipboard and mooring measurements suggests a translation of about 0.2 m s^{-1}. This speed is presumably a combination of both the onshore propagation of the lee wave (i.e. set by the magnitude of the offshore tidal current) and onshore advection by the forcing tide. The spatial structure of the wave propagating onslope explains the characteristic pattern observed at the mooring (Fig 3.7b, c, d), which resembles observations by [Musgrave et al., 2016]. Therefore, while freely upward propagating internal waves can be identified from downward phase propagation (e.g. [Gill, 1982]), the pattern captured by the mooring record is associated with the horizontal propagation of the trapped tidal response past the mooring.

Although the onslope translation of the lee wave is directly responsible for elevated dissipation rate at the mooring, near-bottom turbulence within the bottom 200 meters is also associated with alongslope tidal velocities later in the tidal cycle (i.e. after ~5 hours in Fig. 3.7b). Given the location of the mooring relative to the bump (Fig. 3.2a), wave breaking north of the

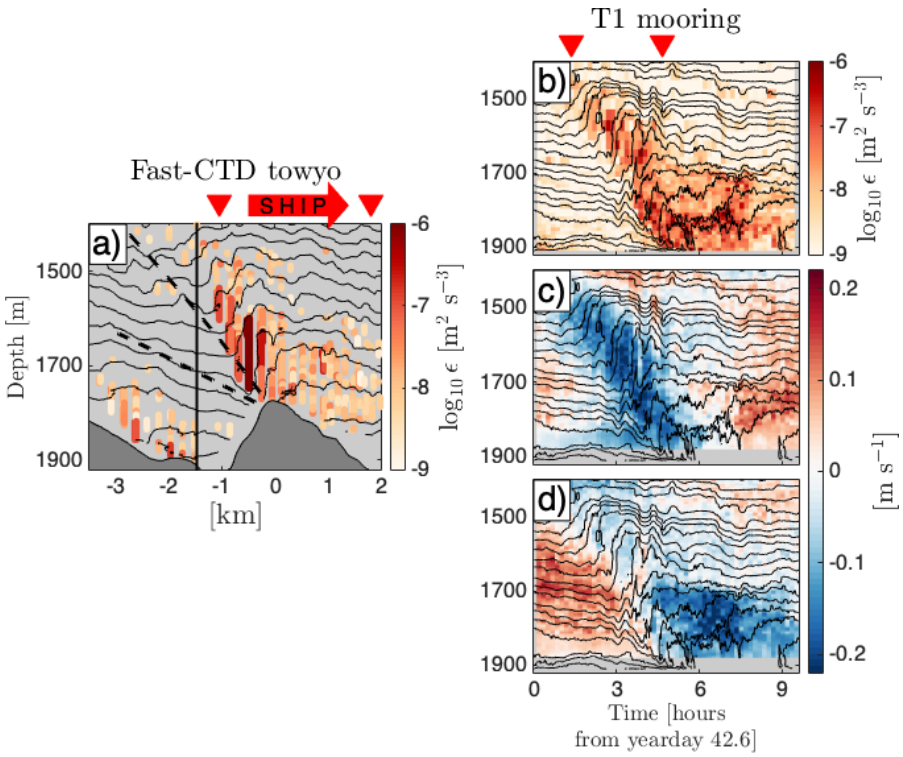

Figure 3.7: Spatial and temporal variability of the tidal response for onshore tidal flow and weak mean flow. (a) Overturn-based estimates of ϵ from a Fast-CTD transect (on yearday 42.6). Moored timeseries of (b) Ellison scale-based ϵ, (c) cross-slope, and (d) along-slope velocity. The location of the mooring (T1) is denoted by the vertical line in (a). The transect observations were taken with the ship moving offshore and the locations of the red triangles in (a) correspond to the times marked by the triangles in (b). Slanted dashed lines in (a) correspond to internal-wave characteristics at the semidiurnal and its second harmonic. As in the model (Fig. 3.5c), these observations show the onshore advection of the tidal response on the offshore side of the bump.

mooring and southward advection of turbulence explains the elevated near-bottom turbulence observed later in the tidal cycle.

The cross-slope advection of the tidal response over the bump is also captured by the adjacent timeseries from the mooring and the Fast-CTD station (Fig. 3.8). Similar to observations from [Dale and Inall, 2015], enhanced ϵ is observed twice per tidal period due to onshore and offshore advection of turbulence past the crest of the bump (Fig. 3.8b). The bursts of turbulence at the crest that coincide with onshore tidal velocity precede the enhanced turbulence on the onshore side of the bump captured by the mooring (Fig. 3.8c). These turbulent events are associated with the onshore translation of the tidal response. The cross-slope structure and the onshore propagation of the tidal response (Fig. 3.7a) explains the different patterns of the same feature observed at two nearby locations: the observations over the crest of the bump capture a near-bottom burst of dissipation rate, and the mooring sees a downward phase propagation pattern on the onshore side.

For the limited 2-day period of the Fast-CTD station, the largest ϵ event (i.e around yearday 45) does not exhibit the signature of the onshore propagation. Instead, this turbulent event appears to be more associated with the southward advection than the direct onshore translation of the tidal response past the mooring. Offshore tidal advection of this energetic event explains the enhanced ϵ subsequently observed higher up in the water column over the crest of the bump (Fig. 3.8b).

Several of the features discussed above are summarized by the depth-averaged tidal velocities and dissipation rate around the bump (Fig. 3.9). Near-bottom ϵ is enhanced on the side of the tidal ellipses further from the crest of the bump. This pattern is a signature of the dissipation driven by the cross-slope dynamics of the tidal flow, where dissipation rate generally increases after the peak of the cross-slope tidal velocity away from the crest of the bump. Moreover, dissipation advected by southward velocity at the T1 mooring leads to larger ϵ on the southwest quadrant of the ellipse.

However, tidal ellipses are not polarized in the cross-slope direction as would be expected

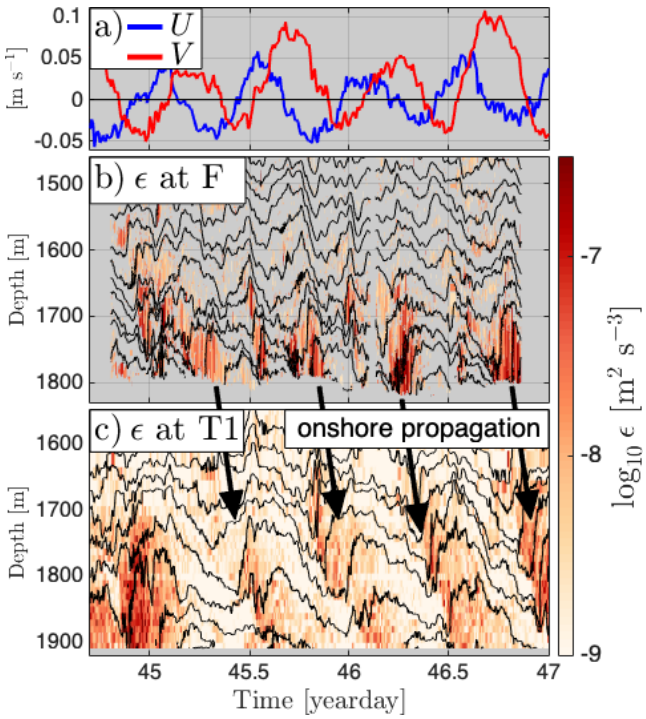

Figure 3.8: Moored (T1) and shipboard (F) timeseries observations on the onshore side and on the crest of the bump, respectively. (a) Depth-averaged (from 20 to 550 m above the bottom) cross-shore (U) and alongshore (V) velocity at T1, (b) overturn-based dissipation rate (ϵ) from the Fast-CTD station, and (c) Ellison scale-based ϵ from T1 mooring data. Near-bottom turbulence on the crest of the bump (b) is enhanced every ≈6 hours due to both onshore and offshore tidal propagation. Mooring T1 only captures the turbulence on the onshore side and the dominant period is the semidiurnal period. Fig. 3.7 demonstrates how the onshore propagation of the tidal response leads to the slanted pattern of elevated dissipation in the timeseries. Arrows from (b) to (c) indicate the turbulent patches associated with the onshore propagating tidal events.

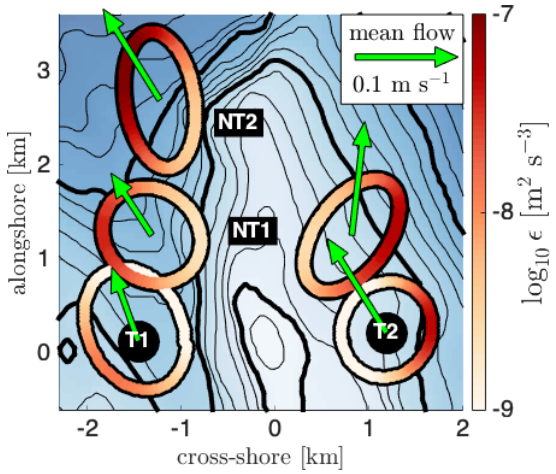

Figure 3.9: Spatio-temporal variability of dissipation rate around the bump. Tidal ellipses, dissipation rate (ϵ), and mean flow (green arrows) were estimated from concurrent mooring (T1 and T2) and CTD/LADCP towyo (NT1 and NT2) observations taken over the course of 3.5 days (between yeardays 18.5 and 22). All estimates are based on depth-averaged quantities between 1500 m and the bottom. We have plotted harmonic fits to the observed dissipation rate. Tidal ellipses correspond to progressive vector diagrams calculated from semidiurnal tidal velocities. Vectors and ellipses are consistently scaled (i.e. a circular tidal ellipse would be produced by a tidal velocity with a peak value equal to the radius of the circle). The variability of dissipation within a tidal cycle is similar at all locations and consistent with transient lee-wave expectations (i.e. the maximum dissipation is observed after the peak velocity away from the bump). Tidal ellipses are not aligned in the cross-slope direction.

if the dynamics could be reduced to this horizontal direction. The ellipses are also not polarized along a single direction that could be related to an angle of incidence for the incoming wave. Moreover, the tidal ellipse at T1 is aligned with the canyon-like bathymetry around the mooring.

3.4 Temporal variability

Our ~45-day mooring record indicates that near-bottom turbulence is primarily driven by the semidiurnal tide (Fig. 3.10). The semidiurnal variability of dissipation rate is modulated at lower frequencies by an envelope consistent with the depth-averaged tidal speed (Fig. 3.10c-e). However, this envelope is not associated with a spring-neap cycle. Instead, the variability is dominated by episodic bursts that last for 3 to 6 days.

Early in the timeseries (i.e. until yearday 25), the background velocity is comparable to the tidal velocity (0.1 m s^{-1}). Although dissipation rate has semidiurnal variability, elevated background turbulence (Fig. 3.10c) suggests the mean flow may also play a significant role. In the following month (between yeardays 25 and 55), the mean flow is smaller than the tidal velocity and dissipation rate is enhanced over 5 bursts. Qualitatively, visual inspection of dissipation in these bursts indicates the downward phase propagation pattern (as in Figs. 3.7b-d). Towards the end of the record (after yearday 55), tidal velocities extend higher above the bottom than earlier in the timeseries, ϵ does not have a the characteristic pattern seen at the bursts, and the magnitude of dissipation is not as large as might be expected from the tidal speed. These qualitative differences suggest three distinct periods in the timeseries, such that scaling relationships should be computed for each period separately (we do this in Fig. 3.14, section 3.6).

The temporal variability in the mean flow is possibly associated with the different observed cross-slope structures of the tidal response. Without a mean current (as in the model, Fig 3.5), the lee wave due to offshore tidal flow is able to propagate onshore and be observed by the mooring (Fig. 3.6e). This wave may have its formation or propagation modified by a large alongshore

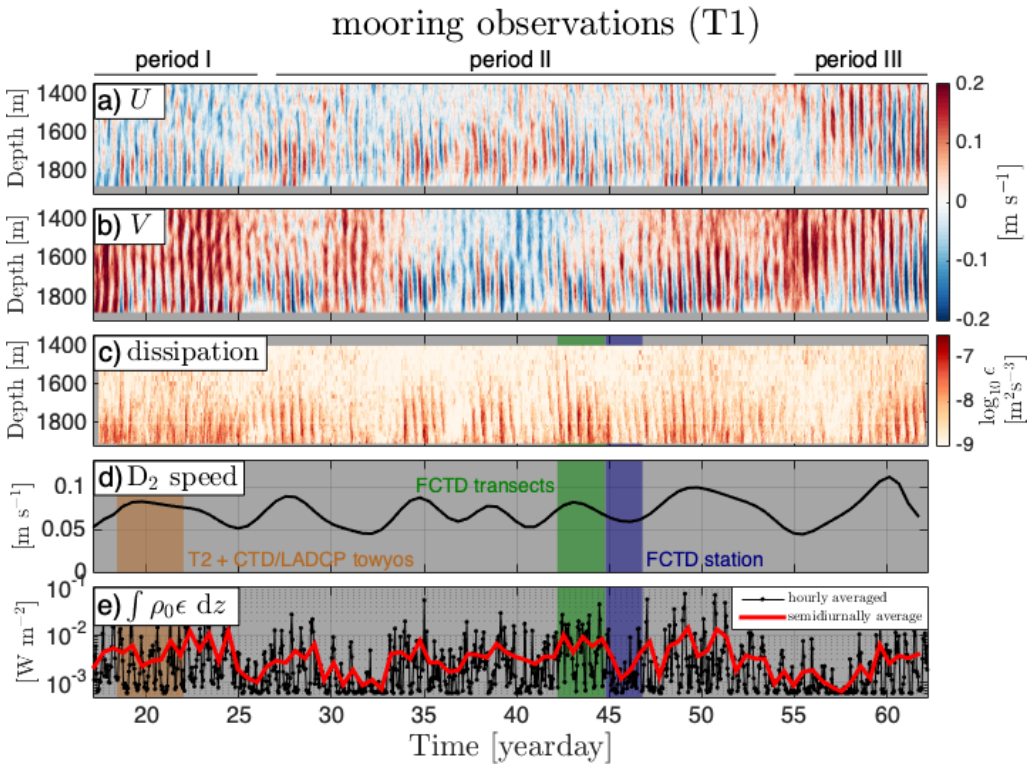

Figure 3.10: Timeseries of velocity and dissipation rate over the course of the T-TIDE experiment from mooring T1. (a) Cross-slope and (b) along-slope velocity components, and (c) semidiurnal tidal speed averaged below 1600 m, (d) $\log_{10}$ of dissipation rate based on the Ellison scale, and (e) depth-integrated dissipation (over the full vertical range of the observations). The colored shading indicates times when we took additional observations. The three periods are defined from qualitative features of velocity and dissipation (see section 3c). Mean flow is most energetic (and northward) in the first week of data (until yearday 25) and small at the time of the Fast-CTD observations. Note that near-bottom turbulence is related to the semidiurnal tidal speed.

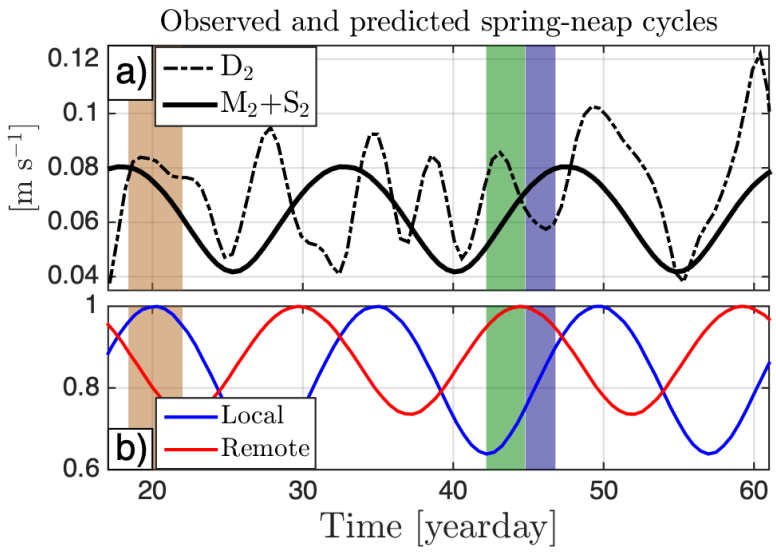

Figure 3.11: Observed spring-neap cycle and prediction of its phase from local and remote tides. (a) Depth-averaged semidiurnal (D2, dashed) speed and its stationary (M_2+S_2, solid) component. (b) Normalized tidal speed from TPXO on the Tasman slope (blue) and at Macquarie Ridge (red). The latter is shifted by the travel time of the mode-1 internal tide (9.3 days). Note the spring-neap computed from the observations has an intermediate phase to the local and remote fortnight cycles.

current, and the lee wave due to onshore tidal flow is able to develop (Fig. 3.6c).

Depth-integrated dissipation ranges between 1 and 10 mW m^{-2} (Fig. 3.10e), where the depth integral is calculated over the full range of available observations (i.e. in the bottom 600 m). Relative to a global parameterization of tidal dissipation [de Lavergne et al., 2020], our study site is a region of modestly large near-bottom tidally driven turbulence.

While there is no obvious spring-neap cycle, the phase of the fortnight variability (calculated from harmonic fits to the M_2 and S_2 frequencies) is intermediate to the predictions from the surface tide and from the remote internal tide (Fig. 3.11). These predictions are based on semidiurnal tides from the TOPEX/Poseidon Global Inverse Solution (TPXO) 7.2 [Egbert and Erofeeva, 2002] extracted at the Tasman slope and at the generation site of the remote internal tide. The spring-neap cycle of the latter is shifted in time by the travel time of the remote wave (i.e. ≈9.3 days, computed following [Marques et al., 2021]).

We propose that local and remote tides play comparable roles in driving the tidal

response over the bump and the near-bottom dissipation. Their interference can lead to a total spring-neap cycle with intermediate phase to those from the individual tides. Each burst in tidal velocity and dissipation is perhaps associated with primarily local or remote forcing. Furthermore, their interference is sensitive to small changes in the travel time of the remote wave [Marques et al., 2021] and may lead to bursts of dissipation that unexpectedly occur during neap tides (i.e. around yearday 39).

3.5 Tidal forcing

Evidence of tidal forcing by the remote mode-1 internal tide is provided by velocity data from the mooring and shipboard sonar at the time of the Fast-CTD station (Fig. 3.12). The continental slope offshore from the bump is supercritical until the seafloor is about 3200 meters, after which the slope is generally subcritical. Our conceptual picture is that an incoming mode-1 internal tide shoals (between water depths of about 4500 and 3200 meters) and then scatters on the steep part of the continental slope around the bump.

In this scenario, the semidiurnal cross-slope velocity profile should change sign near the depth of mode-1 crossing (calculated at 3200 meters). This pattern is roughly observed from the mooring and shipboard data, where tidal velocities in the upper ocean (between 400 and 900 meters) and near the bottom (below 1600 meters) have opposite phase. Moreover, the tidal ellipse from the depth-averaged velocity in the upper part of the water column indicates an angle of incidence consistent with a regional model [Klymak et al., 2016] of the incoming internal tide. In contrast, the direction of the tidal ellipse from near-bottom velocity is aligned with the bathymetry on the onshore side of the bump. A nonlinear tidal response with magnitude comparable to its forcing qualitatively explains the large near-bottom velocities relative to those higher above in the water column.

However, the velocity profile does not constrain the magnitude of the incoming tide.

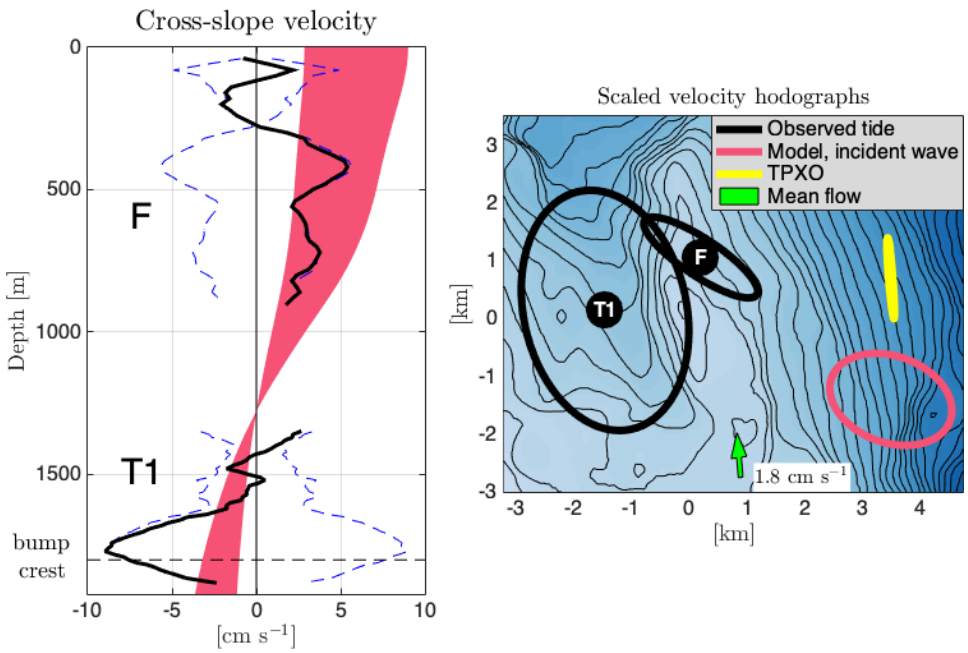

Figure 3.12: Semidiurnal tidal velocity profile on top of the bump and tidal velocity hodographs. Tidal fits are based on 2 days of data around yearday 46 from the HDSS (above 1000 meters) and mooring T1 (below 1300 meters). (a) Zonal (approximately cross-slope) semidiurnal velocity profile at a specific time (black), peak tidal velocity (dashed blue), and mode-1 velocity profiles for a range of incident depth-integrated energy fluxes (0.8 to 8 kW m^{-1}). The mode-1 velocities are calculated for a total water depth of 3200 meters, which is just offshore from the region where the continental slope is supercritical. (b) Tidal ellipses from vertically averaged velocity in the upper ocean and closer to the bump (black), mode-1 velocity ellipse at the crest of the bump (1800 meters) for an incoming energy flux of 4.5 kW m^{-1} (pink), and TPXO tidal ellipse (purple). For visual purposes, all tidal ellipses are scaled by a factor of 6 (i.e. tidal excursions are a factor 1/6 shorter than displayed). The reference velocity vector corresponds to the mean velocity observed at T1. While the observed tidal velocities near the bottom are larger than what would be expected, both the velocity profile and the upper ocean tidal ellipse are qualitatively consistent with an incoming mode-1 internal tide. The tidal ellipse from velocities closer to the bottom (T1) suggest the tidal flow is somewhat constrained by the details of the bottom topography on the onshore side of the bump.

Several factors can preclude a quantitative estimate: the comparable magnitudes of tidal forcing and response under nonlinear dynamics; the sensitivity of the energy flux due to the scaling with velocity squared; near-bottom velocity enhancement of the incoming tide while shoaling over subcritical topography [Wunsch, 1968]; and perhaps large-wavenumber internal tides near the surface.

Our conceptual scattering model is specific to the incoming mode-1 internal tide. However, the timeseries suggest that the local surface tide may also be a significant forcing (Fig. 3.11). It is unclear how the surface can lead to a similar response over the bump but, with surface tide velocity polarized in the alongshore direction, our conceptual model is not valid. In this context, coastally trapped waves (i.e. which are leaky at superinertial frequencies), might be excited and play a key role [Musgrave, 2019, Brink, 2021]. In fact, even with remote forcing alone, our conceptual 2D model does not explain comparable cross-shore and alongshore tidal velocity components. Trapped waves forced by the incoming internal tide, which are present in the regional numerical simulation [Klymak et al., 2016], might be responsible for relatively large alongshore tidal velocities near the bump.

3.6 Observations and theoretical scalings

We now take a step back from the complexity of the observations and address whether they can be roughly explained by theoretical predictions of tidal flow over supercritical topography [Klymak et al., 2010b, Klymak et al., 2010a, Klymak et al., 2013].

3.6.1 Lee-wave adjustment time

[Klymak et al., 2010b] explored the nonlinear regime of high-mode lee waves generated by a constant flow over an isolated obstacle. For temporally variable forcing, the adjustment time scale is important to determine whether the lee wave can develop before substantial variability

of the forcing. Based on the group velocity, the time scale for the wave to propagate over one vertical wavelength is

$$\Delta t \equiv \frac{2\pi}{\alpha_{\mathrm{ef}} N}, \tag{3.6}$$

where α_{ef} is the effective aspect ratio of the topography and N is the buoyancy frequency. Qualitatively, the effective aspect ratio is associated with the region near the crest of the obstacle, because the horizontal length is set by the tidal excursion instead of the full width of the obstacle [Klymak et al., 2010a].

For tidal flow over a bump, a transient lee wave can only develop on each side of the topography if Δt is shorter than half of a tidal period. Δt scales with the inverse of the criticality parameter, such that a criticality of two approximately corresponds to a lee wave propagating over one vertical wavelength before the reversal of the tidal velocity [Klymak et al., 2013].

Similar to [Voet et al., 2020], we determine aspect ratios for different segments of the topography by fitting Gaussian curves. Considering 1-km adjacent segments onshore from the crest, on the offshore side, and further offshore (Fig. 3.2b), the time scales are about 4, 10, and 6 hours, respectively. Not only does the longest time scale indicates no lee wave associated with the corresponding piece of topography, but its near-critical slope likely induces dynamics beyond the range of validity of (3.6).

The supercritcal regions on the onshore side and around 2 km offshore from the bump can support a lee-wave-like response. The shortest time scale indicates a more well-defined lee wave on the onshore side than that on the offshore side, which is roughly consistent with observations (see Figs. 3.6a and 3.13). Nevertheless, these time scales are not much smaller than one half of a tidal period. Therefore, although our observations do not extend into the upper 1000 m, the tidal lee waves are not expected to propagate for several wavelengths away from the bottom. Moreover, the offshore supercritical slope is not immediately adjacent to the crest of the bump, which might be an additional factor that leads to wave forms in the observations (Fig. 3.7a) that differ from theory over an idealized bump [Klymak et al., 2010a].

3.6.2 Lee-wave structure

The cross-slope towyo observations give a good example of the onset and breaking of a tidal lee wave formed on the onshore side of the bump (Fig. 3.13). For a transect taken just after the peak onshore tidal flow (Fig. 3.13b, d), the spatial structure of velocity and density surfaces are qualitatively consistent with the high-mode theoretical lee wave [Klymak et al., 2010b]. On the crest of the bump, the largest velocity is observed near the bottom ($\approx 0.2-0.3$ m s^{-1}) with another local maximum of onshore velocity between 200 and 400 m above the bottom (Fig. 3.13b. See also Fig. 3.6a). This rough vertical distance presumably corresponds to one vertical wavelength of the transient lee wave. In the subsequent transect (Fig. 3.13c, e), when the tidal velocities reverse from onshore to offshore, vigorous wave breaking is observed. Due to wave propagation and advection, lee-wave features in the density surfaces are observed further offshore and higher above the bottom.

The expected lee-wave vertical wavelength is

$$\lambda_z = 2\pi \frac{U}{N}, \tag{3.7}$$

where U is a velocity scale of the forcing and N is the buoyancy frequency [Klymak et al., 2010b]. With observed $N \approx 1.7 \times 10^{-3}$ s^{-1} and $\lambda_z \approx$ 300-400 m, the required U for the theory to match the observations is 8-11 cm s^{-1}.

While the background buoyancy frequency can be calculated from our observations, the velocity scale can not be unambiguously obtained. In (3.7), U is a scale for the forcing, which is the peak velocity magnitude for oscillatory flow. The observations only capture a combination of the forcing with the response and, for nonlinear phenomena, they both have comparable magnitudes.

Our best approach to obtain a reasonable U from the observations is to use the towyo data in an attempt to average out the high-mode tidal response. We averaged the velocity observations in the vertical (above the height of the bump), in the cross-slope direction (all profiles for

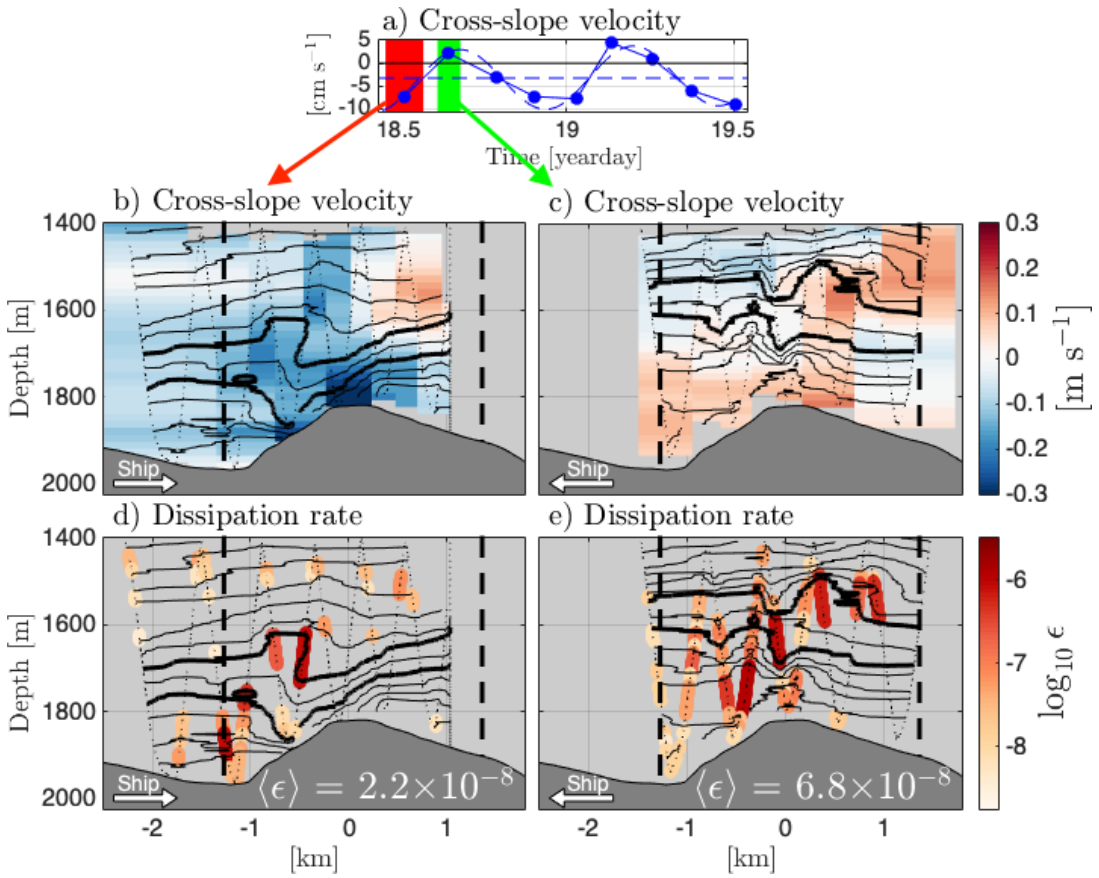

Figure 3.13: Observations of a breaking transient lee wave forced by onslope tidal flow over the bump. (a) Timeseries of average cross-slope velocity for all NT1 transect repeats. Averages are computed over depth (between 1450 and 1800 m) and over the cross-slope direction (using all profiles in each transect). The observations are shown by the dotted line (i.e. the dots correspond to the average velocity of the 9 transects) and the mean by the horizontal dashed line. (b)-(c) Cross-slope velocity from the first two NT1 transect repeats, and (d)-(e) corresponding overturn-based dissipation rates. Dissipation is only plotted where overturns are observed. Overturns in downcasts, when the CTD at the bottom of the rosette samples undisturbed water by the instrument package, are consistent with overturns in adjacent upcasts. Contours of equally spaced potential density surfaces (two are thicker for visual reference). The vertical dashed lines are the location of moorings T1 and T2 (on the onshore and offshore sides, respectively). Thin dotted lines indicate the path of the profiling CTD. White arrows in the bottom left of (b)-(e) show the direction in which the ship moved. Average dissipation ($\langle\epsilon\rangle$ in W kg^{-1}) for each transect is shown in (d) and (e). Before averaging, undefined ϵ (i.e. where overturns are not observed) are replaced by a background value of 10^{-9} W kg^{-1}.

each transect), and then calculated a harmonic fit from the averaged velocity (Fig. 3.13a). In the harmonic fit, we solved for the parameters of a linear trend and a sinusoidal with (lunar) semidiurnal period. We find a cross-slope mean flow and peak tidal current of 3 and 7 cm s^{-1}, respectively. Since the mean flow is onshore, its combined effect with the semidiurnal tide gives $U \approx 0.1$ m s^{-1}. Through (3.7), this velocity scale predicts a vertical wavelength that agrees with that inferred from the observations. Therefore, we conclude that the tidal response captured by the NT1 towyo on the onshore side of the bump is consistent with the high-mode lee wave theory [Klymak et al., 2010b].

There are several caveats worth pointing out. The λ_z inferred from the observations is clearly only a rough estimate. Although there are limitations in the measurements, it is important to bear in mind the observations in the real ocean are more complex that in an idealized scenario. For example, an accurate estimate of the vertical wavelength would not only require observations extending further above the bottom, but the wave itself would need to propagate for several vertical wavelengths before the relaxation of the tidal forcing. As previously discussed, the bottom slope is not sufficiently steep for the wave to propagate far away from the bottom. Finally, the observed lee wave generated on the onshore side is based on observations from early in the record (i.e. period I in Fig. 3.10). For the bulk of the timeseries (i.e. period II in Fig. 3.10), enhanced velocity and dissipation is associated with the onshore advection of the tidal response generated on the offshore side (Fig. 3.7).

3.6.3 Tidal scattering and dissipation

Although the structure of the tidal response depends on the details of the topography, the scattering of the forcing tide is presumably associated with the supercritical topography on which the bump is embedded (Fig 3.2b). In other words, if the idealized scattering due to a knife-edge ridge is a reasonable approximation, the energy that is lost to dissipation does not depend on the details of the bump. In this case, we can solve a scattering model to calculate the energy flux

distribution into vertical modes and assume that higher (slower) modes than a critical number lead to the dissipation near the topography [Klymak et al., 2010a].

Following the recipe outlined [Klymak et al., 2013], we make an estimate of dissipation from a simple model. The model geometry consists of a flat bottom with a knife-edge ridge. The depth of the flat bottom is set to 3200 m, which roughly corresponds to the transition between subcritical to supercritical topography offshore from the bump (Fig. 3.2b). The knife-edge scattering problem has simple solutions for constant stratification [St. Laurent et al., 2001]. To account for depth-varying stratification on the Tasman slope, we WKB-scale the vertical coordinate [Leaman and Sanford, 1975]. The height of the ridge in the model (i.e. in the WKB-scaled coordinate) is 750 m (instead of 1400 m in the real ocean). The buoyancy frequency profile was calculated from climatological data [Boyer et al., 2013], which is consistent with observations at depths where the latter are available.

As discussed earlier, our observations in northeastern Tasmania do not constrain the magnitude of the incoming internal tide. However, a comparison between observations in southeastern Tasmania and a regional numerical model yields a rough incident energy flux estimate between 2.3 and 5.5 kW m^{-1} [Marques et al., 2021]. The range corresponds to the variability between neap and spring tides. From the same regional model [Klymak et al., 2016], the incident energy flux in southeastern Tasmania is about twice of that on the northeastern slope. Therefore, reasonable upper and lower bound estimates for the incident flux of the internal tide scattering on the bump are 1 and 2.5 kW m^{-1}, respectively. We used these estimates to set the incident mode-1 energy flux in the scattering model.

The inferred dissipation from the [Klymak et al., 2013] recipe ranges between 12 and 42 W m^{-1}. To compare with the mooring observations, the total dissipation has to be divided by a characteristic ridge width, which is about 5 km. Therefore, the predicted depth-integrated dissipation rate is roughly 2 to 8 mW m^{-2}. Given the simplicity of this idealized recipe, the many assumptions involved, and an observed dissipation between 1 and 10 mW m^{-2} (Fig. 3.10e), we

conclude the model successfully predicts the magnitude of ϵ. Along with the observed velocity profile (Fig. 3.12), the agreement between model and observations further supports that the remote internal tide scatters around the bump. Coupled with the nonlinear dynamics at the crest, the incident wave can sustain the magnitude of the observed dissipation.

Observations can also be compared to the theoretical scaling [Klymak et al., 2010a] between tidal forcing and dissipation. Although the observations do not provide an unambiguous estimate of the forcing alone, we compared the theoretical scaling with our moored velocity and dissipation. First, we regridded the variables in terms of the semidiurnal phase instead of time, such that semidiurnal events of enhanced ϵ can be treated separately. For the semidiurnal velocity, the peak velocity was calculated at all depths. We then computed depth averages over the full range of the mooring observations, which is our best option to partially average out the effect of the tidal response and obtain a closer estimate of the forcing.

For most of the timeseries (period II), the observations are roughly consistent with ϵ proportional to the tidal velocity cubed (Fig. 3.14). This is the same scaling as in the case of dissipation driven by the scattering of the surface tide [Klymak et al., 2010a]. A general scaling does not exist for internal tide forcing because the velocity is not constant in the vertical [Klymak et al., 2013]. Since the height of the topography does not extend above the mode-1 crossing depth (Fig. 3.12), the scattering of the mode-1 internal tide might be similar to that of the surface tide. This approximation may be responsible for the observed scaling of dissipation with the tidal velocity magnitude.

We note that the regression was only computed for one month of data (i.e. period II, Fig. 3.10), because differences in the mean flow and vertical structure of the tides suggest that each period should be treated separately. Moreover, the other periods in the timeseries have less data and corresponding errors on the regression slope are larger.

Despite the general agreement between observations and theory, different attempts to scale dissipation with velocity highlight features beyond the scope of theoretical scaling. Simulations by

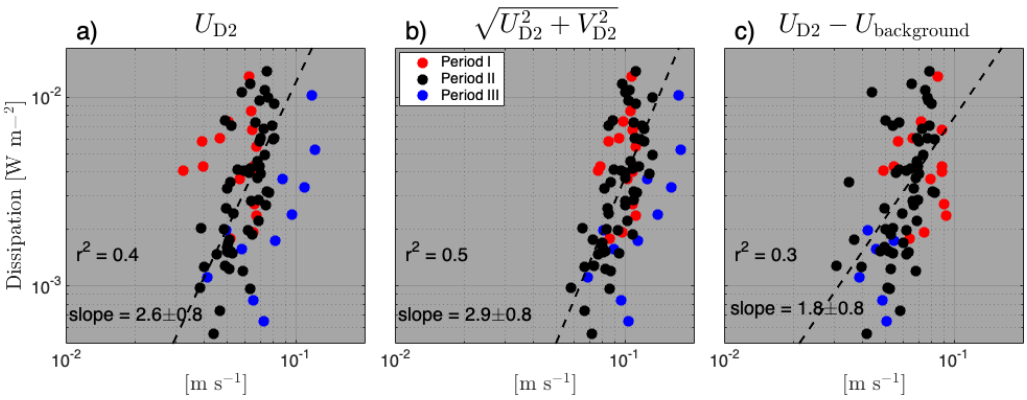

Figure 3.14: Scaling between velocity scales and depth-integrated dissipation. Scaling with (a) peak cross-slope semidiurnal velocity magnitude, (b) peak semidiurnal velocity magnitude, and (c) tidal minus mean flow velocity. Data is color coded for the three periods of the data (see Fig. 3.10). Regressions and correlation coefficients squared (r^2) are only calculated for period II. The regression slope is shown along with its error for a 95% confidence interval. Cross-slope mean flow (i.e. background) is smaller than peak tidal current at all times, such that regression with dissipation (which is greater than zero by definition) is well-defined. Observed regression slopes with peak tidal current are roughly consistent with the third-power theoretical scaling from [Klymak et al., 2013]

[Klymak et al., 2010a] considered two-dimensional ridges forced by tidal motion alone. Although the cross-slope tidal velocity yields results consistent with theory (Fig. 3.14a), the tidal speed (Fig. 3.14b) seems to be a more appropriate velocity scale. Moreover, although we previously argued for the combined effect of tides and mean flow in setting the lee-wave wavelength, attempts to incorporate the mean flow in the scaling with dissipation did not improve the correlation. In fact, given the differences between periods, such as the relative importance between the lee wave formed on the onshore side (Fig. 3.13) and the onshore translation of the response from the offshore side (Fig. 3.7), it is unclear how the mean flow should be incorporated on these observationally based scalings.

The conceptual picture of scattering and turbulence has also been successfully applied to other continental slopes. Moored observations in the South China Sea [Klymak et al., 2011] suggest that a large fraction (up to ≈40%) of the incoming diurnal internal tide may dissipate through scattering over supercritical topography at the offshore edge of the continental slope. On the Oregon slope, a hotspot of dissipation is also observed over a steep rise of the continental

slope from the abyssal plain [Nash et al., 2007], and the fraction of the wave that propagates onshore may dissipate through successive regions of scattering over supercritical topography [Kelly et al., 2012].

On the Tasman slope, the scattering model indicates that turbulence over the bump can only dissipate about 1% of the incoming internal-tide energy flux. As suggested by additional in-situ observations [Schlosser et al., 2019], the incident wave does not reach the continental shelf. Therefore, a significant fraction of the incident internal tide on the northeastern Tasman slope is expected to shoal within the continental slope, but almost entirely dissipate or reflect until the shelfbreak.

3.7 Summary

Motivated by a well-defined internal tide source [Pinkel et al., 2015, Zhao, 2016], we studied in-situ observations off of Tasmania to understand the energy fate of a remote internal tide impinging on the continental slope. In this paper, we have combined model output, mooring and shipboard observations to study the turbulent processes over a $O(100)$ m tall topographic bump. We summarize our primary findings as:

1. Indirect estimates of moored dissipation rate can be obtained from Ellison scales, which have advantages relative to Thorpe scales for mooring data (Fig. 3.3 and 3.4).

2. Consistent with the model results, spatially resolving measurements capture the cross-shore asymmetry of the tidal response at $O(1)$ km scale and are essential to interpret isolated timeseries (Figs. 3.5-3.8).

3. The cross-slope tidal flow over the bump drives most of the near-bottom turbulence around the bump (Figs. 3.9-3.10).

4. The tidal response and dissipation has episodic temporal variability and it is likely driven by both the local tide and the remote mode-1 internal tide (Figs. 3.10-3.12).

5. The observations of the tidal response and dissipation are qualitatively consistent with theoretical predictions of tidal lee waves and scattering over supercritical topography (Fig. 3.13-3.14).

The suite of observations, aided by the numerical model results, provides a rich description of turbulent processes around the bump. Within the context of tidally driven deep-ocean turbulence, adequate sampling of a rapidly evolving velocity and density field is a challenging task. Combining temporally and spatially resolving observations is crucial to characterize the tidal response, track its evolution over the tidal cycle, and describe temporal variability over longer time scales.

We have shown that tidally driven dissipation in our site is consistent with high-mode tidal lee-wave theory. Although this is similar physics to that observed over large-scale ridges [Alford et al., 2014, Musgrave et al., 2016], our observations suggest that both the local surface tide and the remote internal tide drive the observed turbulence. Nevertheless, longer timeseries and observations constraining the tide would be necessary to understand the low frequency modulation of observed dissipation over the bump and whether the mean flow can also play a significant role. Finally, it remains to be demonstrated whether the type of phenomena that we have observed is a significant contribution of turbulence in the abyssal ocean.

3.8 Acknowledgements

Chapter 3, in part is currently being prepared for submission for publication of the material. Marques, Olavo B.; Alford, Matthew H.; Pinkel, Robert; MacKinnon, Jennifer A.; Klymak, Jody M.; Nash, Jonathan D. The dissertation author was the primary investigator and author of this paper.

Chapter 4

Near-bottom upwelling along corrugations in the continental slope of Tasmania

4.1 Introduction

Small-scale diapycnal mixing has important effects to the state of the deep ocean [Melet et al., 2016]. For example, the lower meridional overturning circulation has a significant component across density surfaces in the abyssal ocean [Lumpkin and Speer, 2007], such that its strength directly depends on diapycnal mixing [Cessi, 2019]. Even for the upper overturning circulation, with is intrinsically more adiabatic, mixing is important in regulating the meridional oceanic heat transport [Hieronymus et al., 2019, Holmes et al., 2019]. Therefore, understanding the energy sources that power deep-ocean mixing and the associated small-scale turbulent processes can improve ocean general circulation models [MacKinnon et al., 2017].

Elevated deep-ocean turbulence is often observed[1] above rough topography, where it is generally bottom-enhanced over vertical scales of $O(100-1000)$ m above the bottom [Polzin et al., 1997, Waterhouse et al., 2014, Kunze, 2017]. However, water parcels embedded in

[1] More precisely, profiles of the dissipation rate of turbulent kinetic energy (ϵ).

this vertical structure mix more vigorously at their bottom than at their top, becoming denser, which leads to downwelling instead of upwelling [Ferrari et al., 2016]. To reconcile the upwelling estimated from large-scale measurements with a local inference of downwelling, the effects of bathymetry in near-bottom mixing must be accounted for. For a water parcel bounded from below by sloping seafloor, mixing from above leads to upwelling within a bottom-boundary layer (BBL). Over abyssal canyons, profiles of ϵ can also be elevated around their rim depth, thus decreasing towards the bottom, and leading to upwelling locally. In fact, consideration of the shape of the bathymetry (i.e. hypsometry) is also important important to consider the integrated upwelling [Kunze et al., 2012, McDougall and Ferrari, 2017, Thurnherr et al., 2020]. While there are several open questions on boundary mixing in the ocean, the current paradigm is that, as observed by [St. Laurent et al., 2001], abyssal upwelling is the net result of downwelling and upwelling circulations, which are coupled by rough topography [Polzin and McDougall, 2021].

The energy that supports boundary mixing in the deep ocean is thought to originate from tides, winds (through the generation of near-inertial waves), and the large-scale circulation [MacKinnon et al., 2017]. While there is observational evidence for near-bottom turbulence induced by all three energy reservoirs [Whalen et al., 2020], it is often hard to relate the dynamics of the energy containing scales to the induced boundary mixing. [Spingys et al., 2021] is a recent effort along this direction, where they observed boundary mixing associated with a Deep Western Boundary Current. For near-bottom mixing induced by internal tides, large turbulence estimates (i.e. dissipation rates or diffusivities) are often measured but without consideration of dynamics of the diapycnal upwelling [Dale and Inall, 2015, van Haren, 2017]. In this context, [Kunze et al., 2012] is a notable exception, although they did not have direct velocity observations.

As part of the The Tasman Tidal Dissipation Experiment (T-TIDE), we observed the the internal tide on the continental slope off Tasmania and associated near-bottom turbulent processes. The primary source of the internal is an incident remote mode-1 tidal beam that is generated over Macquarie Ridge, $\approx$14000 km to the southeast of Tasmania. From model and

observations, the southeastern slope primarily reflects the incoming wave without mode transfer. In contrast, the incident wave on the northeastern is more prone to scattering to higher modes [Johnston et al., 2015, Klymak et al., 2016, Marques et al., 2021].

Although the southeast continental slope of Tasmania is highly reflective to the mode-1 internal tide, small-scale corrugations lead to substantial spatial variability of the internal tide energy [Marques et al., 2021]. Moreover, the trough of these corrugations is associated with persistent onshore subtidal velocities, which suggest upwelling along the sloping bottom (Fig. 4.1b and [Marques et al., 2021]). The goal of this paper is to investigate the dynamics of the near-bottom subtidal flow and potential connections with the internal tides and boundary mixing.

We first describe our mooring and shipboard measurements (section 4.2). We then present our velocity observations and the adjustment of the flow to the corrugated topography (section 4.3.1). Although there are large uncertainties, we compare indirect and direct vertical velocities, which are not inconsistent with one another (section 4.3.2). We then focus on the unexpected connections between near-bottom turbulence, the subtidal flow, and the internal tide (section 4.3.3). Apparent inconsistencies among them are reconciled through the consideration of the semidiurnal Reynolds stress (section 4.3.4). We then discuss the near-bottom cross-shore momentum and buoyancy budgets (section 4.4) and summarize our main findings (section 4.5). The appendix describe a simple diagnostic model for diagnosing peaks in the observed profile of stratification.

4.2 Methods

4.2.1 Study site and measurements

The main T-TIDE observations were taken between January and March of 2015. We focused our measurements in two regions to capture the transformation of the incident internal tide over continental slopes with distinct shapes. Further north, the shape of the continental slope leads to significant scattering of the incoming low-mode internal tide to

higher modes [Johnston et al., 2015, Klymak et al., 2016]. Further south, the continental slope is steeper and leads to large reflection of the incoming mode-1 wave without significant scattering [Johnston et al., 2015, Klymak et al., 2016, Zhao et al., 2018, Marques et al., 2021]. In this paper, we revisit the in-situ observations further south to examine the effect of the corrugated topography on the tidal and subtidal flow (Fig. 4.1b).

The continental slope around the moorings is steep to the semidiurnal internal tide as defined by the bottom criticality parameter, i.e.

$$\gamma \equiv \frac{|\beta|}{s} = |\beta| \sqrt{\frac{N^2 - \omega^2}{\omega^2 - f^2}}. \tag{4.1}$$

$|\beta|$ is the magnitude of the bottom slope, s is the slope of internal tide characteristics, N is the buoyancy frequency at the bottom, f is the Coriolis parameter, and ω is the frequency of the internal tide (where γ in Fig. 4.1b is for the lunar semidiurnal frequency, $\omega \approx 1.93$ cycles per day). For $\gamma > 1$ (i.e. supercritical), an incident energy flux from the deep ocean reflects backwards (i.e. the cross-shore component of energy flux changes sign). For $\gamma < 1$ (i.e. subcritical), an incident wave shoals onto the bathymetry and keeps propagating shoreward. For $\gamma \approx 1$ (i.e. near critical), the waves reflected off the slope have significantly larger wavenumber than the incident wave [Phillips, 1966].

On a larger scale, the continental slope in southeastern Tasmania is steep and has a concave shape that leads to large reflection. However, over short $O(1)$ km horizontal scales, the topography is corrugated (Fig. 4.1b). Sets of corrugations or isolated canyons are present along a ~70 km stretch of the continental slope. Around the moorings site, the corrugations extend between the 800 and 1500 m isobaths, where the height of the corrugation rim, relative to the seafloor along the trough axis, can be up to 200 m. At the T5 and T6 mooring sites, this height is about 100 and 170 m, respectively. Moreover, other sets of corrugations and canyons are also present at deeper water, between 2000 and 3200 m.

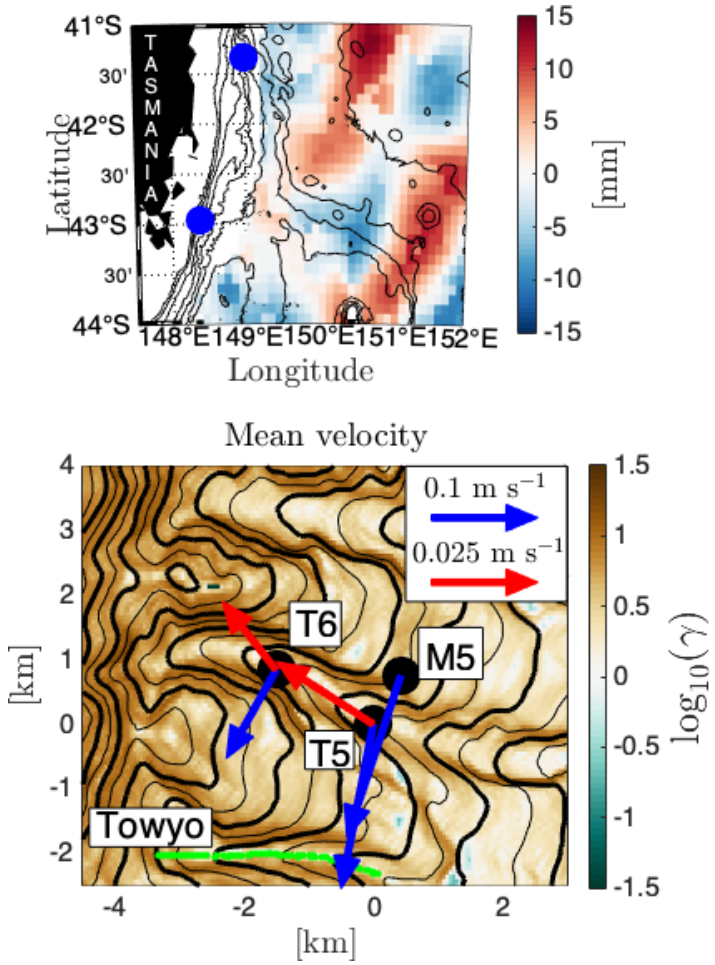

Figure 4.1: Location of TTIDE observations on the continental slope of Tasmania. (a) In-phase, semidiurnal (M2) sea-surface height from satellite altimetry. (b) Location of moorings and CTD-LADCP towyo in the corrugated southeastern continental slope. Time-mean, depth-averaged velocities further above the bottom (blue arrows) are alongshore and poleward. Time-mean velocity within the trough are onshore (red arrows). Note the different scales of the velocity vectors. The bottom slope along the axis of the corrugation is $\beta \approx 0.06$, which implies a vertical velocity $w \sim \beta u \approx 0.06 \times 0.02 \sim O(100)$ m day^{-1}.

With the corrugated topography, the bottom slope has significant variability in the alongshore direction. While the corrugation trough axis has $\gamma \approx 1.5$ and bottom slope of 0.06 (corresponding to an angle of 3°), the walls of the trough have γ between 3 and 10 (with maximum topographic angle of 23°).

We deployed two moorings (T5 and T6) along a trough of the corrugation and one near the edge of the adjacent crest (M5) (Fig. 4.1b). Instrumentation on M5 covers most of the water column, primarily with an acoustic doppler current profiler (ADCP) in the top 100 m, a moored McLane profiler (MMP) between 100 and 800 m, and a second profiler between 820 and 1130 m. Both MMPs had CTDs and velocity sensors, although technical issues led to data gaps between 600 and 800 m in the upper MMP upcasts. In contrast, moorings T5 and T6 extend to about 600 m from the bottom. In each of these moorings, velocity was measured by two Teledyne RD Instruments (TRDI): one 300 kHz ADCP for the bottom 100 m and a 75 kHz ADCP for the overlying 500 m. Around 40 Seabird (SBE)-56 thermistors and two SBE-37 MicroCAT CTDs were deployed over the full mooring length. Thermistors are closer together (10 m) in the bottom 150 m and further apart higher up on the mooring. Further details on the mooring instrumentation can be found in [Marques et al., 2021].

We also carried out a ≈12-hour towyo along the corrugation trough adjacent to the one where the moorings were deployed (Fig. 4.1b). The ship's CTD rosette was instrumented with downward and upward looking lowered acoustic Doppler current profilers (LADCPs), operating at 300 kHz. CTD profiles extend from a depth of 600 m down to 10 m above the bottom. We obtained 3.5 transects along the towyo track, where each full transect took between 2.5 and 3.5 hours.

Throughout this paper, we refer to cross-shore (x) and alongshore directions (y), although their definition depends on the specific context. More precisely, in Figs. 4.2, 4.3, 4.7, and 4.9, it is more appropriate (for display purposes) to first define the alongshore direction in terms of the principal axis of the vertically averaged velocity above the corrugation rim. The cross-shore is the

perpendicular direction in the sense of a right-handed coordinate system. In Figs. 4.6, 4.8, and 4.10, where the near-bottom velocity is the focus of the corresponding analyses, we first defined the cross-shore direction based on the axis of the corrugation trough. In Fig. 4.5, where both coordinate systems are convenient for display purposes, the first definition is used in panels (a)-(d) and the second definition in panel (i).

4.2.2 Dissipation rate estimates

We estimate the rate of dissipation of turbulent kinetic energy (ϵ) from both shipboard and moored instruments. For profiling CTD data (i.e. from the towyo or on the MacLane moored profilers), we use traditional Thorpe scales [Thorpe, 1977, Gargett and Garner, 2008]. Briefly, observed potential density profiles are vertically sorted such that it monotonically increases downwards. For each identified overturn, the Thorpe scale (L_T) is the root mean square displacement between observed and sorted depths. For each overturn, the dissipation rate is computed as

$$\epsilon = \alpha^2 L_T^2 N^3, \tag{4.2}$$

where α is the ratio between the Ozmidov and Thorpe scales and we use constant $\alpha = 0.8$ [Dillon, 1982].

For moored thermistor data, we estimate ϵ as in (4.2), but using the Ellison scale (L_E) instead of the Thorpe scale in (4.2) [Cimatoribus et al., 2014]. The Ellison scale is defined as

$$L_E \equiv \frac{\sqrt{\langle T'^2 \rangle}}{\partial \langle T \rangle / \partial z}, \tag{4.3}$$

where the angle brackets is a time averaging operator and $T' \equiv T - \langle T \rangle$. In practice, our thermistors sample at 1 Hz, with a response time scale of 10 seconds, and we used a time-averaging window of 2 minutes. We also sorted the averaged temperature profile into a stable one before computing the vertical gradient in (4.3) (this approach is often applied to Thorpe scale analysis, although

other definitions of the background stratification have been proposed [Smith, 2020]). For the analyses in this paper, L_E provides an advantage over L_T because average ϵ has a significant contribution from overturns with heights shorter than the near-bottom thermistor spacing (10 m) (see section 4.34.3.3),

4.3 Results

4.3.1 Overview of the observations

Consistent with the time-mean circulation of the East Australian Current Extension (e.g. [Oke et al., 2019]), observed depth-averaged currents are generally poleward throughout the 50-day timeseries. Current speeds are as large as >0.4 m s^{-1}, which can lead to significant mooring knockdown and disrupt the profiling of the MMPs. While the flow is consistently southward further above the bottom, moorings deployed along the corrugation trough show near-zero alongshore velocities below depths around the corrugation rim.

With a weak subtidal cross-shore flow, the semidiurnal velocities become more apparent closer to the bottom. In particular, the amplitude of the semidiurnal cross-shore velocity increases below the corrugation rim (i.e. below the dashed lines in Fig. 4.2 d, e). The semidiurnal tides show a spring-neap modulation, which is a non-trivial result for a remote internal tide (e.g. [Alford and Zhao, 2007a]), and is described in more detail by [Marques et al., 2021].

While subtidal cross-shore velocities are only $O(10^{-2})$ m s^{-1}, they exhibit consistent patterns below the corrugation rim. Moorings T5 and T6 show persistent onshore subtidal near-bottom flow, with similar temporal variability at the two locations. In contrast, the subtidal current on mooring M5 is offshore in the bottom few hundred meters.

Time-mean velocity profiles show the general features of the subtidal flow further above the bottom and below the corrugation rim 4.3). The mean alongshore velocity transitions from weak vertical shear in the interior to enhanced shear within $\approx$ 150 m above the corrugation rim.

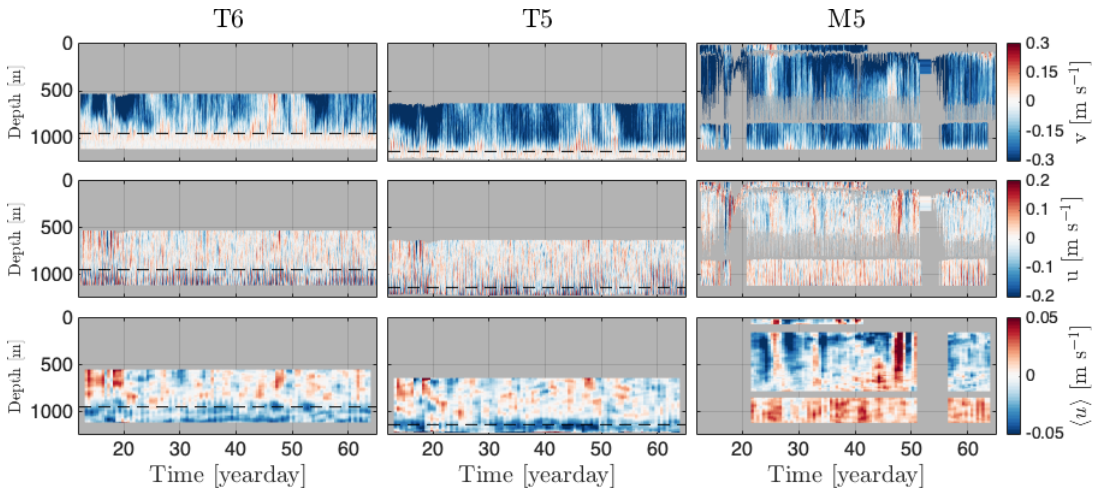

Figure 4.2: Observed velocity at the moorings. (a)-(c) Observed alongshore velocity component; (d)-(f) observed cross-shore velocity; (g)-(i) subtidal cross-shore velocity. Dashed lines for moorings T6 and T5 indicate the rim of the corrugations at these sites. The along-slope velocity decreases within 100 m of the corrugation rim and is very weak within the trough. A relatively weak, but persistently onshore flow is observed within the trough of the corrugations. Upstream from moorings T5 and T6, the flow in the bottom few hundred meters has an offshore component (at mooring M5).

The time-mean onshore flow increases towards the corrugation rim, where the velocity vertical profile has a local maximum. At T5, the cross-shore velocity magnitude decreases monotonically within the bottom ≈70 m, but the onshore velocity at T6 has two local maxima in the vertical. Nevertheless, the observed mean near-bottom velocity is primarily aligned along the corrugation trough (Fig. 4.1b).

As expected, the vertical structure of the mean alongshore current away from the bottom is roughly in thermal wind balance (Fig. 4.3c). We computed the cross-shore density gradient from the moored thermistors and inferred alongshore vertical shear from the thermal wind relation (e.g. [Gill, 1982]). The observed cross-slope density difference (and the associated thermal-wind shear) corresponds to density surfaces tilting upwards in the onshore direction.

The thermal wind shear diverges from the observed shear at depths around and below the shallowest rim depth. Therefore, as expected, the cross-shore geostrophic balance does not hold closer (within ∼100 m) to the bottom. Note that depth levels within the trough at the onshore

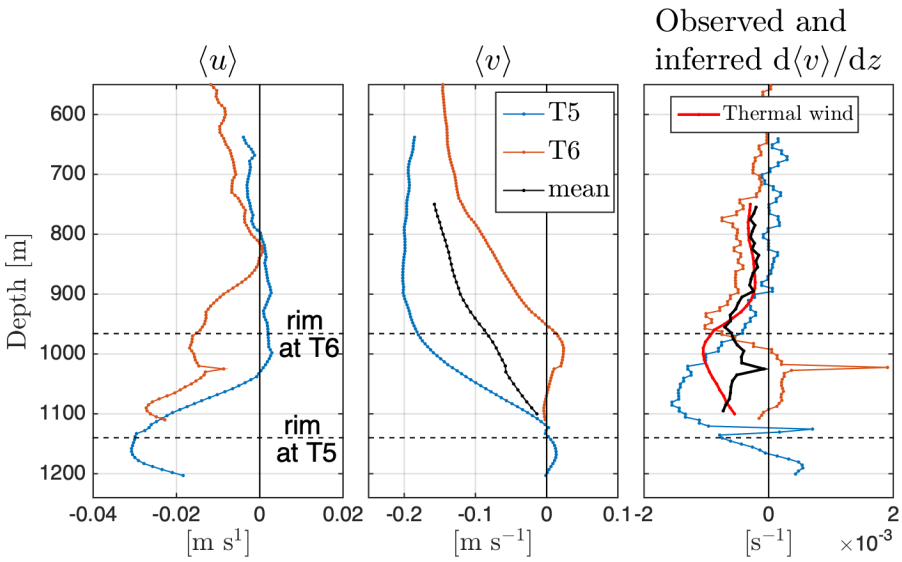

Figure 4.3: Vertical structure of the temporally averaged flow (a) Cross-shore velocity ($\langle u \rangle$), (b) along-shore velocity ($\langle v \rangle$), and (c) vertical shear of $\langle v \rangle$. The thermal wind shear is calculated from horizontal density gradients inferred from thermistor data on moorings T5 and T6. Within 100-200 m above the corrugation rim, the magnitude of $\langle v \rangle$ decreases downwards and is close to zero around the depths of rim. Over the same region, $\langle u \rangle$ increases in the onshore direction. Density surfaces tilt upwards in the onshore direction and are consistent with thermal wind above ≈980 m. At depths below the corrugation rim at the onshore mooring site, the observed and predicted vertical shear diverge. At mooring T5, the onshore velocity has a simpler vertical structure, with maximum around the rim of the corrugation. While the vertical structure at mooring T6 is more complex, the mean velocity is also onshore.

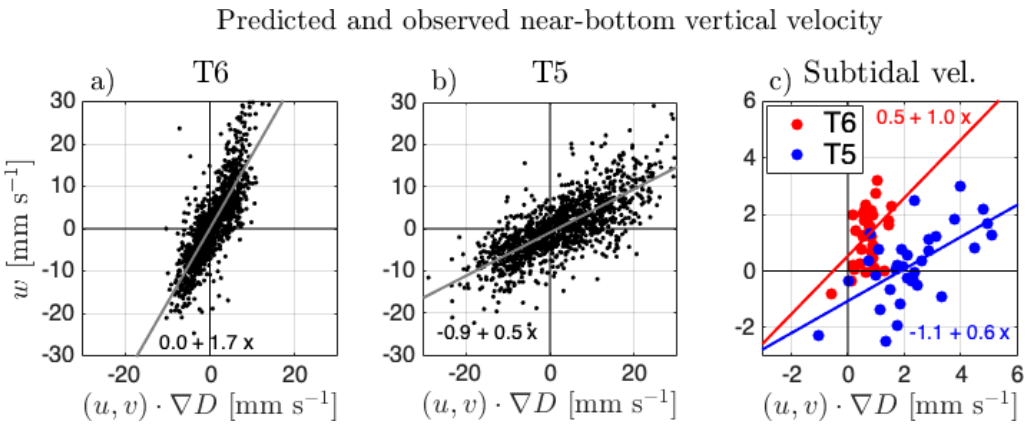

Figure 4.4: Direct and indirect vertical velocities from (a) velocity observations at T6, (b) at T5, and (c) from the corresponding subtidal velocities. The lines correspond to the linear regression and the regression coefficients are shown next to them. In (c), the regression curves are computed from the T6 (red) and T5 (blue) data separately. Direct vertical velocities refer to the ADCP measurements of w and indirect estimates are computed from the horizontal velocity and the bottom slope (i.e. through equation (4.4)). Note the limits of the x and y axes in (c) are one order of magnitude smaller than in (a) and (b). Biases of 1° in tilt and roll sensors are sufficient to change the sign of a 1 mm s^{-1} vertical velocity.

mooring site (T6) lie above the corrugation rim at the offshore mooring location (T5). Our observations can only evaluate the mismatch between observed and predicted shears between the mooring sites, but thermal wind might still hold above the corrugation rim at mooring T5.

4.3.2 Near-bottom vertical velocity

The observed onshore velocities within the corrugation indicate upwelling along the sloping bottom. In this paper, we use upwelling to refer to positive vertical velocity, irrespective of the components of the flow that are across or along density surfaces.

In principle, ADCPs provide all three components of the velocity field. In practice, several factors preclude an accurate measurement of the vertical velocity (w) in the deep ocean. First, horizontal homogeneity of the flow must be assumed to combine the along-beam velocities from the ADCP. Second, since the horizontal velocity is much larger than the vertical component, the orientation of the ADCP must be known to high accuracy for an unbiased estimate of w. The required accuracy for reliable direct w measurements can be estimated by doing a simple

sensitivity analysis where we reprocess the raw data after adding known biases to the tilt and roll sensors. This calculation shows that a bias of 1° in the attitude sensors changes the vertical velocity by about 1 mm s^{-1}.

Alternatively, w can be indirectly estimated from the horizontal velocity by assuming the bottom boundary condition of no flow through the bottom applies to the velocity measurements. This condition implies the velocity is parallel to the topography and can be written as

$$w = (u, v) \cdot \nabla_{x,y} D, \tag{4.4}$$

where $\nabla_{x,y}$ is the two-dimensional (horizontal) gradient operator, (u, v) is the horizontal velocity in the (x, y) coordinate system, and D is (minus) the water depth. For an order of magnitude estimate, it is useful to rotate (4.4) in a coordinate system aligned with the axis of the corrugation trough. With the bottom slope along the axis $\beta \approx -0.06$ and an along-corrugation subtidal velocity of -0.01 m s^{-1} (Fig. 4.3a), we infer

$$w = \beta u = 0.6 \text{ mm s}^{-1} \approx 50 \text{ m day}^{-1} \tag{4.5}$$

As an attempt to support (4.5), we compared direct and indirect estimates of near-bottom w. For the *total* velocity signal, there is good agreement between direct and indirect w (Fig. 4.4 a, b). The vertical velocitiy is primarily associated with the semidiurnal tide flowing along the corrugation trough, which leads to positive and negative $w \sim O(10^{-2})$ m s^{-1}. Squared correlation coefficients are $r^2 = 0.5$ and $r^2 = 0.7$ for moorings T5 and T6, respectively. However, regression slopes are not one. Nevertheless, the practical limitations of computing w with our ADCP are not too severe for reasonably measuring $w \sim O(10)^{-2}$ m s^{-1}.

Although our direct measurements are not sufficient to attest *subtidal* w of $O(10^{-3})$ m s^{-1}, they are also not inconsistent with it (Fig. 4.4). In particular, observations at the T5 mooring are correlated ($r^2 = 0.4$) and the regression coefficients computed from the subtidal velocity are

similar to those from the total velocity (Fig. 4.4b, c). Moreover, the y-intercept of the regression analysis from the T5 mooring data suggests a bias in w of 1 mm s^{-1}. Based on our sensitivity analysis, a bias of 1° in the attitude sensors may lead to a 1 mm s^{-1} bias in the direct vertical velocity measurement.

Although the direct subtidal w at mooring T6 also indicates large upwelling, the statistics do not support its accuracy as much as for the T5 mooring data. The correlation between direct and indirect subtidal estimates is smaller ($r^2 = 0.2$) at mooring T6. In contrast with data from the T5 mooring, the regression coefficients from total and subtidal velocity signals are not consistent between each other. It is unclear whether there are issues with the ADCP or the boundary condition (4.4) is not appropriate for the depth range where we have available observations.

In the context of global abyssal mixing, estimate (4.5) is a large upwelling velocity. [Munk, 1966] obtained a globally averaged diapycnal upwelling of $\sim 10^{-2}$ m day^{-1}, which is consistent with a recent analysis of an ocean state estimate [Liang et al., 2017]. Diapycnal velocity in regional contexts are larger than global averages, but generally smaller than (4.5) estimates of: $w \sim 1$ m day^{-1} have been computed within both coastal [Kunze et al., 2012] and abyssal [Thurnherr et al., 2020] canyons; $w \sim O(1-10)$ m day^{-1} was inferred for boundary mixing in a deep western boundary current north of the Weddell Sea [Spingys et al., 2021]; and $w \sim O(10)$ m day^{-1} was computed from a volume budget in the Samoan Passage [Voet et al., 2015]. Finally, we highlight once again that our direct and indirect upwelling velocities are defined as being along the vertical direction, and not necessarily perpendicular to density surfaces (this distinction is further explored in the discussion of the buoyancy balance, section 4.4.2).

4.3.3 Near-bottom turbulence

In addition to the persistent onshore flow, enhanced dissipation rate is also associated with the corrugation trough (Fig. 4.5). The average vertical profile of ϵ is relatively constant within the corrugation trough and, above the rim, ϵ decreases with increasing height above the bottom.

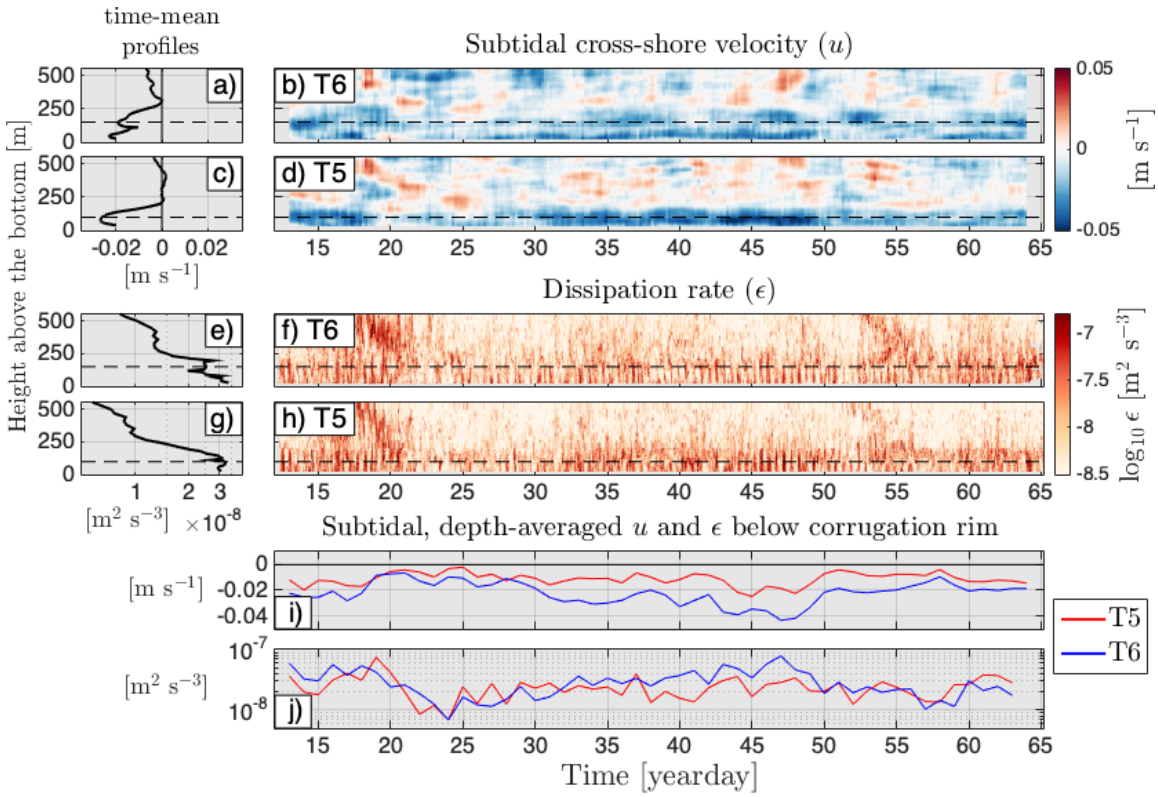

Figure 4.5: Time mean and variability of subtidal cross-shore velocity (u) and dissipation rate (ϵ) over the corrugation trough. Cross-shore velocity and dissipation rate are generally enhanced around and beneath the corrugation rim depth at each mooring site (between 100 and 200 m from the bottom). In this bottom layer, average ϵ is $2-3\times10^{-8}$ m^2 s^{-3}. Large dissipation rates higher above the bottom are observed when the alongshore velocity is large (> 0.3 m s^{-1}, see Fig. 4.2). Periods of both large u and ϵ within the bottom 100 m are observed before yearday 20 and between yeardays 30 and 50.

Large ϵ is also observed away from the bottom at times when the alongshore current is strong.

Within the corrugation trough, time-mean $\epsilon \approx$ 2-3 $\times10^{-8}$ m^2 s^{-3}. The average near-bottom ϵ from Thorpe scale analysis applied to the mooring data is a factor of 5 smaller. Therefore, density overturns shorter than 10 m in the vertical, which are not resolved by our moored thermistors, have a significant contribution to the average ϵ. Above 200 m from the bottom, where thermistor spacing increases to 20-30 m and ϵ is smaller than near the bottom, density inversions are rarely observed and only the Ellison scale can provide an estimate of ϵ. Over short time scales (i.e. $\approx$ 1 hour), enhanced ϵ is often associated with overturns higher than 50 m and $\epsilon \approx 10^{-7}$ m^2 s^{-3}.

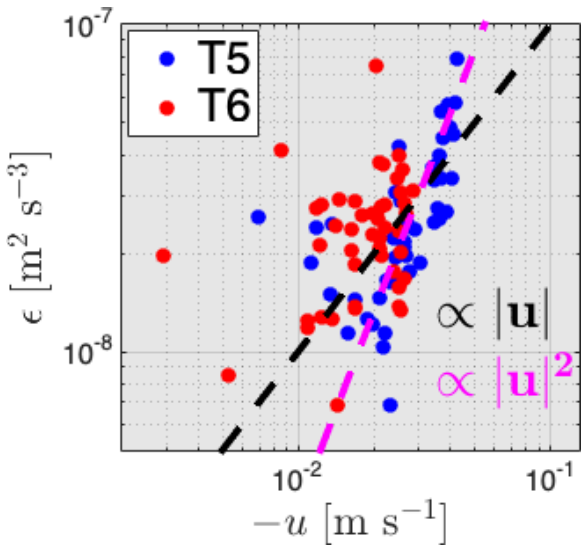

Figure 4.6: Near-bottom turbulence is proportional to onshore subtidal velocity inside the corrugation trough. Consistent with the height scale of dissipation rate (see Fig. 4.5), ϵ on the mooring outside the corrugation (M5) has good correspondence with the other two moorings (T5 and T6). The correlation between u and $\log_{10}(\epsilon)$ is larger at T5 ($r^2 \approx 0.5$) than at T6 ($r^2 \approx 0.2$). The linear relationships between $|u|$ and ϵ are shown for reference, but we have not made dynamical interpretations based on (uncertain) regression slopes. Nevertheless, larger onshore velocity is associated with larger near-bottom turbulence.

At subtidal time scales, near-bottom turbulence is similar across all moorings and is proportional to the cross-shore subtidal velocity (Fig. 4.5). While semidiurnal velocity and vertical displacements have well-defined spring-neap cycle [Marques et al., 2021], near-bottom ϵ and background cross-shore velocity do not. Velocity and near-bottom turbulence are larger earlier in the record, followed by a sharp decrease around yearday 20. Their magnitudes increase between yearday 25 and 47, and decrease to more moderate values until the end of the timeseries. Despite the temporal variability, note that the range in subtidal ϵ is only one order of magnitude.

In addition to the relationship between subtidal velocity and ϵ, dissipation rate is also modulated over semidiurnal time scales (Fig. 4.7). Over three days (around the period when towyo data is also available), the amplitude of the semidiurnal ϵ has significant variability without a clear correspondence to tidal velocity. For example, only a modest tidal cycle in ϵ is observed between yeardays 31.5 and 33, but the semidiurnal signal is larger in the preceding and subsequent tidal

periods. Nevertheless, below the corrugation rim, dissipation rate is enhanced in the transition between offshore and onshore tidal velocities. Higher above the bottom, enhanced dissipation might be linked to alongshore tidal velocities, where the diurnal tide may also play a role (i.e. above 900 m, ϵ is enhanced around yeardays 31.5, 32.5, and 33.5).

From the combined towyo and mooring observations, the near-bottom turbulence can be understood in terms of the sloshing of the internal tide. First, cross-shore tidal velocities are enhanced within the trough of the corrugation. This spatial structure leads to larger vertical displacements and tilt of density surfaces. Onshore tidal flow tilts density surfaces, such that they become nearly parallel to the ocean bottom. With offshore advection, the density surfaces tilt in the opposite direction, stratification decreases, triggering large overturns through convective instabilities. Onshore velocities then advect water upslope and restratify the layer below the corrugation rim layer.

The observed near-bottom turbulence and cross-shore velocities lead to an apparent contradiction. On one hand, the observations support a correlation between ϵ and the cross-shore velocity within the corrugation (Fig. 4.6), and they do not exhibit a clear fortnight modulation (Fig. 4.5). On the other hand, the semidiurnal tide, which has a well-defined spring-neap cycle [Marques et al., 2021], seems to be a significant source of near-bottom turbulence (Fig. 4.7). These observations may be reconciled by considering the subtidal flow forced by the internal tide.

4.3.4 Internal tide forcing of subtidal flow

In a rotating system, internal waves can accelerate the background horizontal flow through the divergence of the pseudomomentum flux

$$\mathbf{F} \equiv \left(u'w' - \frac{f}{N^2} v'b', \;\; v'w' + \frac{f}{N^2} u'b', \;\; 0 \right), \tag{4.6}$$

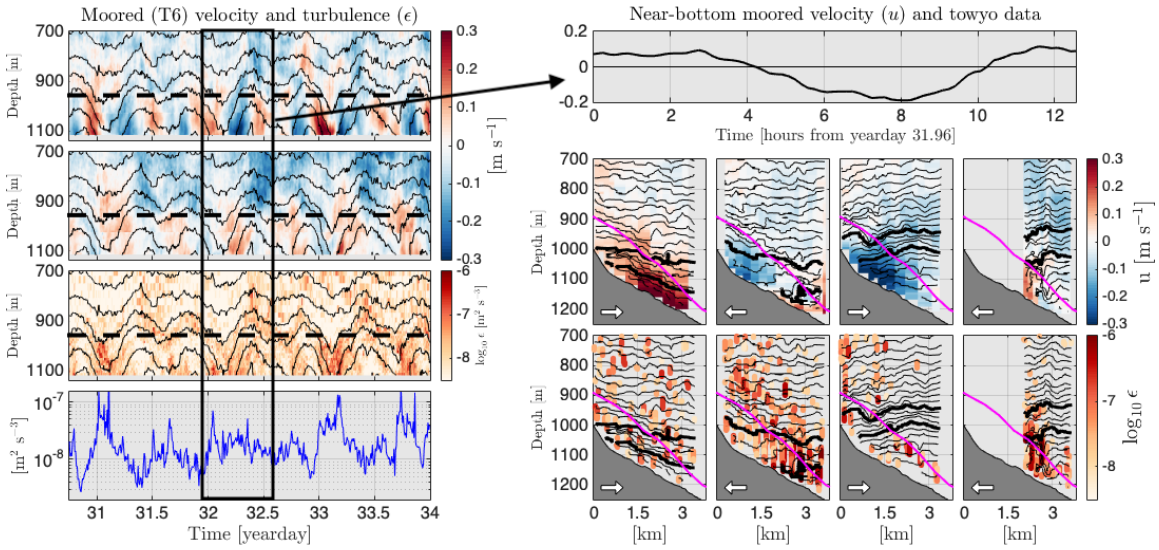

Figure 4.7: Near-bottom velocity and turbulence observations from moored and shipboard data. 3-day mooring record (T6) of (a) cross-shore velocity, (b) along-shore velocity, (c) dissipation rate (ϵ), and (d) depth-averaged ϵ. (f)-(i) Cross-shore velocity and (j)-(m) ϵ from a cross-shore CTD-LADCP towyo along the corrugation trough adjacent to the one the moorings were deployed. (e) Near-bottom cross-shore moored concurrent to the towyo observations. The horizontal dashed lines in (a)-(c) indicate the corrugation rim depth. In (f)-(m), the white arrows indicate the direction of the ship track for each transect, and the magenta line is the corrugation rim depth. Dissipation further above the bottom may be associated with along-slope flow above the corrugation rim. Cross-shore tidal velocities are enhanced within the trough. Enhanced turbulence takes place between the peak onshore and offshore tidal velocities.

where (u', v', w') is a wave component of the velocity vector, and b' is the buoyancy perturbation due to wave field [Gent and McWilliams, 1996, Shakespeare and Hogg, 2019]. The corresponding acceleration (wave forcing, WF) is given by

$$WF \equiv -\frac{\partial \langle \mathbf{F} \rangle}{\partial z}, \tag{4.7}$$

where the angle brackets correspond to space-time averaging. Note that (4.6) is a simplified version of the generalized pseudomomentum flux and its validity depends on a suitable definition of the averaging operator in (4.7) [Gent and McWilliams, 1996].

If we assume the averaging operator can be substituted by averaging in time only, then our moorings can provide an estimate of (4.7). Semidiurnal u' and v' (cross-shore and along-shore, respectively) were computed from the ADCP data. Similarly, we computed the semidiurnal buoyancy anomaly (b') from timeseries of potential density, inferred from the thermistors. Without reliable direct measurements of w' throughout the whole mooring depth range, we first computed semidiurnal vertical displacements, and then estimated w' as the time derivative of displacement. Our averaging operator is a simple daily average of second-order quantities (e.g. $u'w'$).

As expected, the cross-shore component of $\mathbf{F}$ is generally enhanced below the corrugation rim (Fig. 4.8). Since the tidal ellipses are largely polarized along the corrugation trough, the rotational term is much smaller than the momentum stress term in the bottom layer. Therefore, the relevant pseudomomentum reduces to the $\langle u'w' \rangle$ term, which is one of the components of the semidiurnal Reynolds stress tensor.

The wave forcing term is also enhanced near the bottom and is generally onshore (Fig. 4.8 g, h). Vertical gradients are much smaller higher above the bottom than below the corrugation rim. Observations at the two moorings have different vertical structures in the bottom layer. At mooring T6, WF is onshore around the corrugation rim, but is generally offshore closer to the bottom. In contrast, mooring T5 is consistently onshore below the rim. Moreover, WF only

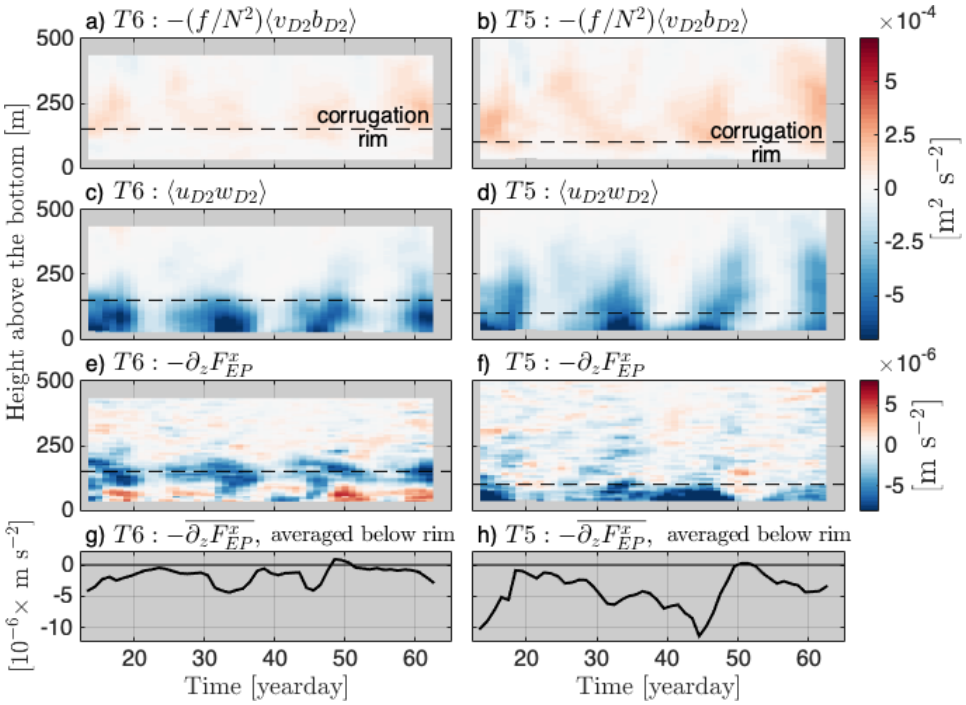

Figure 4.8: Semidiurnal wave pseudomomentum and its vertical gradient for moorings T5 an T6. The Reynolds stress term is much larger than the buoyancy term (not shown). The semidiurnal stress is primarily enhanced below the rim of the corrugation. The semidiurnal stress averaged below the rim is primarily associated with onshore acceleration

has a clear spring-neap cycle around the corrugation rim at T6. Despite differences between moorings, the acceleration averaged below the rim of the corrugation is generally onshore for the two moorings and has a magnitude between 10^{-6} and 10^{-5} m s^{-2}. Qualitatively, this onshore acceleration may play a role in sustaining the cross-shore subtidal flow, but other terms in the cross-shore momentum equation must be taken into account.

4.4 Discussion

4.4.1 Momentum balance

To address whether wave forcing is a reasonable hypothesis, we consider the cross-shore momentum equation at subtidal timescales

$$\frac{\partial\langle u\rangle}{\partial t} + \langle u\rangle\frac{\partial\langle u\rangle}{\partial x} - f\langle v\rangle = -\frac{1}{\rho_0}\frac{\partial\langle p\rangle}{\partial x} + WF + \frac{\partial}{\partial z}\left(A_v\frac{\partial\langle u\rangle}{\partial z}\right), \tag{4.8}$$

where variables in angle brackets denote time averaging, WF is the wave forcing term defined in (4.7), and A_v is a turbulent vertical kinematic viscosity. Equation (4.8) only includes terms that we can estimate from the observations and we will consider the momentum equation for depth averaged below the corrugation rim.

From order of magnitude estimates, several terms in (4.8) are smaller than the near-bottom wave forcing term previously computed (Fig. 4.8). From Fig. 4.5, the unsteady term is $O(10^{-8})$ m s^{-2}. Taking $\langle u\rangle \sim 10^{-2}$ m s^{-1} and a corrugation length of 5 km, the nonlinear term on the left-hand side of (4.8) is also $O(10^{-8})$ m s^{-2}. The frictional term averaged within the corrugation trough, can be decomposed as a stress at the rim minus at the bottom. The mean velocity shows a near-zero gradient at the top of the corrugation (Fig. 4.3). The magnitude of the bottom drag can be parameterized as $C_d|u|^2/H$, where $C_d = 2\times10^{-3}$ is a drag coefficient [Polzin and McDougall, 2021] and H is the height above the bottom of the corrugation rim. Using

$H = 100$ m, the magnitude of the bottom drag is $O(10^{-8})$ m s^{-2}.

Since we did not measure pressure at the bottom, we can only infer the the cross-shore pressure gradient. Our approach is to estimate $\partial_x p$ from the along-shore velocity away from the bottom and the density difference between moorings T5 and T6. The pressure gradient term in (4.8) can be rewritten as

$$-\frac{1}{\rho_0}\frac{\partial\langle p\rangle}{\partial x} = -\frac{g}{\rho_0}\frac{\partial}{\partial x}\int_z^{z_0}\langle\sigma\rangle\,\mathrm{d}z' - \frac{1}{\rho_0}\frac{\partial\langle p\rangle}{\partial x}\bigg|_{z_0}, \tag{4.9}$$

where σ is potential density and z_0 is a reference depth. By assuming a geostrophic balance in the cross-shore direction at a depth z_0 further away from the bottom, we can infer the pressure gradient from the velocity measurements at the reference depth (which we chose as $z_0 = 640$ m). The baroclinic term (first term on the right-hand side of (4.9)) can be readily computed over the depth range where observations at both moorings are available.

While the poleward velocities away from the bottom are associated with an onshore pressure gradient acceleration, the tilt in density surfaces is sufficiently large to reverse the direction within the corrugation trough (Fig. 4.9). The onshore pressure gradient within ≈ 100 m above the corrugation rim could be associated with the onshore velocities in the same depth range, but it is inconsistent with the onshore velocities observed below (Fig. 4.3). Therefore, the near-bottom upwelling in our observations is fundamentally different than pressure-driven upwelling suggested for narrow canyons [Allen and Hickey, 2010, Alford and MacCready, 2014]. Instead, the onshore flow is likely driven by the remote internal tide over the sloping bottom, which is suggested by the correlation ($r^2 = 0.4$) between the cross-shore subtidal flow and the wave-driven acceleration.

Although we could not close the cross-shore momentum budget within the corrugation trough, the pressure gradient and wave forcing terms have the largest magnitudes (Fig. 4.10). These terms have opposite signs, but the pressure gradient is 2 to 3 times larger. There are several

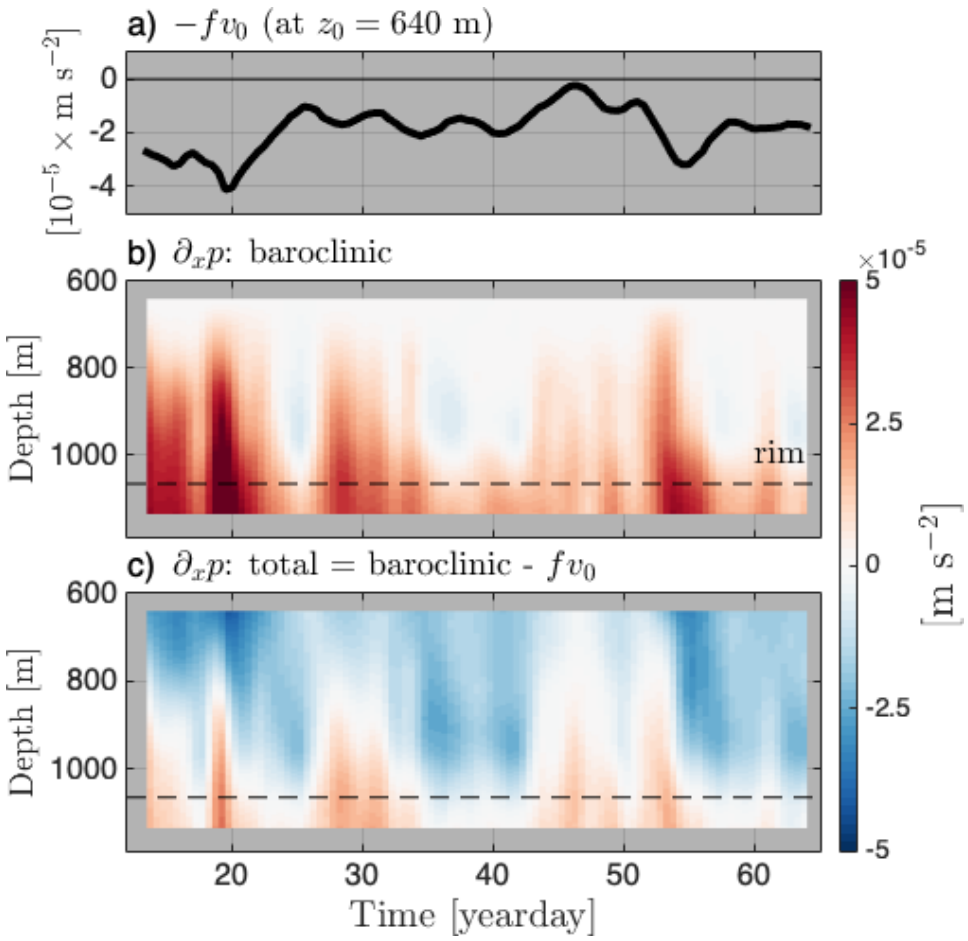

Figure 4.9: Cross-shore pressure gradient estimate. (a) Pressure gradient at z_0 assuming geostrophic balance, (b) baroclinic pressure gradient term (first term in the right-hand side of (4.9), and (c) the total pressure gradient. The bottom and rim depth are taken at the location between moorings T5 and T6. Contrary to near-bottom upwelling driven by the cross-shore pressure gradient, the near-bottom acceleration is offshore.

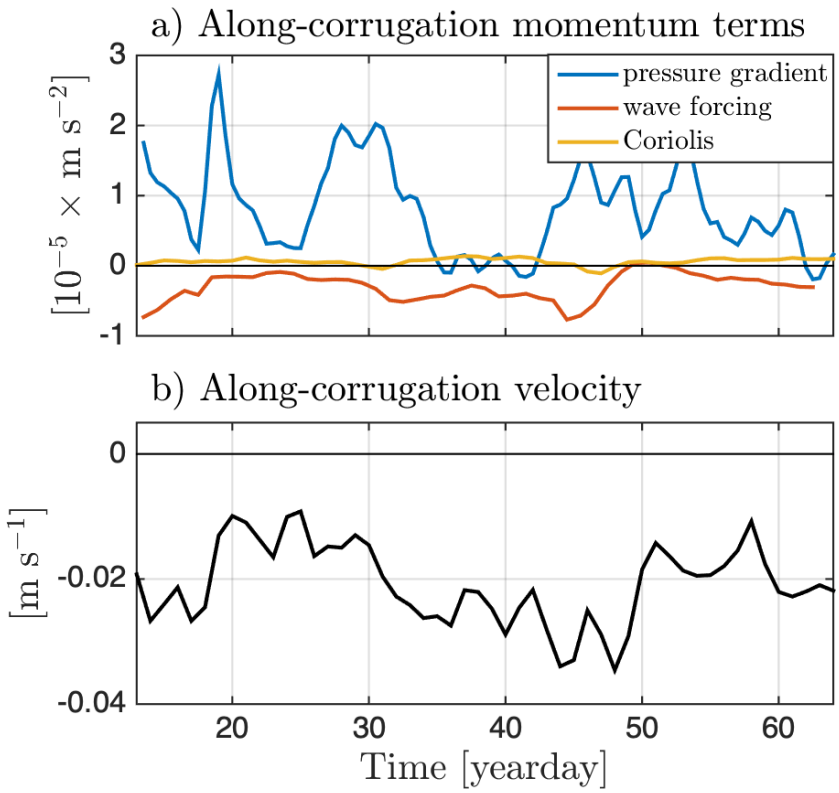

Figure 4.10: Along-corrugation momentum budget vertically averaged within the corrugation trough. (a) Timeseries of along-corrugation pressure gradient (blue line), wave-forcing acceleration (red line), and along-corrugation Coriolis acceleration. (b) Along-corrugation subtidal velocity (note the observed acceleration is $O(10^{-8})$ m s^{-2}). The wave forcing and Coriolis terms are computed as means of the depth-averaged quantities calculated at each mooring. Depth-averages were computed from the rim depth to the bottom. In (a), the Coriolis terms has the smallest magnitude and estimates of bottom drag and nonlinear terms (see text) are even smaller. Although we can not close the along-corrugation momentum budget, the pressure gradient and the wave forcing terms are consistently offshore and onshore, respectively.

limitations in the estimates that could explain the differences. For example, these terms have gaps in the bottom $\leq$ 50 m. Moreover, the pressure gradient was computed between the moorings, while the wave forcing term is an average of the depth-averaged WF separately computed at each mooring. Finally, differences in the wave forcing term between the moorings suggests cross-shore variability that is hard to account for with observations at only two sites.

Despite the limitations of our measurements, we propose that the effect of small-scale corrugations on the incoming internal tide, couples the latter with dynamics of the subtidal flow.

Internal tide velocities are enhanced within the corrugation troughs, either through the bathymetric constriction or the dynamics over a near-critical slope along the trough axis ($\gamma \approx 1.5$). The resulting internal-tide Reynolds stress accelerates the near-bottom onshore flow that lifts density towards the shore, which in turn sets a counteracting pressure gradient. The cross-shore density gradient extends higher above the corrugation rim, such that the magnitude of the overlying alongshore current decreases towards the rim through thermal-wind shear. The coupling between different processes also suggests that the temporal variability of the large-scale alongshore current may also modify the semidiurnal and subtidal velocities near the bottom. Nevertheless, the correlation between wave forcing and subtidal velocity indicates that the remote internal tide, and not the alongshore current, forces the observed near-bottom flow.

4.4.2 Buoyancy balance

Our proposed hypothesis for the flow within the corrugated trough has not considered the buoyancy budget. Following [Kunze et al., 2012], the steady buoyancy equation for a thread of fluid that extends across the width of the corrugation trough $l_y(x,z)$ is

$$\overline{u} l_y \overline{B}_x + \overline{w} l_y \overline{N}^2 = -\frac{\partial}{\partial x}\left(\overline{u'b'} l_y\right) - \frac{\partial}{\partial z}\left(\overline{w'b'} l_y\right), \tag{4.10}$$

where the overbar indicates time averaging and the flow is two-dimensional flow (i.e. no alongshore variability). From (4.10), mixing and/or adiabatic flow is required to maintain a mean upslope flow.

Based on [Kunze et al., 2012], we will first make an estimate of the vertical velocity based on a balance between vertical advection and diffusion, i.e.

$$\overline{w} l_y \overline{N}^2 = -\frac{\partial}{\partial z}\left(\overline{w'b'} l_y\right). \tag{4.11}$$

The mean vertical turbulent buoyancy flux is often parameterized as $\overline{w'b'} = -\Gamma\overline{\epsilon}$ [Osborn, 1980], where Γ is the mixing coefficient. As in [Kunze et al., 2012], $\overline{\epsilon}$ is nearly constant within the corrugation trough and would suggest a zero divergence of buoyancy flux. However, mixing can play an integrated role on the buoyancy budget within the trough because l_y decreases below the rim. Assuming l_y decreases linearly with depth, an estimate of the vertical velocity is given by

$$\overline{w} \approx \frac{\Gamma}{\overline{N}^2 H}\overline{\epsilon}, \tag{4.12}$$

where H the height of the corrugation trough and γ is the mixing coefficient [Gregg et al., 2018]. If we take $\Gamma = 0.2$ [Osborn, 1980], $H = 100$ m, $\overline{\epsilon} = 3\times10^{-8}$ m^2 s^{-3} (Fig. 4.5), and $\overline{N}^2 = 10^{-5}$ s^{-2} (Fig. 4.11), we obtain $\overline{w} = 6\times10^{-6}$ m s^{-1} ≈ 0.5 m day^{-1}. Given the assumptions in the parameterization, this estimate of vertical velocity is also a diapycnal velocity.

Our diapycnal velocity estimate has a moderate magnitude when comparable to results from other observationally based studies of diapycnal upwelling over sloping bottoms [Kunze et al., 2012, Voet et al., 2015, Thurnherr et al., 2020, Spingys et al., 2021]. These estimates are at least one order of magnitude larger than the globally averaged rate of abyssal upwelling [Munk, 1966]. We highlight that our measurements (and those of [Kunze et al., 2012]) are not located in the abyssal ocean (i.e. within the depth range of the lower overturning circulation), but there are not enough observations for a more comprehensive comparison between directly comparable studies. In fact, since the large-scale diapycnal diffusivity around ≈ 1000 m is one order of magnitude smaller than in the abyss [Lumpkin and Speer, 2007], our mean diapycnal velocity estimate is at least two orders of magnitude larger than a basin-wide average around the same depth level.

Nevertheless, $\overline{w} \approx 0.5$ m day^{-1} is two orders of magnitude smaller than the vertical velocity we inferred from the horizontal component over the sloping bottom and the direct ADCP measurements (Fig. 4.4). Moreover, the density surfaces tilt upwards in the onshore direction

(Fig. 4.11b), which is associated with some adiabatic upwelling. In a purely adiabatic steady flow, flow is parallel to the density surfaces. Assuming that we can apply the bottom boundary condition (4.4), it implies that the mean density surfaces should also be parallel to the seafloor.

However, the temporally averaged slope of density surfaces is significantly smaller than $|\beta| \approx 0.06$, the bottom slope along the axis of the trough (Fig. 4.11). The maximum mean cross-shore isopycnal slope observed between the moorings is -0.011, 18% of the bottom slope. The peak value has a local maximum at ≈1000 m, just below the rim depth at the onshore mooring, indicating the enhanced isopycnal slope within the trough, relative to the slope in the interior.

Since the observed density surfaces are computed from two locations only, only a mean slope is measured, but not the curvature. Inferred density surfaces from the thermal wind applied at each mooring indicate the slope in the interior between 750 and 900 m is steeper further onshore. Assuming thermal wind is a valid approximation above the corresponding rim depths at each mooring, we can make local estimates of isopycnal slopes. The maximum value, which is still only 25% of the bottom slope, is obtained for the mooring further offshore (T5) at a depth of ≈1080 m.

The vertical structure of stratification suggests strong curvature and steeper density surfaces that is not captured by the direct and indirect observations above (Fig. 4.11). Both moorings show peak of N^2 just above the corresponding rim depths, which is a signature of increased slope of isopycnals around the corrugation rim relative to the interior. A simple geometric model can be constructed to relate the density field to the change of N^2 across the rim, which allows us to infer the isopycnal slope associated with the peak in stratification from a single mooring (Appendix). We estimated that the isopycnal slope can be a substantial fraction (i.e. up to 40%) of the bottom slope. However, notice that our simple model provides only a realistic estimate where the peak in N^2 is observed, but not closer to the bottom.

All of our direct and indirect estimates for the mean slope of density surfaces do not support that the subtidal flow can be purely two-dimensional and adiabatic. Therefore, considering

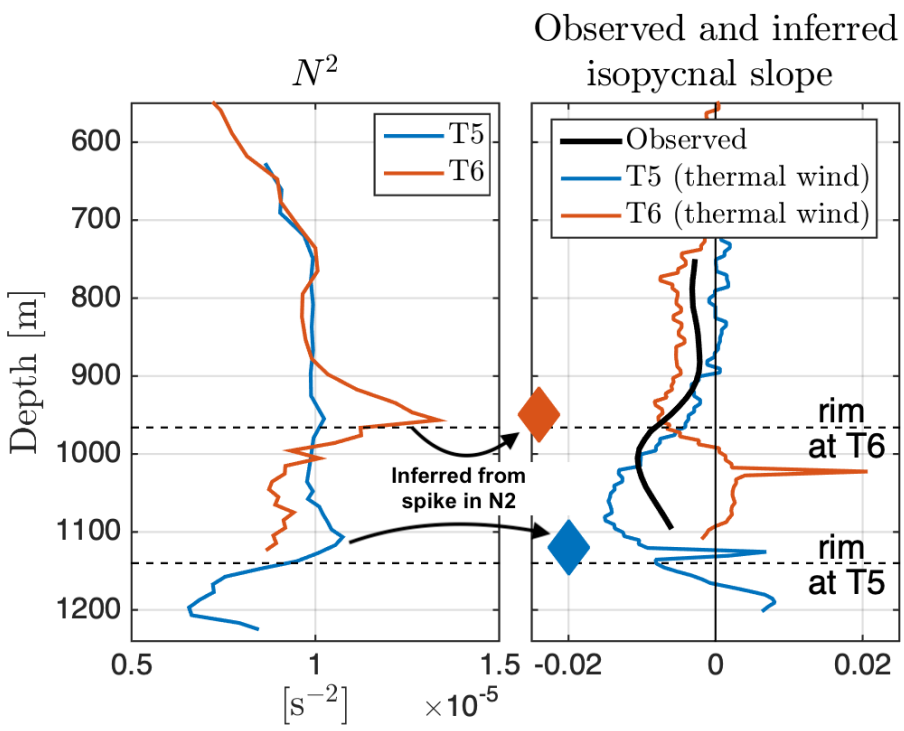

Figure 4.11: Vertical stratification enhancement around corrugation rim and slope of density surfaces. (a) Time-mean buoyancy frequency squared (N^2) from moorings T5 and T6. (b) Observed slope of mean density surfaces (black line), slopes inferred from dv/dz, the thermal wind relation, and N^2 at each mooring separately. Based on a diagnostic cross-shore toy-model of the density field (see Appendix), enhanced N^2 around the rim of the corrugation may be associated with increased tilt of density surfaces (going upwards in the onshore direction). The disparity between observed and inferred slopes may be associated with the curvature of density surfaces around the rim of the corrugations. An isopycnal slope of 0.022 is about 40% of the bottom slope (0.06) along the axis of the corrugation.

both diabatic and adiabatic estimates, we can not close the buoyancy budget. Nevertheless, we also note that even if the isopycnal slope is only 10% of the bottom slope, the adiabatic vertical velocity is an order of magnitude larger than the diapycnal component we estimated from $\overline{\epsilon}$. Other effects that may be important in the buoyancy budget are (i) adiabatic recirculation within the corrugation trough and (ii) Stokes drift due to the internal tide.

4.5 Summary

The remote internal tide impinging on the continental slope off Tasmania undergoes different transformations depending on the region along the slope [Klymak et al., 2016]. Further north, the complex shape of the continental slope significantly scatters the mode-1 wave to higher modes. Further south, the concave, steeper continental slope leads to large mode-1 reflectivity. Since the incident energy flux is variable and mostly directed to the southern region, the overall result of the internal tide is to be primarily reflected as a low-mode wave.

However, our observations indicate that small-scale corrugated topography embedded on the reflective slope modify the internal tide dynamics near the bottom, which fuels the near-bottom turbulence and drives the onshore near-bottom flow. More specifically:

- Persistent onshore flow is observed within the corrugation trough.
- Alongshore subtidal velocities decrease to near-zero values around the corrugation rim through thermal-wind balance.
- Based on direct and indirect vertical velocity estimates, we infer large vertical velocities of up to $O(100)$ m day^{-1}.
- Near-bottom cross-shore velocity and ϵ are correlated and do not exhibit a clear spring-neap cycle.
- Internal tide sloshing is an important mechanism for near-bottom turbulence.
- The divergence of the the semidiurnal Reynolds stress reconciles the temporal variability of the internal tide with the dissipation and the subtidal flow.
- We propose that the near-bottom onshore subtidal current is primarily driven by the remote internal, which is balanced by an opposing pressure gradient, which in turn is coupled with the overlying alongshore current through thermal-wind.

4.6 Appendix: Diagnostic model of peak in N^2

In this simple two-dimensional diagnostic model, we impose a change of isopycnal slope along an interface and relate to the corresponding change in vertical stratification. The bottom topography is an infinite plane and its angle to the horizontal is β. The interface between the boundary and the interior lies at $z = -\tan(\beta)x$ and it has a constant height H above the bottom. In the model, we specify constant horizontal and vertical density gradients in the interior and in the boundary layer. The angle to the horizontal of the density surfaces in the boundary layer are denoted as θ. Contrary to standard trigonometric convention, we use positive angles and tangents for lines inclining downwards as x increases.

By specifying both the constant density gradient in the interior

$$\nabla\sigma^I \equiv \left(\sigma_x^I, \sigma_z^I\right) \equiv \left(M^I, N^I\right), \tag{4.13}$$

and the isopycnal slope in the boundary layer,

$$\tan\theta \equiv \frac{\sigma_x}{\sigma_z} = \frac{M^B}{N^B}, \tag{4.14}$$

we can solve for the density gradient in the boundary layer, i.e.

$$\nabla\sigma^B \equiv \left(\sigma_x^B, \sigma_z^B\right) \equiv \left(M^B, N^B\right). \tag{4.15}$$

The density fields in the interior and in the boundary are given by

$$\sigma^{I,B}(x, y) = \sigma(0, 0) + M^{I,B}x + N^{I,B}z. \tag{4.16}$$

Matching the solutions at the interface $z = -\tan(\beta)x$ yields the relation

$$M^I - \tan(\beta)N^I = M^B - \tan(\beta)N^B. \tag{4.17}$$

Substituting (4.14) into (4.17) gives

$$N^B = \frac{M^I - \tan(\beta)N^I}{\tan(\theta) - \tan(\beta)}. \tag{4.18}$$

We can also denote the slope in the interior by $\tan(\alpha) \equiv M^I/N^I$ and rewrite (4.18) as

$$N^B = N^I \frac{\tan(\beta) - \tan(\alpha)}{\tan(\beta) - \tan(\theta)}. \tag{4.19}$$

The horizontal density gradient in the boundary is then given by $M^B = N^B \tan(\theta)$.

We have tuned the model to separately match the observed peak in N^2 in each mooring. The analysis for T6 is shown in Fig. 4.12. For the slope in the interior, we use the slope inferred from the vertical stratification and the horizontal density gradient based on thermal wind (Figs. 4.11). The value of $\tan(\theta)$ in Fig. 4.12 is the same as the inferred slope in Fig. 4.11b for mooring T6.

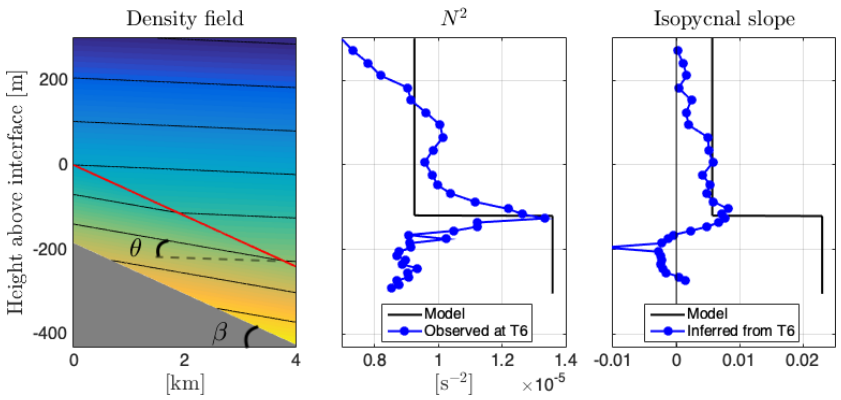

Figure 4.12: Simple model tuned to observations at mooring T6 to explain the observed peak in N^2 around the corrugation rim depth. (a) Density field in the model. (b) Profile of N^2 calculated in the model at $x = 2$ km and averaged stratification profile observed at mooring T6. (c) Profile of isopycnal slope at $x = 2$ km in the model and inferred from observations at the T6 mooring. The slope inferred from the mooring data is given by σ_x/σ_z, where the vertical gradient is calculated from thermistor data and the horizontal gradient is given by the thermal wind relation, i.e. $\sigma_x = -\frac{\rho_0}{fg} v_z$. The vertical coordinate of the blue dots in (b) and (c) correspond to the intermediate location of adjacent thermistors (relative to the z coordinate in the model). The modeled slope in the bottom layer is about 0.022, which is at most 40% of the bottom slope along the axis of the corrugation trough.

4.7 Acknowledgements

Chapter 4, in part is currently being prepared for submission for publication of the material. Marques, Olavo B.; Alford, Matthew H.; Pinkel, Robert; MacKinnon, Jennifer A.; Voet, Gunnar; Klymak, Jody M.; Nash, Jonathan D. The dissertation author was the primary investigator and author of this paper.

Bibliography

[Alford, 2003] Alford, M. H. (2003). Redistribution of energy available for ocean mixing by long-range propagation of internal waves. *Nature*, 423(6936):159.

[Alford et al., 2014] Alford, M. H., Klymak, J. M., and Carter, G. S. (2014). Breaking internal lee waves at kaena ridge, hawaii. *Geophysical Research Letters*, 41(3):906–912.

[Alford and MacCready, 2014] Alford, M. H. and MacCready, P. (2014). Flow and mixing in juan de fuca canyon, washington. *Geophysical Research Letters*, 41(5):1608–1615.

[Alford et al., 2019] Alford, M. H., Simmons, H. L., Marques, O. B., and Girton, J. B. (2019). Internal tide attenuation in the north pacific. *Geophysical Research Letters*, 0(ja).

[Alford and Zhao, 2007a] Alford, M. H. and Zhao, Z. (2007a). Global patterns of low-mode internal-wave propagation. part i: Energy and energy flux. *Journal of Physical Oceanography*, 37(7):1829–1848.

[Alford and Zhao, 2007b] Alford, M. H. and Zhao, Z. (2007b). Global patterns of low-mode internal-wave propagation. part ii: Group velocity. *Journal of physical oceanography*, 37(7):1849–1858.

[Allen and Hickey, 2010] Allen, S. E. and Hickey, B. M. (2010). Dynamics of advection-driven upwelling over a shelf break submarine canyon. *Journal of Geophysical Research: Oceans*, 115(C8).

[Aucan et al., 2006] Aucan, J., Merrifield, M. A., Luther, D. S., and Flament, P. (2006). Tidal mixing events on the deep flanks of kaena ridge, hawaii. *Journal of Physical Oceanography*, 36(6):1202–1219.

[Boettger et al., 2015] Boettger, D., Robertson, R., and Rainville, L. (2015). Characterizing the semidiurnal internal tide off tasmania using glider data. *Journal of Geophysical Research: Oceans*, 120(5):3730–3746.

[Boyer et al., 2013] Boyer, T. P., Antonov, J. I., Baranova, O. K., Coleman, C., Garcia, H. E., Grodsky, A., Johnson, D. R., Locarnini, R. A., Mishonov, A. V., O'Brien, T. D., Paver, C. R., Reagan, J. R., Seidov, D., Smolyar, I. V., and Zweng, M. M. (2013). *World Ocean Database 2013*. pages NOAA Atlas NESDIS 72, 209 pp.

[Brink, 2021] Brink, K. (2021). Near-resonances of superinertial and tidal fluctuations at islands. *Journal of Physical Oceanography*.

[Cessi, 2019] Cessi, P. (2019). The global overturning circulation. *Annual review of marine science*, 11:249–270.

[Cimatoribus et al., 2014] Cimatoribus, A. A., Van Haren, H., and Gostiaux, L. (2014). Comparison of ellison and thorpe scales from eulerian ocean temperature observations. *Journal of Geophysical Research: Oceans*, 119(10):7047–7065.

[Clément et al., 2017] Clément, L., Thurnherr, A. M., and St. Laurent, L. C. (2017). Turbulent mixing in a deep fracture zone on the mid-atlantic ridge. *Journal of Physical Oceanography*, 47(8):1873–1896.

[Cusack et al., 2017] Cusack, J. M., Naveira Garabato, A. C., Smeed, D. A., and Girton, J. B. (2017). Observation of a large lee wave in the drake passage. *Journal of Physical Oceanography*, 47(4):793–810.

[Dale and Inall, 2015] Dale, A. C. and Inall, M. E. (2015). Tidal mixing processes amid small-scale, deep-ocean topography. *Geophysical Research Letters*, 42(2):484–491.

[de Lavergne et al., 2019] de Lavergne, C., Falahat, S., Madec, G., Roquet, F., Nycander, J., and Vic, C. (2019). Toward global maps of internal tide energy sinks. *Ocean Modelling*, 137:52–75.

[De Lavergne et al., 2016] De Lavergne, C., Madec, G., Le Sommer, J., Nurser, A. G., and Naveira Garabato, A. C. (2016). On the consumption of antarctic bottom water in the abyssal ocean. *Journal of Physical Oceanography*, 46(2):635–661.

[de Lavergne et al., 2020] de Lavergne, C., Vic, C., Madec, G., Roquet, F., Waterhouse, A. F., Whalen, C., Cuypers, Y., Bouruet-Aubertot, P., Ferron, B., and Hibiya, T. (2020). A parameterization of local and remote tidal mixing. *Journal of Advances in Modeling Earth Systems*, 12(5):e2020MS002065.

[Deacon, 1937] Deacon, G. E. R. (1937). Note on the dynamics of southern ocean. *Discovery Report*, 15:125–152.

[Dillon, 1982] Dillon, T. M. (1982). Vertical overturns: A comparison of thorpe and ozmidov length scales. *Journal of Geophysical Research: Oceans*, 87(C12):9601–9613.

[Duda et al., 2018] Duda, T. F., Lin, Y.-T., Buijsman, M., and Newhall, A. E. (2018). Internal tidal modal ray refraction and energy ducting in baroclinic gulf stream currents. *Journal of Physical Oceanography*, 48(9):1969–1993.

[Egbert and Ray, 2000] Egbert, G. and Ray, R. (2000). Significant dissipation of tidal energy in the deep ocean inferred from satellite altimeter data. *Nature*, 405(6788):775.

[Egbert and Erofeeva, 2002] Egbert, G. D. and Erofeeva, S. Y. (2002). Efficient inverse modeling of barotropic ocean tides. *Journal of Atmospheric and Oceanic Technology*, 19(2):183–204.

[Ferrari et al., 2016] Ferrari, R., Mashayek, A., McDougall, T. J., Nikurashin, M., and Campin, J.-M. (2016). Turning ocean mixing upside down. *Journal of Physical Oceanography*, 46(7):2239–2261.

[Ganachaud and Wunsch, 2000] Ganachaud, A. and Wunsch, C. (2000). Improved estimates of global ocean circulation, heat transport and mixing from hydrographic data. *Nature*, 408(6811):453–457.

[Gargett and Garner, 2008] Gargett, A. and Garner, T. (2008). Determining thorpe scales from ship-lowered ctd density profiles. *Journal of Atmospheric and Oceanic Technology*, 25(9):1657–1670.

[Gellert, 1938] Gellert, J. (1938). Defant, a., böhnecke, g. und wattenberg, h. die ozeanographischen arbeiten des vermessungsschiffes" meteor" in der dänemarkstrasse und irmingersee während der fischereischutzfahrten 1929, 1930, 1933 und 1935. i. teil: Plan und reiseberichte, die tiefenkarte, das beobachtungsmaterial.(veröffentl. d. inst. f. meereskunde ad univ. berlin, nf a, heft 32.)(book review). *Geographische Zeitschrift*, 44(11):436.

[Gent and McWilliams, 1996] Gent, P. R. and McWilliams, J. C. (1996). Eliassen–palm fluxes and the momentum equation in non-eddy-resolving ocean circulation models. *Journal of Physical Oceanography*, 26(11):2539–2546.

[Gill, 1982] Gill, A. E. (1982). *Atmosphere-Ocean Dynamics*. Academic Press.

[Gregg et al., 2018] Gregg, M., D'Asaro, E., Riley, J., and Kunze, E. (2018). Mixing efficiency in the ocean. *Annual review of marine science*, 10:443–473.

[Gregg, 1991] Gregg, M. C. (1991). The study of mixing in the ocean: A brief history. *Oceanography*, 4(1):39–45.

[Hieronymus et al., 2019] Hieronymus, M., Nycander, J., Nilsson, J., Döös, K., and Hallberg, R. (2019). Oceanic overturning and heat transport: The role of background diffusivity. *Journal of Climate*, 32(3):701–716.

[Holmes et al., 2019] Holmes, R. M., Zika, J. D., Ferrari, R., Thompson, A. F., Newsom, E. R., and England, M. H. (2019). Atlantic ocean heat transport enabled by indo-pacific heat uptake and mixing. *Geophysical Research Letters*, 46(23):13939–13949.

[Jalali et al., 2017] Jalali, M., Chalamalla, V. K., and Sarkar, S. (2017). On the accuracy of overturn-based estimates of turbulent dissipation at rough topography. *Journal of Physical Oceanography*, 47(3):513–532.

[Johnston et al., 2015] Johnston, T. M. S., Rudnick, D. L., and Kelly, S. M. (2015). Standing internal tides in the tasman sea observed by gliders. *Journal of Physical Oceanography*, 45(11):2715–2737.

[Kelly and Nash, 2010] Kelly, S. and Nash, J. (2010). Internal-tide generation and destruction by shoaling internal tides. *Geophysical Research Letters*, 37(23).

[Kelly et al., 2013] Kelly, S. M., Jones, N. L., and Nash, J. D. (2013). A coupled laplace model for laplace's tidal equations in a fluid with one horizontal dimension and variable depth. *Journal of Physical Oceanography*, 43(8):1780–1797.

[Kelly et al., 2012] Kelly, S. M., Nash, J. D., Martini, K. I., Alford, M. H., and Kunze, E. (2012). The cascade of tidal energy from low to high modes on a continental slope. *Journal of physical oceanography*, 42(7):1217–1232.

[Klymak et al., 2011] Klymak, J. M., Alford, M. H., Pinkel, R., Lien, R.-C., Yang, Y. J., and Tang, T.-Y. (2011). The breaking and scattering of the internal tide on a continental slope. *Journal of Physical Oceanography*, 41(5):926–945.

[Klymak et al., 2013] Klymak, J. M., Buijsman, M., Legg, S., and Pinkel, R. (2013). Parameterizing surface and internal tide scattering and breaking on supercritical topography: The one-and two-ridge cases. *Journal of Physical Oceanography*, 43(7):1380–1397.

[Klymak et al., 2010a] Klymak, J. M., Legg, S., and Pinkel, R. (2010a). A simple parameterization of turbulent tidal mixing near supercritical topography. *Journal of Physical Oceanography*, 40(9):2059–2074.

[Klymak et al., 2010b] Klymak, J. M., Legg, S. M., and Pinkel, R. (2010b). High-mode stationary waves in stratified flow over large obstacles. *Journal of Fluid Mechanics*, 644:321.

[Klymak et al., 2006] Klymak, J. M., Moum, J. N., Nash, J. D., Kunze, E., Girton, J. B., Carter, G. S., Lee, C. M., Sanford, T. B., and Gregg, M. C. (2006). An estimate of tidal energy lost to turbulence at the hawaiian ridge. *Journal of Physical Oceanography*, 36(6):1148–1164.

[Klymak et al., 2008] Klymak, J. M., Pinkel, R., and Rainville, L. (2008). Direct breaking of the internal tide near topography: Kaena ridge, hawaii. *Journal of Physical Oceanography*, 38(2):380–399.

[Klymak et al., 2016] Klymak, J. M., Simmons, H. L., Braznikov, D., Kelly, S., MacKinnon, J. A., Alford, M. H., Pinkel, R., and Nash, J. D. (2016). Reflection of linear internal tides from realistic topography: The tasman continental slope. *Journal of Physical Oceanography*, 46(11):3321–3337.

[Kunze, 2017] Kunze, E. (2017). Internal-wave-driven mixing: Global geography and budgets. *Journal of Physical Oceanography*, 47(6):1325–1345.

[Kunze et al., 2012] Kunze, E., MacKay, C., McPhee-Shaw, E. E., Morrice, K., Girton, J. B., and Terker, S. R. (2012). Turbulent mixing and exchange with interior waters on sloping boundaries. *Journal of physical oceanography*, 42(6):910–927.

[Kunze et al., 2002] Kunze, E., Rosenfeld, L. K., Carter, G. S., and Gregg, M. C. (2002). Internal waves in monterey submarine canyon. *Journal of Physical Oceanography*, 32(6):1890–1913.

[Leaman and Sanford, 1975] Leaman, K. D. and Sanford, T. B. (1975). Vertical energy propagation of inertial waves: A vector spectral analysis of velocity profiles. *Journal of Geophysical Research*, 80(15):1975–1978.

[LeBlond and Mysak, 1981] LeBlond, P. H. and Mysak, L. A. (1981). *Waves in the Ocean*, volume 20. Elsevier.

[Ledwell et al., 1993] Ledwell, J. R., Watson, A. J., and Law, C. S. (1993). Evidence for slow mixing across the pycnocline from an open-ocean tracer-release experiment. *Nature*, 364(6439):701–703.

[Legg, 2004] Legg, S. (2004). Internal tides generated on a corrugated continental slope. part i: Cross-slope barotropic forcing. *Journal of Physical Oceanography*, 34(1):156–173.

[Legg, 2021] Legg, S. (2021). Mixing by oceanic lee waves. *Annual Review of Fluid Mechanics*, 53:173–201.

[Legg and Klymak, 2008] Legg, S. and Klymak, J. (2008). Internal hydraulic jumps and overturning generated by tidal flow over a tall steep ridge. *Journal of Physical Oceanography*, 38(9):1949–1964.

[Levine and Boyd, 2006] Levine, M. D. and Boyd, T. J. (2006). Tidally forced internal waves and overturns observed on a slope: Results from home. *Journal of physical oceanography*, 36(6):1184–1201.

[Liang et al., 2017] Liang, X., Spall, M., and Wunsch, C. (2017). Global ocean vertical velocity from a dynamically consistent ocean state estimate. *Journal of Geophysical Research: Oceans*, 122(10):8208–8224.

[Lumpkin and Speer, 2007] Lumpkin, R. and Speer, K. (2007). Global ocean meridional overturning. *Journal of Physical Oceanography*, 37(10):2550–2562.

[MacKinnon et al., 2017] MacKinnon, J. A., Zhao, Z., Whalen, C. B., Waterhouse, A. F., Trossman, D. S., Sun, O. M., St. Laurent, L. C., Simmons, H. L., Polzin, K., Pinkel, R., Pickering, A., Norton, N. J., Nash, J. D., Musgrave, R., Merchant, L. M., Melet, A. V., Mater, B., Legg, S., Large, W. G., Kunze, E., Klymak, J. M., Jochum, M., Jayne, S. R., Hallberg, R. W., Griffies, S. M., Diggs, S., Danabasoglu, G., Chassignet, E. P., Buijsman, M. C., Bryan, F. O., Briegleb, B. P., Barna, A., Arbic, B. K., Ansong, J. K., and Alford, M. H. (2017). Climate process team on internal wave–driven ocean mixing. *Bulletin of the American Meteorological Society*, 98(11):2429–2454.

[Marques et al., 2021] Marques, O. B., Alford, M. H., Pinkel, R., MacKinnon, J. A., Klymak, J. M., Nash, J. D., Waterhouse, A. F., Kelly, S. M., Simmons, H. L., and Braznikov, D.

(2021). Internal tide structure and temporal variability on the reflective continental slope of southeastern tasmania. *Journal of Physical Oceanography*, 51(2):611–631.

[Marshall et al., 1997] Marshall, J., Adcroft, A., Hill, C., Perelman, L., and Heisey, C. (1997). A finite-volume, incompressible navier stokes model for studies of the ocean on parallel computers. *Journal of Geophysical Research: Oceans*, 102(C3):5753–5766.

[Martini et al., 2007] Martini, K., Alford, M., Nash, J., Kunze, E., and Merrifield, M. (2007). Diagnosing a partly standing internal wave in mamala bay, oahu. *Geophysical Research Letters*, 34(17).

[Martini et al., 2011] Martini, K. I., Alford, M. H., Kunze, E., Kelly, S. M., and Nash, J. D. (2011). Observations of internal tides on the oregon continental slope. *Journal of Physical Oceanography*, 41(9):1772–1794.

[Mater et al., 2015] Mater, B. D., Venayagamoorthy, S. K., St. Laurent, L., and Moum, J. N. (2015). Biases in thorpe-scale estimates of turbulence dissipation. part i: Assessments from large-scale overturns in oceanographic data. *Journal of Physical Oceanography*, 45(10):2497–2521.

[McDougall and Barker, 2011] McDougall, T. J. and Barker, P. M. (2011). Getting started with teos-10 and the gibbs seawater (gsw) oceanographic toolbox. *SCOR/IAPSO WG*, 127:1–28.

[McDougall and Ferrari, 2017] McDougall, T. J. and Ferrari, R. (2017). Abyssal upwelling and downwelling driven by near-boundary mixing. *Journal of Physical Oceanography*, 47(2):261–283.

[Melet et al., 2013] Melet, A., Hallberg, R., Legg, S., and Polzin, K. (2013). Sensitivity of the ocean state to the vertical distribution of internal-tide-driven mixing. *Journal of Physical Oceanography*, 43(3):602–615.

[Melet et al., 2016] Melet, A., Legg, S., and Hallberg, R. (2016). Climatic impacts of parameterized local and remote tidal mixing. *Journal of Climate*, 29(10):3473–3500.

[Morozov, 1995] Morozov, E. G. (1995). Semidiurnal internal wave global field. *Deep Sea Research Part I: Oceanographic Research Papers*, 42(1):135–148.

[Munk and Wunsch, 1998] Munk, W. and Wunsch, C. (1998). Abyssal recipes ii: Energetics of tidal and wind mixing. *Deep Sea Research Part I: Oceanographic Research Papers*, 45(12):1977–2010.

[Munk, 1966] Munk, W. H. (1966). Abyssal recipes. In *Deep Sea Research and Oceanographic Abstracts*, volume 13, pages 707–730. Elsevier.

[Murphy, 1988] Murphy, A. H. (1988). Skill scores based on the mean square error and their relationships to the correlation coefficient. *Monthly weather review*, 116(12):2417–2424.

[Musgrave et al., 2016] Musgrave, R., MacKinnon, J., Pinkel, R., Waterhouse, A., and Nash, J. (2016). Tidally driven processes leading to near-field turbulence in a channel at the crest of the mendocino escarpment. *Journal of Physical Oceanography*, 46(4):1137–1155.

[Musgrave, 2019] Musgrave, R. C. (2019). Energy fluxes in coastal trapped waves. *Journal of Physical Oceanography*, 49(12):3061–3068.

[Nash et al., 2007] Nash, J., Alford, M., Kunze, E., Martini, K., and Kelly, S. (2007). Hotspots of deep ocean mixing on the oregon continental slope. *Geophysical Research Letters*, 34(1).

[Nash et al., 2005] Nash, J. D., Alford, M. H., and Kunze, E. (2005). Estimating internal wave energy fluxes in the ocean. *Journal of Atmospheric and Oceanic Technology*, 22(10):1551–1570.

[Nash et al., 2004] Nash, J. D., Kunze, E., Toole, J. M., and Schmitt, R. W. (2004). Internal tide reflection and turbulent mixing on the continental slope. *Journal of Physical Oceanography*, 34(5):1117–1134.

[Nash et al., 2012] Nash, J. D., Shroyer, E. L., Kelly, S. M., Inall, M. E., Duda, T. F., Levine, M. D., Jones, N. L., and Musgrave, R. C. (2012). Are any coastal internal tides predictable? *Oceanography*, 25(2):80–95.

[Niwa and Hibiya, 2001] Niwa, Y. and Hibiya, T. (2001). Numerical study of the spatial distribution of the m2 internal tide in the pacific ocean. *Journal of Geophysical Research: Oceans*, 106(C10):22441–22449.

[Oke et al., 2019] Oke, P. R., Roughan, M., Cetina-Heredia, P., Pilo, G. S., Ridgway, K. R., Rykova, T., Archer, M. R., Coleman, R. C., Kerry, C. G., Rocha, C., Schaeffer, A., and Vitarelli, E. (2019). Revisiting the circulation of the east australian current: Its path, separation, and eddy field. *Progress in Oceanography*, 176:102139.

[Osborn, 1980] Osborn, T. (1980). Estimates of the local rate of vertical diffusion from dissipation measurements. *Journal of Physical Oceanography*, 10(1):83–89.

[Phillips, 1966] Phillips, O. M. (1966). *The dynamics of the upper ocean*, volume 1. Cambridge University Press.

[Pickering et al., 2015] Pickering, A., Alford, M., Nash, J., Rainville, L., Buijsman, M., Ko, D. S., and Lim, B. (2015). Structure and variability of internal tides in luzon strait. *Journal of Physical Oceanography*, 45(6):1574–1594.

[Pinkel et al., 2015] Pinkel, R., Alford, M., Lucas, A., Johnston, S., MacKinnon, J., Waterhouse, A., and Strutton, P. (2015). Breaking internal tides keep the ocean in balance. *Eos*, 96:1–5.

[Pinkel et al., 2012] Pinkel, R., Buijsman, M., and Klymak, J. M. (2012). Breaking topographic lee waves in a tidal channel in luzon strait. *Oceanography*, 25(2):160–165.

[Polzin et al., 1997] Polzin, K., Toole, J., Ledwell, J., and Schmitt, R. (1997). Spatial variability of turbulent mixing in the abyssal ocean. *Science*, 276(5309):93–96.

[Polzin and McDougall, 2021] Polzin, K. L. and McDougall, T. J. (2021). Mixing at the ocean's bottom boundary. In *Ocean Mixing*, pages 145–180. Elsevier.

[Ray and Mitchum, 1996] Ray, R. D. and Mitchum, G. T. (1996). Surface manifestation of internal tides generated near hawaii. *Geophysical Research Letters*, 23(16):2101–2104.

[Sarkar and Scotti, 2017] Sarkar, S. and Scotti, A. (2017). From topographic internal gravity waves to turbulence. *Annual Review of Fluid Mechanics*, 49(1):195–220.

[Savage et al., 2017] Savage, A. C., Arbic, B. K., Richman, J. G., Shriver, J. F., Alford, M. H., Buijsman, M. C., Thomas Farrar, J., Sharma, H., Voet, G., Wallcraft, A. J., and Zamudio, L. (2017). Frequency content of sea surface height variability from internal gravity waves to mesoscale eddies. *Journal of Geophysical Research: Oceans*, 122(3):2519–2538.

[Savage et al., 2020] Savage, A. C., Waterhouse, A. F., and Kelly, S. M. (2020). Internal tide nonstationarity and wave–mesoscale interactions in the tasman sea. *Journal of Physical Oceanography*, 50(10):2931–2951.

[Schlosser et al., 2019] Schlosser, T. L., Jones, N. L., Musgrave, R. C., Bluteau, C. E., Ivey, G. N., and Lucas, A. J. (2019). Observations of diurnal coastal-trapped waves with a thermocline-intensified velocity field. *Journal of Physical Oceanography*, 49(7):1973–1994.

[Scotti, 2015] Scotti, A. (2015). Biases in thorpe-scale estimates of turbulence dissipation. part ii: Energetics arguments and turbulence simulations. *Journal of Physical Oceanography*, 45(10):2522–2543.

[Shakespeare, 2020] Shakespeare, C. J. (2020). Interdependence of internal tide and lee wave generation at abyssal hills: Global calculations. *Journal of Physical Oceanography*, 50(3):655–677.

[Shakespeare and Hogg, 2019] Shakespeare, C. J. and Hogg, A. M. (2019). On the momentum flux of internal tides. *Journal of Physical Oceanography*, 49(4):993–1013.

[Simmons et al., 2004] Simmons, H. L., Hallberg, R. W., and Arbic, B. K. (2004). Internal wave generation in a global baroclinic tide model. *Deep Sea Research Part II: Topical Studies in Oceanography*, 51(25-26):3043–3068.

[Smith, 2020] Smith, J. A. (2020). A comparison of two methods using thorpe sorting to estimate mixing. *Journal of Atmospheric and Oceanic Technology*, 37(1):3–15.

[Spingys et al., 2021] Spingys, C. P., Naveira Garabato, A. C., Legg, S., Polzin, K. L., Abrahamsen, E. P., Buckingham, C. E., Forryan, A., and Frajka-Williams, E. E. (2021). Mixing and transformation in a deep western boundary current: A case study. *Journal of Physical Oceanography*, 51(4):1205–1222.

[St. Laurent et al., 2001] St. Laurent, L. C., Toole, J. M., and Schmitt, R. W. (2001). Buoyancy forcing by turbulence above rough topography in the abyssal brazil basin. *Journal of Physical Oceanography*, 31(12):3476–3495.

[Stommel, 1950] Stommel, H. (1950). The gulf stream. *The Scientific Monthly*, 70(4):242–253.

[Stommel, 1958] Stommel, H. (1958). The abyssal circulation. *Deep-Sea Res.*, 5:80–82.

[Sverdrup et al., 1942] Sverdrup, H. U., Johnson, M. W., and Fleming, R. H. (1942). *The Oceans: Their physics, chemistry, and general biology*, volume 1087. Prentice-Hall New York.

[Talley, 2013] Talley, L. D. (2013). Closure of the global overturning circulation through the indian, pacific, and southern oceans: Schematics and transports. *Oceanography*, 26(1):80–97.

[Thorpe, 2001] Thorpe, S. (2001). Internal wave reflection and scatter from sloping rough topography. *Journal of physical oceanography*, 31(2):537–553.

[Thorpe, 1977] Thorpe, S. A. (1977). Turbulence and mixing in a scottish loch. *Philosophical Transactions of the Royal Society of London. Series A, Mathematical and Physical Sciences*, 286(1334):125–181.

[Thurnherr et al., 2020] Thurnherr, A. M., Clément, L., Laurent, L. S., Ferrari, R., and Ijichi, T. (2020). Transformation and upwelling of bottom water in fracture zone valleys. *Journal of Physical Oceanography*, 50(3):715–726.

[van Haren, 2017] van Haren, H. (2017). Exploring the vertical extent of breaking internal wave turbulence above deep-sea topography. *Dynamics of atmospheres and oceans*, 77:89–99.

[Vic et al., 2019] Vic, C., Garabato, A. C. N., Green, J. M., Waterhouse, A. F., Zhao, Z., Melet, A., de Lavergne, C., Buijsman, M. C., and Stephenson, G. R. (2019). Deep-ocean mixing driven by small-scale internal tides. *Nature communications*, 10.

[Voet et al., 2020] Voet, G., Alford, M. H., MacKinnon, J. A., and Nash, J. D. (2020). Topographic form drag on tides and low-frequency flow: Observations of nonlinear lee waves over a tall submarine ridge near palau. *Journal of Physical Oceanography*, 50(5):1489–1507.

[Voet et al., 2015] Voet, G., Girton, J. B., Alford, M. H., Carter, G. S., Klymak, J. M., and Mickett, J. B. (2015). Pathways, volume transport, and mixing of abyssal water in the samoan passage. *Journal of Physical Oceanography*, 45(2):562–588.

[Waterhouse et al., 2018] Waterhouse, A. F., Kelly, S. M., Zhao, Z., MacKinnon, J. A., Nash, J. D., Simmons, H., Brahznikov, D., Rainville, L., Alford, M., and Pinkel, R. (2018). Observations of the tasman sea internal tide beam. *Journal of Physical Oceanography*, 48(6):1283–1297.

[Waterhouse et al., 2014] Waterhouse, A. F., MacKinnon, J. A., Nash, J. D., Alford, M. H., Kunze, E., Simmons, H. L., Polzin, K. L., Laurent, L. C. S., Sun, O. M., Pinkel, R., Talley, L. D., Whalen, C. B., Huussen, T. N., Carter, G. S., Fer, I., Waterman, S., Garabato, A. C. N., Sanford, T. B., and Lee, C. M. (2014). Global patterns of diapycnal mixing from measurements of the turbulent dissipation rate. *Journal of Physical Oceanography*, 44(7):1854–1872.

[Whalen et al., 2012] Whalen, C., Talley, L., and MacKinnon, J. (2012). Spatial and temporal variability of global ocean mixing inferred from argo profiles. *Geophysical Research Letters*, 39(18).

[Whalen et al., 2020] Whalen, C. B., de Lavergne, C., Garabato, A. C. N., Klymak, J. M., Mackinnon, J. A., and Sheen, K. L. (2020). Internal wave-driven mixing: governing processes and consequences for climate. *Nature Reviews Earth & Environment*, 1(11):606–621.

[Wunsch, 1968] Wunsch, C. (1968). On the propagation of internal waves up a slope. In *Deep Sea Research and Oceanographic Abstracts*, volume 15, pages 251–258. Elsevier.

[Wunsch, 1975] Wunsch, C. (1975). Internal tides in the ocean. *Reviews of Geophysics*, 13(1):167–182.

[Wunsch and Ferrari, 2004] Wunsch, C. and Ferrari, R. (2004). Vertical mixing, energy, and the general circulation of the oceans. *Annu. Rev. Fluid Mech.*, 36:281–314.

[Zaron, 2017] Zaron, E. D. (2017). Mapping the nonstationary internal tide with satellite altimetry. *Journal of Geophysical Research: Oceans*, 122(1):539–554.

[Zhao, 2016] Zhao, Z. (2016). Internal tide oceanic tomography. *Geophysical Research Letters*, 43(17):9157–9164.

[Zhao, 2018] Zhao, Z. (2018). The global mode-2 m2 internal tide. *Journal of Geophysical Research: Oceans*, 123(11):7725–7746.

[Zhao et al., 2016] Zhao, Z., Alford, M. H., Girton, J. B., Rainville, L., and Simmons, H. L. (2016). Global observations of open-ocean mode-1 m2 internal tides. *Journal of Physical Oceanography*, 46(6):1657–1684.

[Zhao et al., 2010] Zhao, Z., Alford, M. H., MacKinnon, J. A., and Pinkel, R. (2010). Long-range propagation of the semidiurnal internal tide from the hawaiian ridge. *Journal of Physical Oceanography*, 40(4):713–736.

[Zhao et al., 2018] Zhao, Z., Alford, M. H., Simmons, H. L., Brazhnikov, D., and Pinkel, R. (2018). Satellite investigation of the m_2 internal tide in the tasman sea. *Journal of Physical Oceanography*, 48(3):687–703.

[Zilberman et al., 2011] Zilberman, N., Merrifield, M., Carter, G., Luther, D., Levine, M., and Boyd, T. J. (2011). Incoherent nature of m 2 internal tides at the hawaiian ridge. *Journal of physical oceanography*, 41(11):2021–2036.